

AD\_\_\_\_\_

Award Number: W81XWH-04-1-0240

TITLE: High Resolution Anatomic and Elastographic Transrectal Ultrasound for Improved Diagnosis of Prostate Cancer

PRINCIPAL INVESTIGATOR: John A. Hossack, Ph.D.

CONTRACTING ORGANIZATION: University of Virginia  
Charlottesville, VA 22908-0759

REPORT DATE: February 2006

TYPE OF REPORT: Annual

PREPARED FOR: U.S. Army Medical Research and Materiel Command  
Fort Detrick, Maryland 21702-5012

DISTRIBUTION STATEMENT: Approved for Public Release;  
Distribution Unlimited

The views, opinions and/or findings contained in this report are those of the author(s) and should not be construed as an official Department of the Army position, policy or decision unless so designated by other documentation.

REPORT DOCUMENTATION PAGE				Form Approved OMB No. 0704-0188	
Public reporting burden for this collection of information is estimated to average 1 hour per response, including the time for reviewing instructions, searching existing data sources, gathering and maintaining the data needed, and completing and reviewing this collection of information. Send comments regarding this burden estimate or any other aspect of this collection of information, including suggestions for reducing this burden to Department of Defense, Washington Headquarters Services, Directorate for Information Operations and Reports (0704-0188), 1215 Jefferson Davis Highway, Suite 1204, Arlington, VA 22202-4302. Respondents should be aware that notwithstanding any other provision of law, no person shall be subject to any penalty for failing to comply with a collection of information if it does not display a currently valid OMB control number. <b>PLEASE DO NOT RETURN YOUR FORM TO THE ABOVE ADDRESS.</b>					
1. REPORT DATE (DD-MM-YYYY) 01-02-2006		2. REPORT TYPE Annual		3. DATES COVERED (From - To) 21 JAN 2005 - 20 JAN 2006	
4. TITLE AND SUBTITLE High Resolution Anatomic and Elastographic Transrectal Ultrasound for Improved Diagnosis of Prostate Cancer				5a. CONTRACT NUMBER	
				5b. GRANT NUMBER W81XWH-04-1-0240	
				5c. PROGRAM ELEMENT NUMBER	
6. AUTHOR(S) John A. Hossack, Ph.D.  E-Mail: <a href="mailto:jh7fj@virginia.edu">jh7fj@virginia.edu</a>				5d. PROJECT NUMBER	
				5e. TASK NUMBER	
				5f. WORK UNIT NUMBER	
7. PERFORMING ORGANIZATION NAME(S) AND ADDRESS(ES)  University of Virginia Charlottesville, VA 22908-0759				8. PERFORMING ORGANIZATION REPORT NUMBER	
9. SPONSORING / MONITORING AGENCY NAME(S) AND ADDRESS(ES) U.S. Army Medical Research and Materiel Command Fort Detrick, Maryland 21702-5012				10. SPONSOR/MONITOR'S ACRONYM(S)	
				11. SPONSOR/MONITOR'S REPORT NUMBER(S)	
12. DISTRIBUTION / AVAILABILITY STATEMENT Approved for Public Release; Distribution Unlimited					
13. SUPPLEMENTARY NOTES					
14. ABSTRACT: In this work we improve upon conventional Digital Rectal Examination (DRE) and PSA blood test by using ultrasound elasticity imaging. A latex sheath over the transrectal ultrasound probe is slightly inflated with water to provide a source of moderate pressure. The elasticity image is generated by cross-correlating successive raw radio frequency image data sets for incrementally increasing pressure. Strain, and consequently elasticity, can be calculated from the displacement image. Our second objective is to use a new freehand 3D acquisition approach to obtain 3D image data sets. This approach uses a slightly modified transducer and an image motion tracking technique. Preliminary phantom based results are presented in this report. Excellent progress has been made with respect to the Statement of Work and first three of four total Specific Aims. A transducer has been specified and is on order. As promised, this transducer is designed to possess unsurpassed prostate scanning resolution by virtue of its exceptionally high frequency – up to 14 MHz. Prototype phantoms and complete ultrasound test instrumentation has been assembled. Preliminary ultrasound image speckle reduction work has been performed. Preliminary, dimensionally accurate, 3D prostate phantom images have been produced.					
15. SUBJECT TERMS Ultrasound, Imaging, Diagnostic, Elastography, 3D Imaging, Image Processing					
16. SECURITY CLASSIFICATION OF:			17. LIMITATION OF ABSTRACT	18. NUMBER OF PAGES	19a. NAME OF RESPONSIBLE PERSON
a. REPORT	b. ABSTRACT	c. THIS PAGE			USAMRMC
U	U	U	UU	108	19b. TELEPHONE NUMBER (include area code)

## Table of Contents

<b>Introduction.....</b>	<b>4</b>
<b>Body.....</b>	<b>5</b>
<b>Key Research Accomplishments.....</b>	<b>19</b>
<b>Reportable Outcomes.....</b>	<b>19</b>
<b>Conclusions.....</b>	<b>19</b>
<b>References.....</b>	<b>21</b>
<b>Appendices.....</b>	<b>22</b>

## INTRODUCTION

The American Cancer Society estimated that there would be approximately 230,110 new cases diagnosed and approximately 29,900 prostate cancer related deaths in 2004 [1]. Prostate cancer screening today generally uses the Prostate Specific Antigen (PSA) blood testing, free PSA testing and Digital Rectal Examination (DRE). When using a 'cutoff' of PSA > 4.0 ng/mL and an abnormal DRE, sensitivity, specificity and Positive Predictive Value (PPV) are 38%, 88% and 56% respectively [2]. When either an elevated PSA or an abnormal DRE are used, (in isolation – not in combination), sensitivity, specificity and PPV are even lower [2]. When the PSA is used there exists a significant gray area (4 - 10 ng/mL) in which cancers may be missed and yet the number of negative biopsies is large. Even though cancer detection sensitivity, specificity and PPV are improved by combining PSA and DRE [2, 3] the usefulness of DRE remains fundamentally limited due to its subjective nature. Additionally, DRE is practically limited to the detection of shallow (subcapsular) palpable abnormalities. Even systematic multi-core biopsy fails to detect clinically detectable cancers in up to 34% of men [4]. However, there is evidence that as additional biopsies cores are added, sensitivity improves [5]. This observation has resulted in an increase the number of cores taken during routine examination. Nevertheless, biopsy-based detection sensitivity remains less than ideal. Thus, there is plenty of compelling clinical interest in finding improved methods for the early diagnosis of prostate cancer with improved sensitivity and specificity. One recent example of progress in the field of prostate cancer detection involves an effort to automate the DRE examination. Savazyan recently described a system for 'mechanical imaging' of the prostate [6]. This system comprises a rectal probe that is instrumented with an array of pressure sensing strain gages and a 3D magnetic positioner device. In an *in vitro* trial [7], the new system correctly detected and located 100% of the nodules under examination. This compares with detection rates of 83% and 67% for an experienced urologist and a student respectively. Thus, a significant improvement over the conventional DRE examination has been demonstrated for the *in vitro* case. Another recent development is the observation that the sensitivity of an ultrasound examination can be improved by the use of a microbubble based contrast agents [4]. Frauscher's approach [4] involved the use of contrast agent enhanced Color Doppler that improved the detection of hypervascular regions associated cancer. Prostate cancer was detected by contrast agent assisted ultrasound in 23 of 24 patients known to have prostate cancer. (The method used for determining definitively which patients had cancer is not entirely clear in the article.) In comparison, conventional ultrasound detected cancer in 17 patients. The contrast agent assisted approach detected cancer in 8 patients with a negative systematic biopsy-based diagnosis. However, the cost of the contrast agent used in this study was \$65 per patient. This cost makes up approximately half of the cost of a conventional ultrasound examination and therefore represents a considerable impediment to its widespread acceptance. However, more recent publications [8, 9] (including one from Frauscher's group) cast doubt on the true extent of the improvement in diagnostic accuracy obtained by using contrast agents. Specifically, Halpern was unable to detect cancers in the inner gland and achieved a cancer detection sensitivity of only 42% [8].

## BODY

The work conducted as part of this Army funded program can be considered as divided into the following key "Aims":

1. Research, design, development and prototype testing of a new transrectal ultrasound transducer, syringe pump and ultrasound instrumentation to facilitate a Synthetic Digital Rectal Examination (SDRE).
2. Research, development and prototype testing of techniques to enable quantitative (dimensionally accurate) 3D reconstructions of the prostate
3. Research, development and test of techniques to improve ultrasound image quality and to facilitate automated (or semi-automated) border detection of lesions
4. Small scale clinical test at the University of Virginia

Progress has been made in each of these tasks in the second year of the grant. The work is on-track. (The fourth section of work, the small scale clinical test, will occur in the third year of the grant.)

Progress with respect to the areas are related directly to the committed Statement of Work that was funded:

### **Aim 1. Design, specify, and have built, a high resolution transducer optimized for imaging elastic inhomogeneities, unsurpassed B-Mode image resolution and possessing integrated 3D capability.**

A high frequency (8-14 MHz) transducer array was designed and specified as committed in Year 1. Vernon SA, Tours, France made the transducer and it was delivered in Q1 2005. The transducer has two tracking arrays each with 32 elements and a central imaging array with 192 elements. The elements are spaced on a 0.2 mm pitch. This transducer is providing unsurpassed imaging resolution in a transducer housing designed for transrectal ultrasound. The transducer will provide the very best image data as a solid foundation for the subsequent work elements. This transducer is operable at up to 14MHz whereas the previously available transducer was only operable up to 8 MHz. Consequently, we are observing excellent, and significant, improvements in image resolution.

### **Aim 2. Develop and test a tissue elasticity imaging system.**

As committed, we have assembled the apparatus to enable the new approach to transrectal ultrasound based strain imaging. (Most of this work was completed in Year 1.) We have also fabricated several custom prostate phantoms using locally developed techniques [10]. By making the phantoms internally, we are able to iterate efficiently the design and also to fabricate replacement phantoms at very low cost in a timely manner. Phantoms tend to deteriorate over time due to dehydration through the membranes. We have tested the tissue elasticity system using both an older 8 MHz transrectal transducer and the newer 14 MHz transducer connected to our Siemens Sequoia ultrasound machine. Our techniques can be migrated to other ultrasound systems if resource and contractual issues are addressed.

The deliverable for this phase is complete as of the end of Year 2 work and a validated (phantom) elasticity imaging system using the approach presented in the proposal has been produced. We have verified our ability to obtain very fine resolution 3D reconstructions and fine resolution elasticity images using the newly completed tissue elasticity system.

### **Aim 3. Apply image processing algorithms to acquired B-Mode and elasticity images to improve the quantification of detected elastic inhomogeneities**

We have developed 3D surface rendering from 2D slices by implementing a 3D gradient vector flow (GVF) snake algorithm [11]. The algorithm relies on the edges to be well delineated and contrast between the various regions to be well defined in each 2D ultrasound slice to produce a surface that resembles the actual scanned object. A preprocessing despeckling step is needed to reduce the variances in pixel values within homogeneous regions. We have evaluated a wide variety of well known methods and a novel stochastically driven method design specifically for 3D surface rendering from 2D slices of the prostate and other organs. The method we develop specifically for the task of this grant is a stochastically driven compression filter called the squeeze box filter (SBF). Our quantitative evaluation using a Field II [12] simulated B mode ultrasound image with contrast enhancement performance determined by a modified Fisher discriminant has determined that the newly developed SBF method outperformed the other methods and is exceptional in providing the needed intraregion reduction in variance and inter-region contrast enhancement with computational efficiency.

Excellent progress with respect to Aim 3 has been made in the second year of the grant.

The fourth Aim from the Statement of Work relates to a small scale clinical validation in collaboration with partially funded University of Virginia collaborator – Dr. Dan Theodorescu. This item of work will be addressed in the final year of the grant.

## Summary Statement of work completed to date:

(Comprises part of work included as Appendix plus recent image processing results.)

### Prostate Phantom

A purpose-built prostate phantom was designed using the method described in Negron et al. [10]. A simulated lesion (approximately 0.3 ml) was formed inside of an egg-shaped tissue region mimicking a prostate. A cylindrical cavity (20 mm in diameter) was formed to mimic the anal opening and to allow access for the transrectal transducer. A hypoechoic gel component surrounds these three components. (Strictly speaking, the surrounding gel should be echogenic too but the lack of echoic inclusions is immaterial in our phantom studies.) The lesion is made of 17% (by weight) acrylamide gel; the tissue and exterior component are made of 5% acrylamide gel. Thus, the lesion is perceptibly stiffer (approximately 10 times stiffer) than both the egg shaped tissue region and the exterior gel component. A similar concentration (by volume) of Sephadex was added to both the lesion and the tissue, resulting in similar ultrasound image intensity in these two structures (The lesion was made slightly brighter than the tissue in order to assist navigation during scanning.) A B-mode ultrasound image of the prostate is shown in Fig. 1. The lesion in the image is almost isoechoic. This phantom is similar to ones we have made since the beginning of the project.

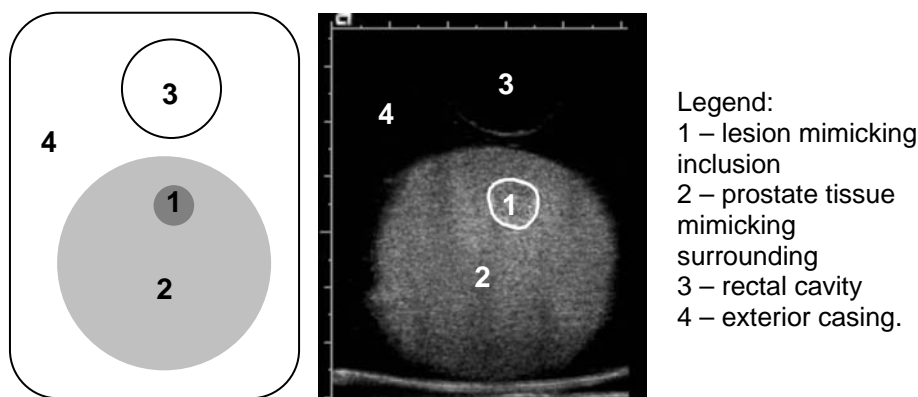


Fig. 1. Left: Schematic of the transrectal design of prostate phantom. Right: An ultrasound image of the phantom.

### Transducer

Vernon SA, Tours, France fabricated an 8-14MHz transrectal transducer to our specification. This was delivered in Q1 2005. Most prostate transducers used today in premium ultrasound scanners use a tightly curved array placed on the end of the transrectal probe. Thus, these probes have limited aperture contribution to image resolution at any particular point in the image field. However, this new transducer has a linear array format and hence has a longer available aperture that results in finer lateral resolution. Thus, we believe that this transducer's imaging resolution is practically unmatched in the field of prostate ultrasound. Image resolution is approximately 0.2 mm lateral and 0.1 mm in the axial (range) dimension. The array pitch is 0.2 mm. There are 192 elements in the imaging array and 32 elements in each of the two perpendicular tracking arrays that provide the transducer with "I-Beam" 3D tracking [13]. This form of 3D tracking yields approximately 4.6% accuracy at the two standard deviation level. (95% of measurements will be within 4.6%.) The I-Beam transducer is also uniquely matched to the transrectal prostate ultrasound application for the following reasons: a) the transrectal probe with the tracking mechanism near the transducer minimizes numerical ill-conditioning that may arise if the means of tracking is separated from the imaging array, and b) the I-Beam transducer estimates the relative tissue motion rather than

absolute tissue motion, which enables efficient and accurate measurements even if there is patient motion of the type that can defeat a 3D system that uses a fixed origin for 3D positioning (eg. Magnetic-based, optical-based, or articulated arm-based positioner.)

The newly developed transducer required new software drivers to be developed to enable it to “run” on our Siemens Sequoia research scanner. One graduate research assistant (Yinbo Li) spent the summer of 2005 at Siemens Engineering in Mountain View, CA, developing the required software with assistance from Siemens Engineering Staff – primarily Greg Holley. Siemens assisted with costs associated with this development. Siemens Engineering also performed ultrasound output intensity measurements to verify that the transducer satisfies current FDA regulated intensities (primarily that Mechanical Index (MI)  $\leq 1.9$ ). While the transducer was having software development, we also took advantage of the opportunity to add a contrast agent imaging mode for potential future work in this area. Contrast Pulse Sequences [14] was implemented on the transducer. It is intended that this will enable future work that might be based on measuring perfusion in prostate or locating the presence of molecular targeted ultrasound contrast. These applications are beyond the scope of the currently funded work and will not be pursued without future funding and any requisite permission.

The transducer, system and phantom are assembled into a complete working 3D scanning / elastographic system by adding a latex sheath over the transducer (secured with elastic bands), Tygon™ flexible plastic tubing and syringe pump to controllable inflate the sheath with plain tap water. When these components are assembled we have the basic apparatus for the “Synthetic Digital Rectal Examination” described in the proposal. The programmable syringe pump is a Harvard Instruments PHD 2000, (Harvard Apparatus, Holliston MA). This pump enables automatic water inflation and can generate a quasistatic stress and produce as uniform tissue deformation as possible. A syringe volume of 60 ml was chosen to provide sufficient water to compress and deform the rectal wall thus providing an optimal tissue strain. This volume is also appropriate in that when used in a clinical setting, the ultimate size of the syringe makes the water injection process safe in that the syringe is emptied before any patient injury could be anticipated. We have recently discovered that other research groups have also adopted a somewhat similar balloon inflation method but that these earlier efforts use a manually operated syringe [15, 16].

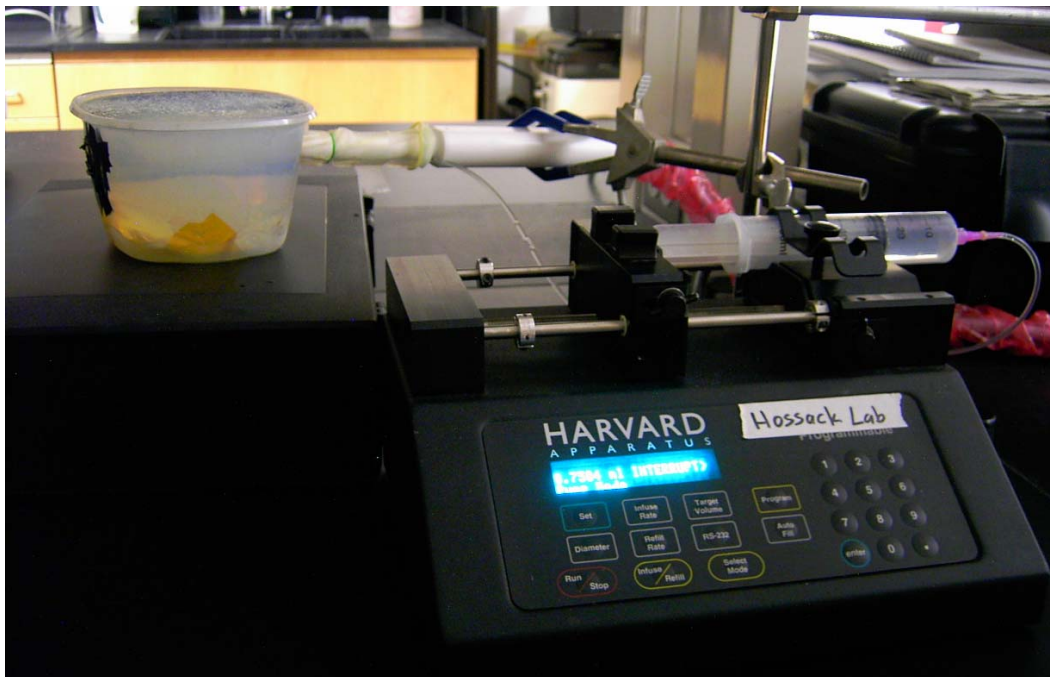


Fig. 2. The transrectal transducer is covered with a latex condom. Water was inflated by the syringe during imaging



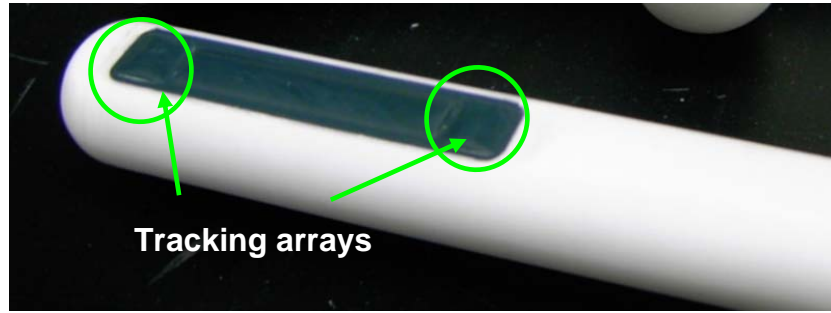


Fig. 3. I-Beam transducer – possessing a main imaging array in the center and a tracking array in each end

Five elevational slices each comprising of 100 Sequoia 14 MHz In-phase/Quadrature (I/Q) data frames were acquired during the in-vitro experiment using an incremental strain between the consecutive frames of 0.04 %. Total applied strain between the first and the last frame was approximately 4 %. This strain is broadly in accordance with the degree of strain that has been found to be optimal for strain imaging [17]. An example B-mode image obtained by the transrectal I-Beam transducer is shown in Fig. 4.

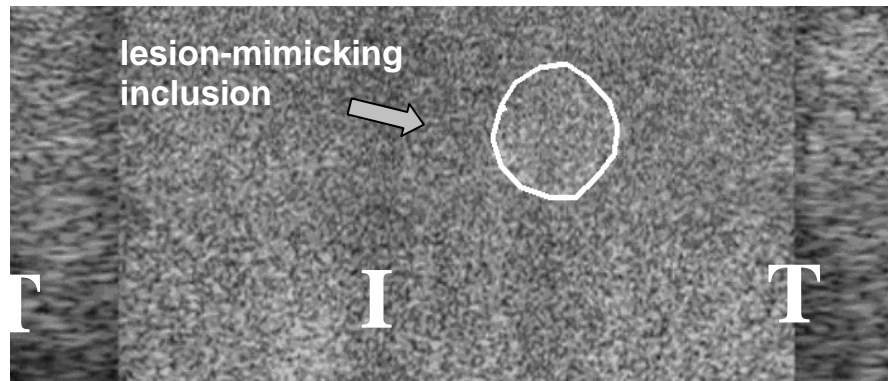


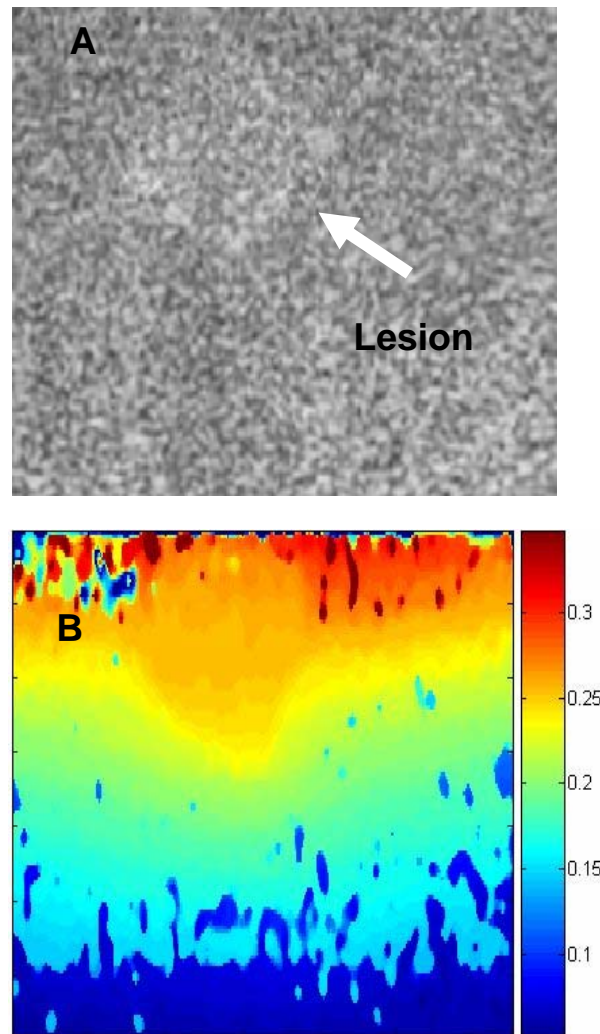
Fig. 4. A B-mode image acquired with the I-Beam transrectal transducer from the prostate-mimicking phantom, showing the layout of image planes formed by 'Tracking' arrays and 'Imaging' array. 'T' – tracking array, 'I' – main imaging array. Delineated is a lesion-mimicking inclusion.

## Elasticity Calculation and 3D Reconstruction

The acquired IQ data were filtered using a low-pass filter to reduce jitter, electronic noise, and out-of band noise. Six pairs of frames with differential strain of 2% were tracked using a time-domain cross-correlation technique. Signal “companding” or stretching was employed to maximize the cross-correlation coefficient between the pre- and the post-compression frames. Companding techniques improve contrast to noise ratio of the strain images. This improvement is desirable as the prostate lesions are known to be twice or at most thrice stiffer than the prostate. Sub-sample precision was obtained in the delay estimates by using a quadratic fit to the cross-correlation function. A search window of approximately 5 wavelengths was used for time-delay estimation. Lateral motion was tracked using the technique described by Lubinski et al.[18]. Displacement estimated from these six different renditions were averaged to eliminate uncorrelated random noise. Strain estimates were then obtained by taking the local gradient of the displacement image (in axial direction). The above process was repeated by sweeping the transducer in the elevational direction and six elevational slices were obtained. In the elevation direction, the inter-slice distance was estimated with a block matching approach based upon the minimum sum of absolute differences (MSAD) algorithm of the I-Beam 'Tracking' data. The inter-slice distance was found to be slightly larger in the deeper portion than in the shallower portion, indicating that the transducer was rotated

by small angles between measurements. In the measurements, the slices were sampled with an interval no greater than 2 mm, and the rotation angle increments were less than 2 degrees in order to ensure that the elevational motion could be accurately tracked. Once the elevational motion of these blocks was calculated, the acquired image slices were interpolated on to a regular 3D grid in Matlab enabling 3D volumes to be rendered

Figure 5 illustrates the lesion detection process. The elasticity reconstruction algorithm was tested on the phantom data. The elasticity reconstruction process for the detection of prostate cancer is complicated than the elasticity reconstruction process of the breast cancers. Unlike the boundary conditions for breast cancer detection, the boundary conditions for prostate cancer detection are non-trivial. The effect of which is obvious in the reconstructed displacement and the strain images. These non-uniform boundary conditions result in non-uniform and non-symmetric internal displacements, which can be seen in the axial displacement image. This results in strain concentration artifacts along the top most boundary of the strain image. The non-uniform boundary conditions also cause a non-linear decay in strain with increasing depths. The isolated saturation of strain in the lower quarter of the strain image is due to the out-of-plane motion, which cannot be tracked with linear array transducer. Two-dimensional arrays may probably solve these problems, which in turn may result in substantial improvement in the quality of strain images. It is also important to note that no post-processing was done on the strain images. In spite of the unique challenges associated with the elasticity reconstruction process of the prostate



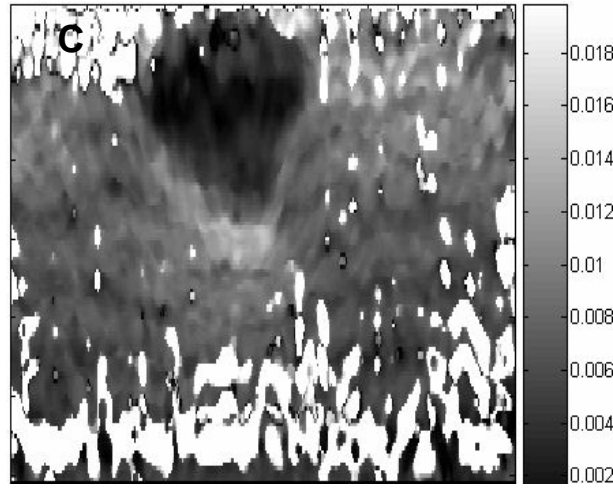
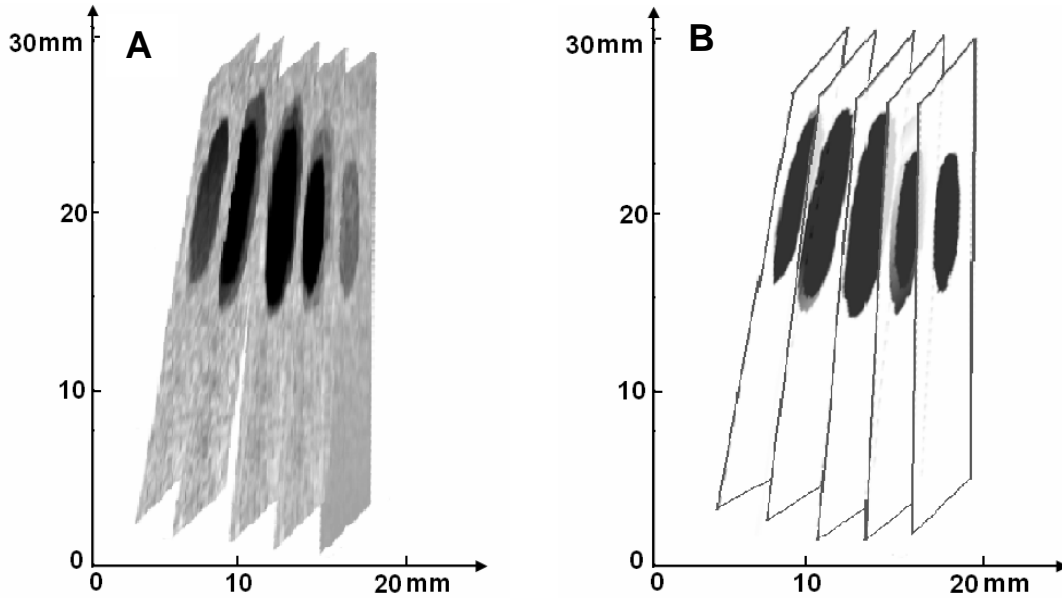


Fig. 5. The lesion detection process. The lesion is barely identifiable in the original B-mode image (A). A displacement image is illustrated in (B). The lesion is clearly identifiable in the strain image (C).

The 3D volume of the detected lesion was calculated after segmenting the 2D contour in each slice and estimating the inter-slice distance. A multiple slice view and a 3D surface view of the identified lesion were rendered based on the 3D dataset as shown in Fig. 6. The volume measured in the elastography and 3D reconstruction is approximately  $339 \pm 11 \text{ mm}^3$  less than 15 % volumetric error from the volume of  $300 \pm 30 \text{ mm}^3$  measured using Archimedes principle.



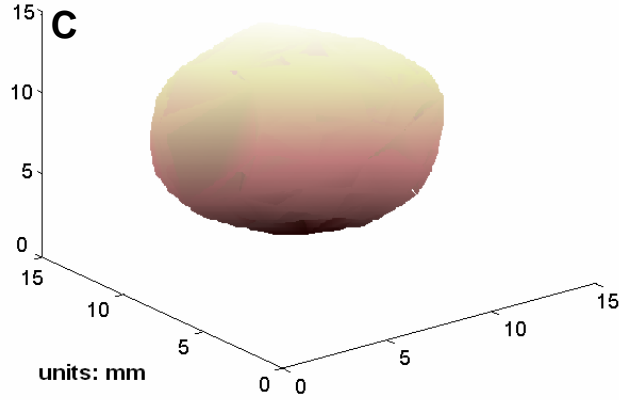


Fig. 6. 3D reconstruction of the lesion. A: The multiple 2D image slices acquired were rendered in three dimensions. The lesion was shown darker than surrounding tissue. B: The multiple slices of elasticity images with the detected lesion shown in black. C: The prostate lesion detected from the ultrasound images. The lesion was segmented from the surrounding tissue and its 3D surface was rendered.

The results shown above indicate that the finer resolution of the new higher frequency transducer yield superior imaging and 3D reconstruction results. The new transducer operates at up to 14 MHz. The transducer previously used (as reported last year) used 8 MHz imaging and a similar aperture dimension. Taken together, our in vitro results make us well place to commence initial patient studies once our Army and Institutional Review Board permission is obtained. The paperwork associated with these studies is being completed at the time of writing.

### Image Processing and Quantification

We have progressed to a accurate 3D surface rendering from 2D slices by implementing a 3D gradient vector flow (GVF) snake algorithm [11]. The 2D and 3D GVF snake algorithm relies on the edges to be well delineated and contrast between the various regions to be well defined in each 2D ultrasound slice to produce a surface that resembles the actual scanned object. In ultrasound, images are affected by a granular pattern commonly known as speckle. Before an accurate 3D surface rendering can be attained a preprocessing despeckling step is needed to reduce the variances in pixel values within homogeneous regions while contrast between distinct regions are concurrently enhanced. We have evaluated a wide variety of well known methods such as the Nagao and Matsuyama filter [19], the Lee filter[20], the Frost *et al.* filter [21], the Kuan *et al.* filter [22], the adaptive weighted median filter proposed by Loupas *et al.*[23], the Wiener filter [24], the SRAD proposed by Yu and Acton [25], and a novel stochastically driven method design specifically for 3D surface rendering from 2D slices of the prostate and other organs. The method we develop specifically for the task of this grant is a stochastically driven compression filter called the squeeze box filter (SBF). Our quantitative evaluation using a Field II [12] simulated B mode ultrasound image with contrast enhancement performance determined by a modified Fisher discriminant has determined that the newly developed SBF method outperformed the other methods and is exceptional in providing the needed intra-region reduction in variance and inter-region contrast enhancement with computational efficiency. In Figs. 7 and 8, we show the results of SBF and SRAD applied to a Field II simulated image. It is visually evident that the bright and dark disks in the SBF result is more pronounced than in the SRAD image. In Figs. 9 and 10, we show the SRAD and SBF results, respectively, using an ultrasound image of a phantom. Again, it is evident that the results of the simulation are up held with the results of the actual ultrasound phantom image in that edges are well preserved and contrast is better enhanced with the SBF than with SRAD. In Figs. 13, 14, and 15, we show the 3D surface, the side view, and the bottom view, respectively, of the rendering we attained from a sequence of scans we acquired of an egg phantom. The sequence consists of acquiring a 2D

slice every millimeter along the long axis of an egg phantom. We processed each slice with the SBF despeckling method. The original unprocessed middle slice is shown in Fig. 11. The SBF processed middle slice is shown in Fig. 12. The 3D rendering was attained by SBF processing each slice then applying a 3D GVF snake to attain the final results shown in Fig. 13, 14, and 15. It is very evident that our method captured the essential size and shape of the egg phantom. The volume estimate we attained for the object enclosed by the surface was only 10% off of the actual volume of the phantom.

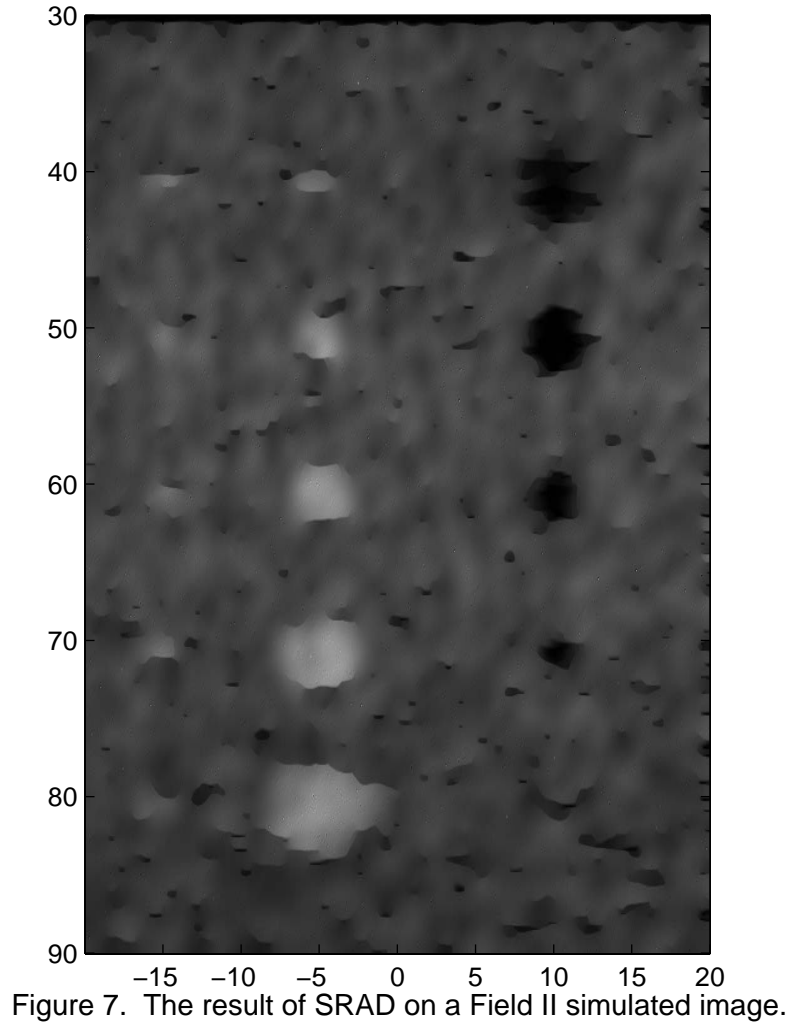
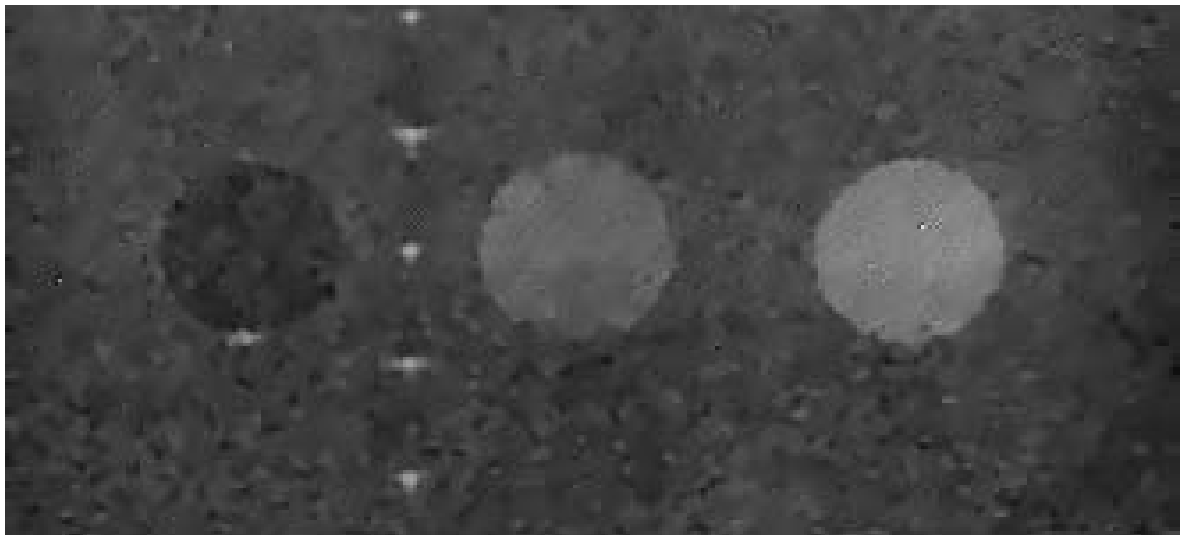
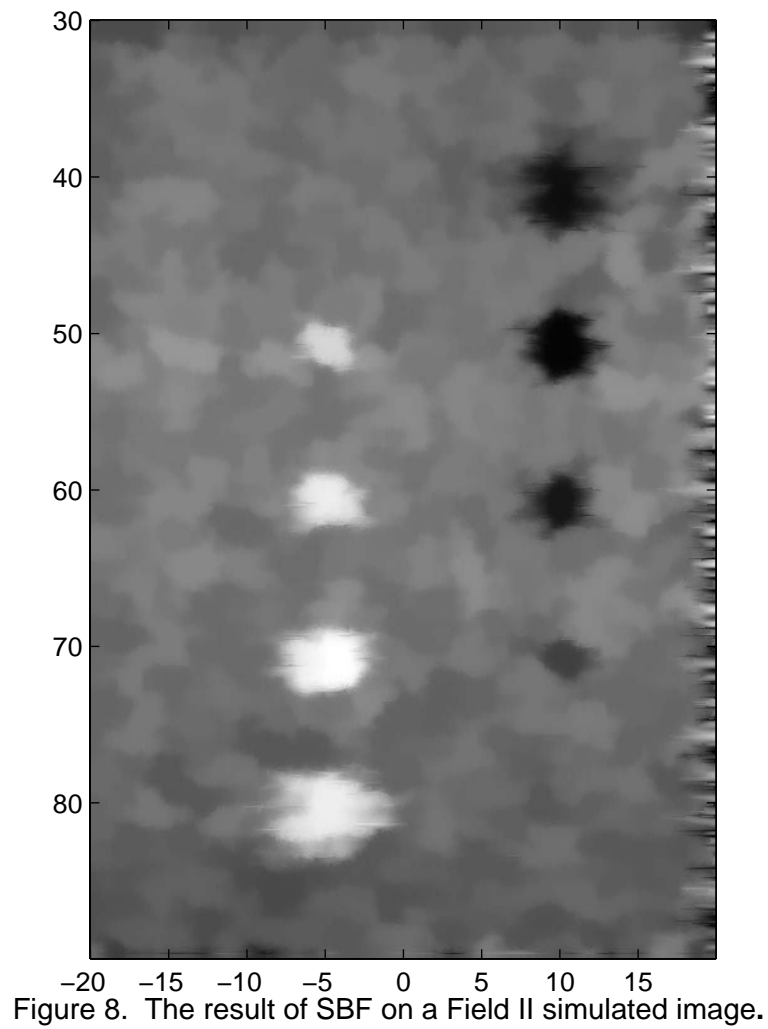


Figure 7. The result of SRAD on a Field II simulated image.



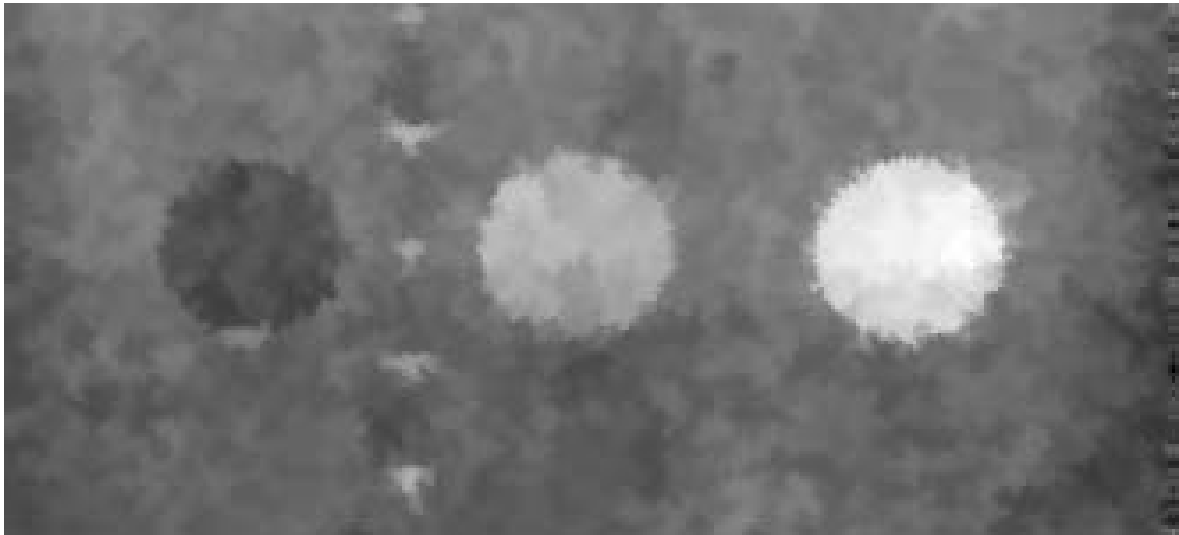


Figure 10. The result of SBF on an actual ultrasound image of a phantom.

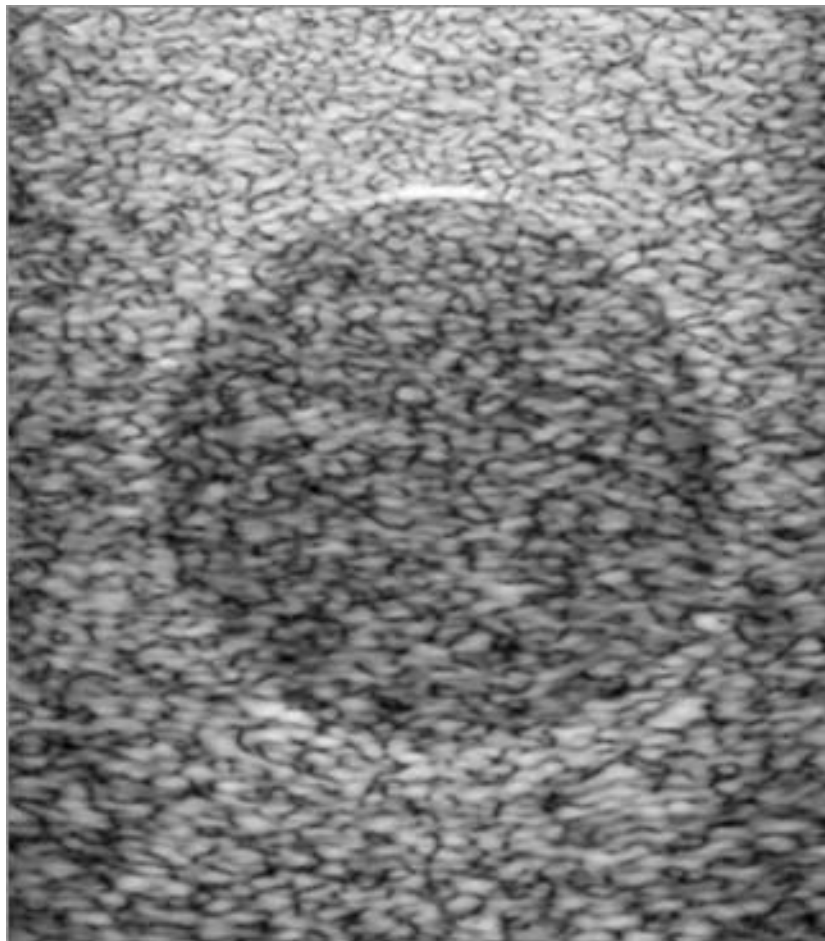


Figure 11. Unprocessed middle slice of the egg phantom.

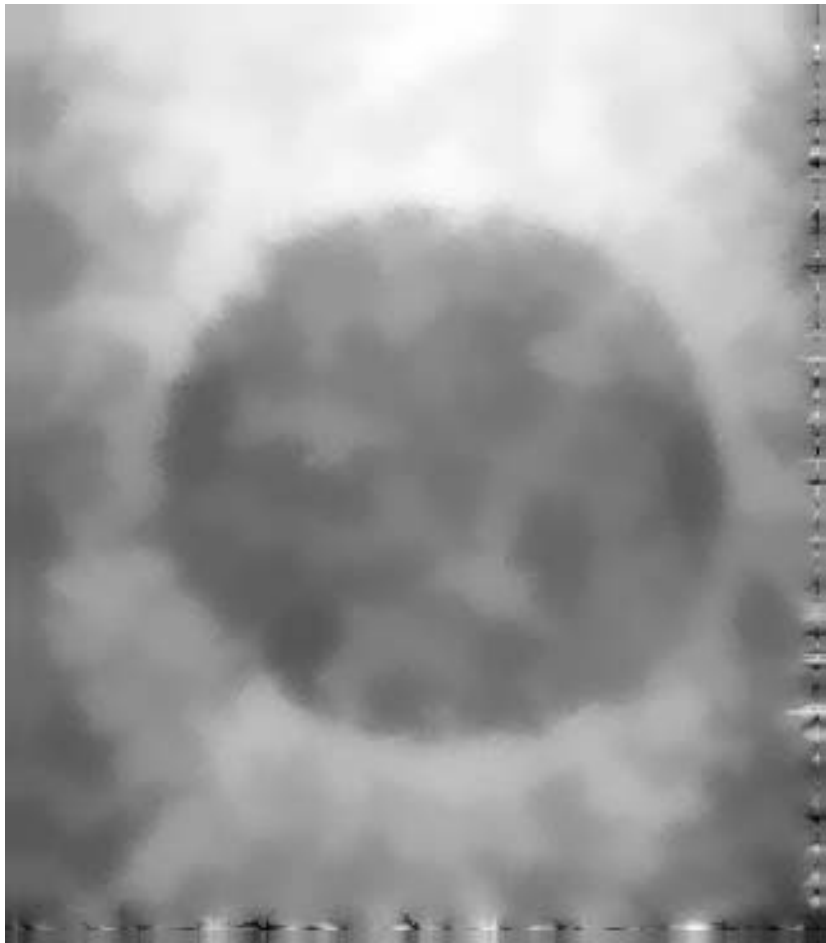


Figure 12. SBF processed middle slice of the egg phantom.



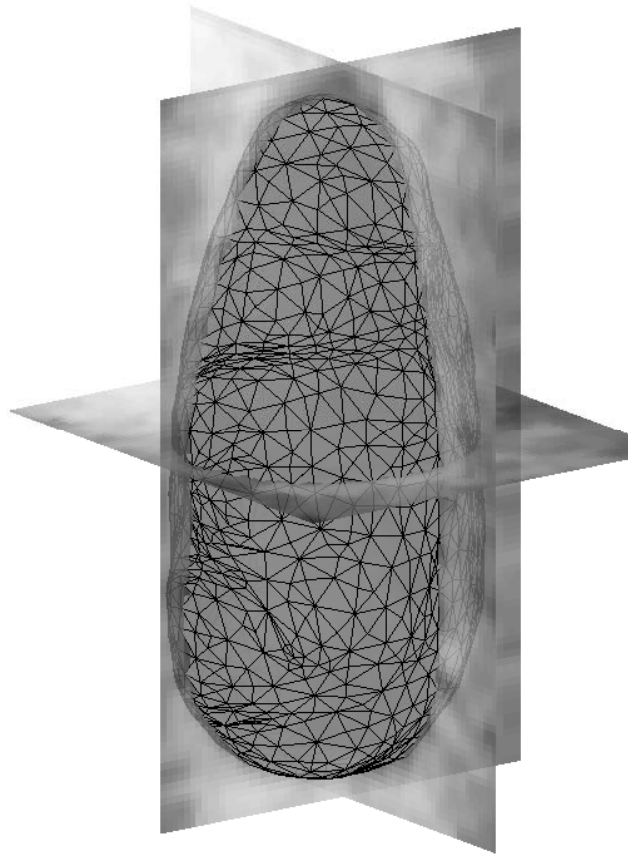


Figure 13. 3D surface found by the 3D GVF with slices preprocessed by SBF.

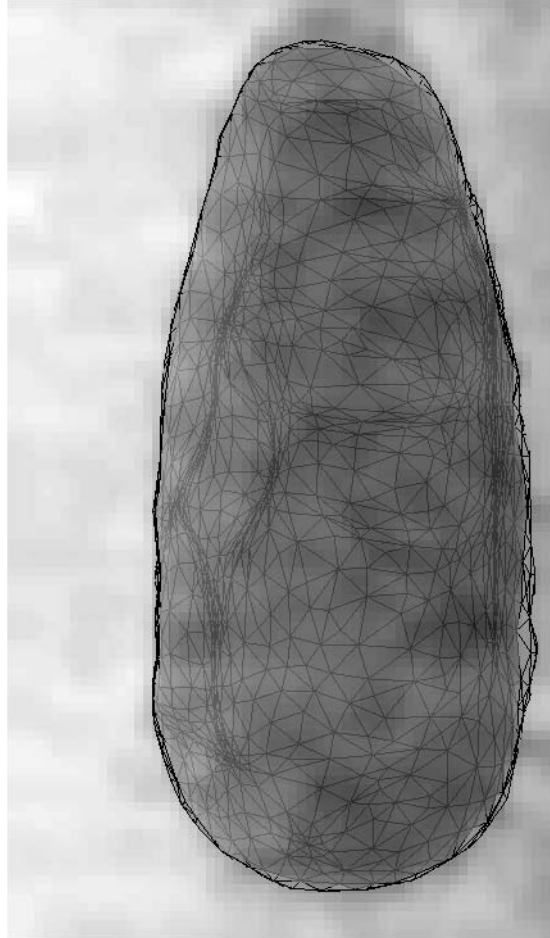


Figure 14. Side view of the surface rendered by the 3D GVF snake with slices preprocessed by SBF.

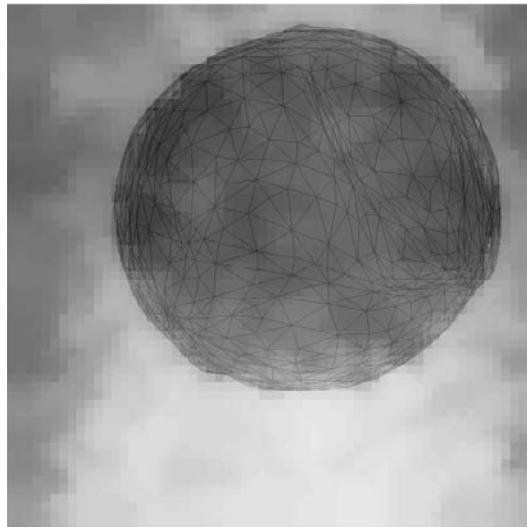


Figure 15. Bottom view of the surface of the egg phantom rendered by the 3D GVF snake with slices preprocessed by SBF.

A conference paper of our novel despeckling method has been peer reviewed and accepted for presentation and publication at the **2006 IEEE International Symposium for Biomedical Imaging: From Nana to Macro** to be held at Crystal Gateway Marriott (Arlington, VA USA) on April 6-9, 2006. Another conference paper that focuses on improvements of the SBF by using a dynamically varying window is under peer review for presentation and publication at the **IEEE International Conference on Image Processing 2006** to be held at Atlanta Marriott Marquis (Atlanta, GA USA) with notification of acceptance due April 17, 2006. A journal paper on the motivation and mathematical foundations of the 1D SBF has been submitted (September 2005) to **IEEE Transactions on Signal Processing** and is current under going the stringent peer review process. A journal paper on the previously mentioned evaluation, 2D SBF, and 3D surface rendering is currently being internally reviewed and we expect a submission to an academically reputable journal in the near future (February 2006).

The future direction of our research in this regards will be to increase the efficiency of our algorithm, improve the 3D GVF snake to incorporate a priori know information such as the approximate size and shape of the prostate, and compare our methods with well established ground truth (we may have to establish this ground truth ourselves).

### KEY RESEARCH ACCOMPLISHMENTS

- We have largely completed Aims 1 and 2. Specifically, we have designed and had fabricated a very high resolution transrectal ultrasound transducer array for high resolution prostate imaging.
- We have integrated the new transducer with an ultrasound scanner and an automated injection stage to realize an accurate elastographic imaging device.
- We have tested the 3D and elastographic imaging capability of the transducer / scanner.
- We have made significant progress in both speckle reduction and in prostate ultrasound feature segmentation for improving and automating the prostate cancer diagnostic process.

### REPORTABLE OUTCOMES

Y. Li, A. Patil and J. A. Hossack, "**High resolution three-dimensional prostate ultrasound imaging**". Presented at SPIE Medical Imaging, San Diego, CA, 2006

Y. Li, A. Patil and J. A. Hossack, "**Combined elasticity and 3D imaging of the prostate**" Proceedings of 2005 IEEE Ultrasonics Symposium, pp.1435-1438, 2005

P. C. Tay, S. T. Acton and J. A. Hossack, "**A Stochastic Approach to Ultrasound Despeckling**", Accepted for presentation at 2006 IEEE International Symposium for Biomedical Imaging: From Nana to Macro Arlington, VA, 2006

P. C. Tay, S. T. Acton and J. A. Hossack, "**Ultrasound Despeckling Using An Adaptive Window Stochastic Approach**", Submitted for presentation at IEEE International Conference on Image Processing 2006

(We have journal papers planned and early preparation in the areas of elastographic imaging and in image speckle reduction.)

### CONCLUSIONS

Our prostate imaging approach combines using an I-Beam transducer with 3D capability, elasticity imaging and test on a prototype using a prostate tissue-mimicking phantom. The prostate strain imaging performed here using a slightly inflated sheath over the transrectal transducer significantly enhanced tumor visibility (a hard inclusion in the phantom). (The lesion was nearly invisible in the regular B-mode image.) The I-Beam transducer enabled reconstruction of discrete 2D image acquisitions into regular 3D grid space, and thus the tumor was rendered in 3D. The volume calculated for this tumor had an error of approximately 11% compared to the actual (independently determined) volume. Additionally, we have made significant progress in the area of image pre-processing (i.e. speckle reduction) and in image

quantification (i.e. feature segmentation). These image processing contributions significantly enhance the practical utility of our technique since they hold the promise of accelerating the prostate cancer diagnostic task and reducing intra and inter operator variability. Reducing variability has significance since serial analysis of cancer growth or remission is dependent on accurate and repeatable measures of prostate volume. Since we are able to measure volumes directly, rather than extrapolating volume from a length dimension or cross-sectional area, our image contributions are well-matched and complement our contributions in 3D and elastographic imaging.

## REFERENCES:

- [1] A. C. Society, "American Cancer Society Prostate Cancer Statistics from [www.cancer.org](http://www.cancer.org)," 2004.
- [2] E. Crawford, S. Leewansangtong, S. Goktas, K. Hothaus, and M. Baier, "Efficiency of Prostate-Specific Antigen and Digital Rectal Examination in Screening, Using 4.0 ng/mL and Age Specific Reference Range as a Cutoff for Abnormal Values," *The Prostate*, vol. 38, pp. 296-302, 1999.
- [3] M. Toubert, M. Schlageter, J. Bron, P. Teillac, A. LeDuc, and Y. Najean, "Screening for cancer of the prostate using prostate-specific antigen," *Presse Medicale*, vol. 19, pp. 1139-1142, 1990.
- [4] F. Frauscher, A. Klauser, E. Halperm, W. Horninger, and G. Bartsch, "Detection of Prostate Cancer with a Microbubble Ultrasound Contrast Agent," *The Lancet*, vol. 357, pp. 1849-1850, 2001.
- [5] J. Taylor, K. Gancarczyk, G. Fant, and D. Mcleod, "Increasing the number of core samples taken at prostate needle biopsy enhances the detection of clinically significant prostate cancer," *Urology*, vol. 60, pp. 841-845, 2002.
- [6] A. Sarvazyan, "Mechanical imaging: a new technology for medical diagnostics," *Journal of Medical Informatics*, vol. 49, pp. 195-216, 1998.
- [7] R. Weiss, V. Hartanto, M. Perrotti, K. Cummings, A. Bykanov, V. Egorov, and S. Sobolevsky, "In vitro trial of the pilot prototype of the prostate mechanical imaging system," *Urology*, vol. 58, pp. 1059-1063, 2001.
- [8] E. Halpern, P. McCue, A. Aksnes, F. Frauscher, and L. Gomella, "Contrast-enhanced US of the Prostate with Sonozone: Comparison with Whole-Mount Prostatectomy Specimens in 12 Patients," *Radiology*, vol. 222, pp. 361-366, 2002.
- [9] R. Clements, "The Role of Transrectal Ultrasound in Diagnosing Prostate Cancer," *Current Urology Reports*, vol. 3, pp. 194-200, 2002.
- [10] L. Negron, F. Viola, E. Black, C. Toth, and W. Walker, "Development and characterization of a vitreous mimicking material for radiation force imaging," *IEEE Transactions Ultrasonics, Ferroelectrics and Frequency Control*, vol. 49, pp. 1543-1551, 2002.
- [11] C. Xu and J. Prince, "Snakes, Shapes and Gradient Vector Flow," *IEEE Trans. Image Processing*, vol. 7, pp. 359-369, 1998.
- [12] J. Jensen and N. Svendsen, "Calculation of Pressure Fields from Arbitrarily Shaped, Apodized and Excited Ultrasound Transducers," *IEEE Transactions on Ultrasonics Ferroelectrics & Frequency Control*, vol. 39, pp. 262-267, 1992.
- [13] J. Hossack, T. Sumanaweera, and S. Napel, "Quantitative 3D Ultrasound Imaging Using an Automated Image Tracking Technique," presented at IEEE Ultrasonics Symposium, 2000.
- [14] P. Phillips, "Contrast Pulse Sequences (CPS): Imaging non-linear microbubbles," *Proceedings of the 2001 IEEE Ultrasonics Symposium*, vol. 2, pp. 1739-1745, 2001.
- [15] A. Lorenz, H. Sommerfeld, M. Garcia-Schurmann, S. Philippou, T. Senge, and H. Ermert, "A new system for the acquisition of ultrasonic multicompression strain images of the human prostate in vivo," *IEEE Transactions on Ultrasonics Ferroelectrics & Frequency Control*, vol. 46, pp. 1147-1154, 1999.
- [16] S. Alam, E. Fellepa, A. Kalisz, S. Ramchandran, R. Ennis, F. Lizzi, C.-S. Wu, and J. Ketterling, "In vivo Prostate Elastography: Preliminary Results," *Proceedings of IEEE Ultrasonics Symposium*, 2004.
- [17] M. Lubinski, S. Emelianov, and M. O'Donnell, "Speckle tracking methods for ultrasonic elasticity imaging using short-time correlation," *IEEE Transactions on Ultrasonics Ferroelectrics & Frequency Control*, vol. 46, pp. 82-96, 1999.
- [18] M. Lubinski, S. Emelianov, K. Raghavan, A. Yagle, A. Skovoroda, and M. O'Donnell, "Lateral Displacement Estimation using Tissue Incompressibility," *IEEE Transactions on Ultrasonics Ferroelectrics & Frequency Control*, vol. 43, pp. 247-256, 1996.
- [19] M. Nagao and T. Matsuyama, "Edge preserving smoothing," *Computer Graphics and Image Processing*, vol. 9, pp. 394-407, 1979.
- [20] J. Lee, "Digital image enhancement and noise filtering by use of local statistics," *IEEE Trans. Pattern Anal. Machine Intell*, vol. 2, pp. 165-168, 1980.
- [21] V. Frost, J. Stiles, K. Shanmugan, and J. Holtzman, "A model for radar images and its application to adaptive digital filtering of multiplicative noise," *IEEE Trans. Pattern Anal. Machine Intell*, vol. 4, pp. 157-166, 1982.
- [22] D. Kuan, A. Sawchuk, T. Strand, and P. Chavel, "Adaptive noise smoothing filter for images with signal-dependent noise," *IEEE Trans. Pattern Anal. Machine Intell*, vol. 7, pp. 165-177, 1985.

- [23] T. Loupas, W. McDicken, and P. Allan, "An adaptive weighted median filter for speckle suppression in medical ultrasonic images," *IEEE Trans. Circuits Syst.*, vol. 36, pp. 129-135, 1989.
- [24] T. Kailath, "Equations of Wiener-Hopf type in filtering theory and related applications," *Norbert Wiener: Collected Works vol. III, P. Masani, Ed., Cambridge, MA: MIT Press*, pp. 63-94, 1976.
- [25] Y. Yu and S. Acton, "Speckle reducing anisotropic diffusion," *IEEE Transactions on Image Processing*, vol. 11, pp. 1260-1270, 2002.

## APPENDICES: Following pages

Y. Li, A. Patil and J. A. Hossack, "**High resolution three-dimensional prostate ultrasound imaging**". Presented at SPIE Medical Imaging, San Diego, CA, 2006

Y. Li, A. Patil and J. A. Hossack, "**Combined elasticity and 3D imaging of the prostate**" Proceedings of 2005 IEEE Ultrasonics Symposium, pp.1435-1438, 2005

P.C. Tay, C. D. Garson, S. T. Acton, and J. A. Hossack, "**Ultrasound Despeckling for 3-D Rendering**" Submitted to IEEE Transactions on Image Processing

P.C. Tay, S. T. Acton, and J. A. Hossack, "**A Stochastic Approach to the Noise Restoration Problems**" Submitted to IEEE Transactions on Signal Processing

P.C. Tay, C. D. Garson, S. T. Acton, and J. A. Hossack "**A Transform Method To Remove Ultrasound Artifacts and Improve Volume Estimates**", Accepted to SSIAI 2006 Symposium

P. C. Tay, S. T. Acton and J. A. Hossack, "**A Stochastic Approach to Ultrasound Despeckling**", Accepted for presentation at 2006 IEEE International Symposium for Biomedical Imaging: From Nano to Macro Arlington, VA, 2006

P. C. Tay, S. T. Acton and J. A. Hossack, "**Ultrasound Despeckling Using An Adaptive Window Stochastic Approach**", Submitted for presentation at IEEE International Conference on Image Processing 2006

# High resolution three-dimensional prostate ultrasound imaging

Yinbo Li, Abhay Patil and John A. Hossack

Biomedical Engineering Department, University of Virginia, Charlottesville, VA  
22908-0759, USA

## ABSTRACT

This work reports on the application of ultrasound elastography to prostate cancer detection using a high resolution three-dimensional (3D) ultrasound imaging system. The imaging was performed at a relatively high frequency (14 MHz), yielding very fine resolution that is optimal for prostate ultrasound imaging. The fine resolution achieved aids in locating smaller lesions than are normally detectable. Elasticity was measured with a quantitative and automatically controlled “Synthetic Digital Rectal Examination (SDRE)” wherein a smoothly increasing force was applied by injecting water, controlled by an electronic syringe pump, into a latex cover over the transrectal transducer. The lesion identified as stiffened tissue was visually enhanced by colorizing and superimposing it over the conventional B-mode image. Experimental results using a tissue-mimicking phantom demonstrated that the reconstruction accuracy of the I-Beam transducer resulted in less than 15% volumetric error. Thus, this high resolution 3D prostate elastography is possible and may provide reliable and accurate determination of the size and the location of cancers, which may result in improved specificity and sensitivity of cancer detection.

**Keywords:** prostate cancer, elastography, 3D ultrasound imaging

## 1. INTRODUCTION

Prostate cancer is the second most prevalent malignant cancer in North American men. In 2004, approximately 230,110 new cases of prostate cancer occurred in the US. According to the American Cancer Society statistics, 29,900 prostate cancer related deaths were anticipated in 2004 [2]. Systematic multi-core biopsy of the prostate, consisting of the acquisition of ten or more biopsy cores distributed throughout the prostate, is the best current test for detecting prostate tumors, but still exhibits a sensitivity significantly less than ideal [3]. Most commonly used approaches for prostate cancer include the digital rectal examination (DRE), and the prostate specific antigen (PSA) blood test. However, the usefulness of DRE is fundamentally limited by its subjective nature, and the PSA presents a significant “gray” area (PSA concentration is between 4 – 10 ng/ml) due to its low sensitivity and specificity [4]. Recent examples of progress in the field of prostate cancer detection include, “mechanical imaging” of the prostate [5] and contrast-enhanced ultrasound [6, 7], but each of these have shortcomings that limit their application in clinical use. Mechanical imaging has shown noticeable improvement in accuracy and sensitivity for *in vitro* cases, while its use of strain gauges and magnetic positioner device may become cumbersome, or even unfeasible, for *in vivo* cases. The cost of contrast agents for prostate cancer diagnosis accounts for almost half of the cost of a conventional ultrasound examination, and therefore represents a considerable financial impediment to the widespread acceptance of contrast in routine prostate cancer ultrasound-based diagnosis. In the recent years, elasticity imaging has garnered attention as a technique that reveals the tissue hardness and thus provides a means that complements anatomic B-Mode imaging with a map of localized regions of abnormal stiffness. Significantly, cancers are frequently associated with local changes in the tissue mechanical properties, or tissue hardness [8]. Techniques like sonoelasticity [9] and transient elastography involve application of low frequency shear waves to a tissue. Difference in tissue elasticity causes change in the velocity of the shear waves through the tissue. This information can be used to reconstruct tissue elasticity modulus. Another ultrasound based elasticity imaging is “elastography” [10]. Elastography has been extensively studied for cancer detection, and has produced promising results both *in vitro* and *in vivo* [11] [12-15]. Elastography involves application of quasi static compression to the tissue; the resultant tissue deformation is obtained by tracking the pre- and the post-compression echo RF data. The tissue deformation, or strain, is an inverse function of tissue elasticity and reveals the mechanical properties of the tissue. This information can be used to differentiate cancers from non-cancers at a relatively early stage as the spatial resolution of

the technique is comparable with that of B-mode ultrasound [16, 17].

One of the challenges in elastography is to classify a detected cancer as malignant or benign, this may potentially help in precluding inessential biopsies. Garra et al.[13] proposed a cancer classification approach based on the size of the cancer as estimated from the elastographic images. It is well known that the benign cancers manifest different shapes from those of the malignant cancers. Hence, shape and size estimation of the cancers based on 3D volume (tomography) imaging holds a key to increasing the sensitivity and the specificity of elastography (strain imaging). No 3D prostate elastography studies have been reported to date. We previously performed 3D reconstruction of the in-vitro prostate inclusion using I-beam transducer operated at 8 MHz [18]. This paper continues the *in vitro* work on 3D prostate elastography using an I-Beam transducer at a high frequency up to 14 MHz, providing higher image resolution and thus more accurate measurement of tumor size and location, especially for the low-volume tumors.

## 2. METHODS

### 2.1 Prostate Phantom

A purpose-built prostate phantom was designed using the method described in Negron et al. [19]. The phantom (Fig. 1) comprises of four components (labeled 1 to 4). A pea-sized (approximately 0.3 ml) lesion mimicking inclusion (referred to as “lesion” hereafter), an egg-shaped tissue mimicking prostate (referred to as “tissue” hereafter) a cylindrical cavity (20 mm in diameter) on top of the egg-shaped surrounding to mimic the anal opening, where the transrectal transducer is placed during screening; and an exterior gel component that encases all the other three components. The lesion is made of 17% (by weight) acrylamide gel; the tissue and exterior component are made of 5% acrylamide gel. Thus, the lesion is perceptibly stiffer (10 times) than both the egg shaped tissue region and the exterior gel component. The lesion and tissue are made echogenic by mixing Sephadex (Amersham Pharmacia Biotech, Piscataway, NJ), which generates speckle in ultrasound imaging. A similar concentration (by volume) of Sephadex was added to both the lesion and the tissue, resulting in similar ultrasound image intensity in these two structures (The lesion was made slightly brighter than the tissue in order to assist navigation during scanning.) A B-mode ultrasound image of the prostate is shown in Fig. 1. The lesion in the image is almost isoechoic.

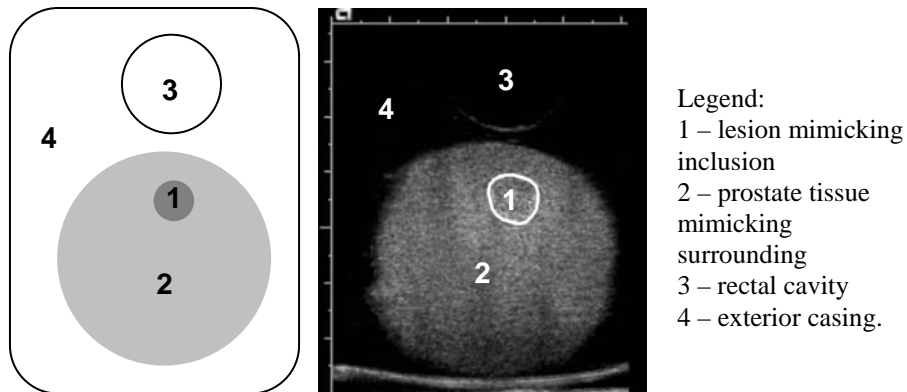


Fig. 1. Left: Schematic of the transrectal design of prostate phantom. Right: An ultrasound image of the phantom.

### 2.2 Imaging

A Siemens Sequoia 512 scanner (Siemens Medical Solutions, Mountain View, CA) and a linear phased-array transrectal transducer operating at 14 MHz were used in this work. Figures 2 and 3 show a photograph of the new, dedicated, high resolution, and 3D capable “I-Beam” [20] transducer that was specifically designed for and used in this work. The I-Beam is a modified 1D linear array transducer, which allows for simultaneous fast acquisition and tracking of the 2D planar images as the transducer sweeps in the elevational direction. This transducer comprises 192, 8-14 MHz elements



on a 0.2 mm pitch for imaging and two pairs of 32 elements on a 0.2 mm pitch, for tracking in 3D space. The I-Beam approach has been previously demonstrated to produce two standard deviation accuracy in the reconstructed (i.e. elevational) direction of 4.6% [20]. The high frequency and long aperture (39.2 mm) of this transducer enables possibly the highest prostate oriented ultrasound imaging resolution yet achieved. We anticipate that this high resolution transducer is capable of more accurately measuring the size and location of the small lesions and we plan to test it *in vivo* in the near future subject to the requisite institutional human subjects protection. In addition, the high image resolution also offers a potential for capturing lesion volumes that go undetected in low resolution imaging systems. The I-Beam transducer is also uniquely matched to this particular application for the following reasons: a) the trans-rectal probe with the tracking mechanism near the transducer prevents any numerical ill-conditioning. b) The I-Beam transducer estimates the relative tissue motion rather than absolute tissue motion, which facilitates efficient and accurate measurements even if there is patient motion of the type that can defeat a 3D system that uses a fixed origin for 3D positioning (eg. Magnetic-based, optical-based, or articulated arm-based positioner.)

A quantitative and controllable “Synthetic Digital Rectal Examination” approach based on automatic water inflation was used to generate a quasistatic stress and to produce tissue deformation. The syringe volume of 60 ml was chosen to provide sufficient water to compress and deform the rectal wall thus providing an optimal tissue strain. The injected water induced uniform stress through the depth of the tissue, which minimized the artifacts due to non-uniformities in the applied stress. Other groups have also adopted similar balloon inflation method, however, those were operated manually [14][15]. Briefly, water was injected with a syringe and ducted via a small tube to the active surface of the transducer that was covered by a latex condom (Instead of securing a tube from outside, an injection port was configured into the transducer.) A programmable syringe pump (PHD 2000, Harvard Apparatus, Holliston MA) was used to motorize the syringe thus minimizing jitter due to undesired manual motion.

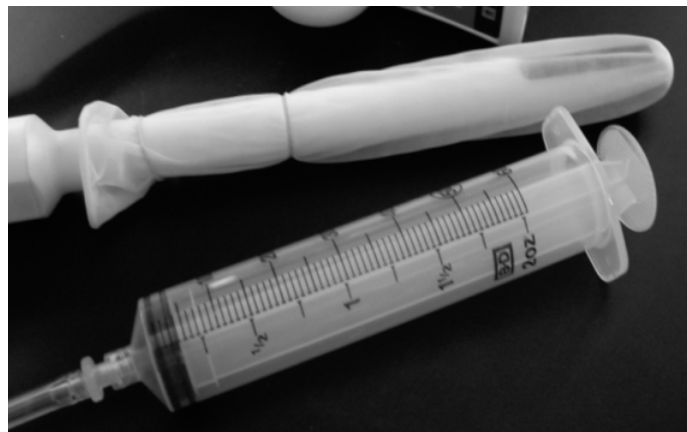


Fig. 2. The transrectal transducer is covered with a latex condom. Water was inflated by the syringe during imaging

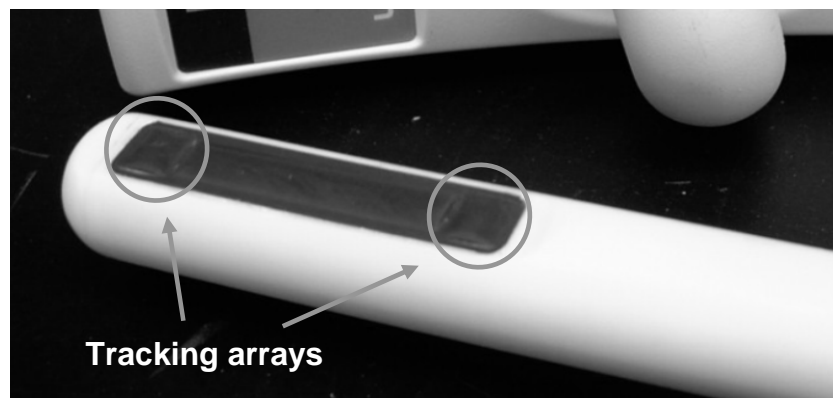


Fig. 3. I-Beam transducer – possessing a main imaging array in the center and a tracking array in each end

Six elevational slices each comprising of 100 IQ data frames were acquired during the in-vitro experiment, such that the incremental strain between the consecutive frames was 0.04 %. Total applied strain between the first and the last frame was approximately 4 %. An example B-mode image obtained by the transrectal I-Beam transducer is shown in Fig. 4.

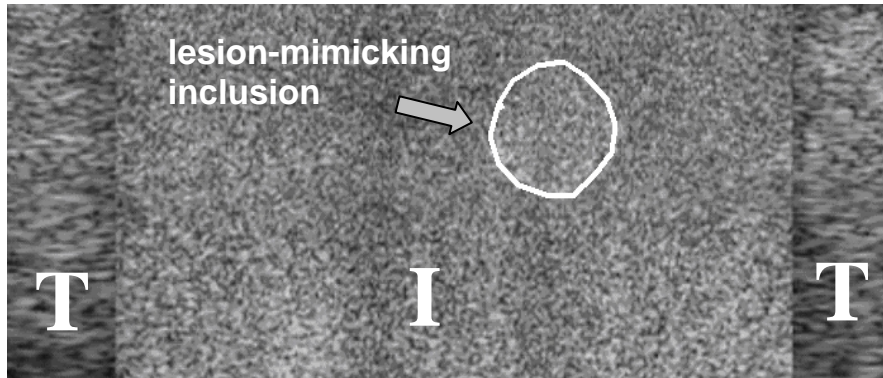


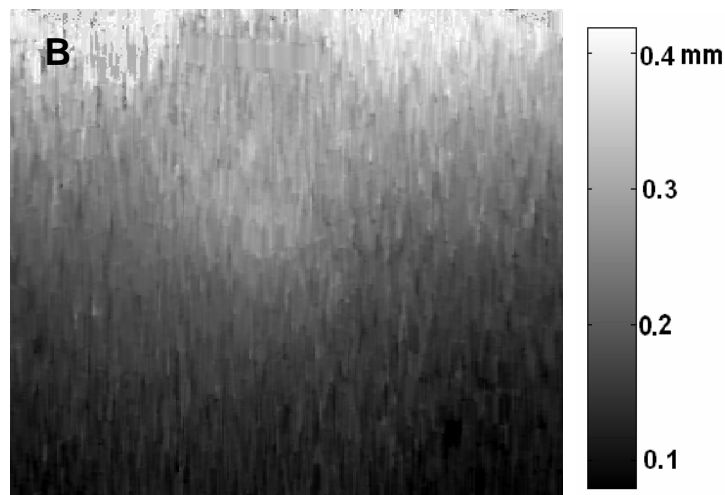
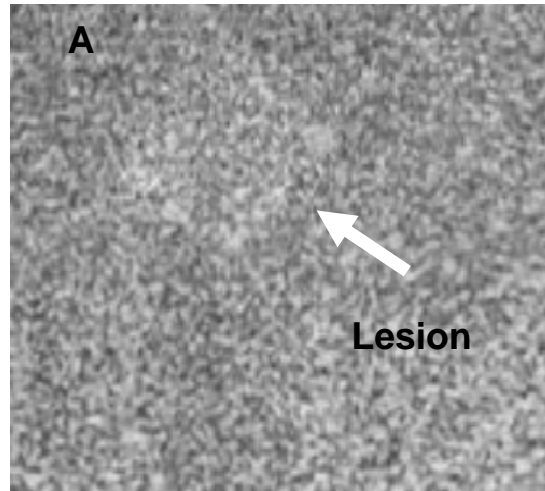
Fig. 4. A B-mode image acquired with the I-Beam transrectal transducer from the prostate-mimicking phantom, showing the layout of image planes formed by 'Tracking' arrays and 'Imaging' array. 'T' – tracking array, 'I' – main imaging array. Delineated is a lesion-mimicking inclusion.

### 2.3 Elasticity Calculation and 3D Reconstruction

An elasticity map was calculated using the acquired data. The data were filtered using a low pass filter to eliminate jitter and electronic noise. Six pairs of frames with differential strain of 2% were tracked using a time-domain cross-correlation technique on complex IQ data. Sub sample precision was acquired in the delay estimates by using a quadratic fit to the cross-correlation function. A search window of approximately 5 wavelengths was used for time-delay estimation. Lateral motion was tracked using the technique described by Lubinski et al. [21]. Displacement estimated from these six different renditions were averaged to eliminate uncorrelated random noise. Strain estimates were obtained by taking the local gradient of the displacement image (in axial direction). The above process was repeated by sweeping the transducer in the elevational direction and six elevational slices were obtained. In the elevation direction, the inter-slice distance was estimated with a block matching approach based upon the minimum sum of absolute differences (MSAD) algorithm of the I-Beam 'Tracking' data. The inter-slice distance was found to be slightly larger in the deeper portion than in the shallower portion, indicating that the transducer was rotated by small angles between measurements. In the measurements, the slices were sampled with an interval no greater than 2 mm, and the rotation angle increments were less than 2 degrees in order to ensure that the elevational motion could be accurately tracked. Once the elevational motion of these blocks was calculated, the acquired image slices were interpolated on to a regular 3D grid in Matlab enabling 3D volumes to be rendered.

## 3. RESULTS

Figure 5 illustrates the lesion detection process. The lesion was detected based on the amplitude of the strain image. A threshold technique, after a 5x5 low pass Gaussian filtering to decrease noise, was applied on the strain image using a threshold value of 0.8%. Low strain regions (i.e. resulting from high stiffness) were rendered using a translucent green mask, superimposed onto the B-mode image so as to maintain the higher spatial resolution of the original B-Mode data while simultaneously highlighting elastically anomalous tissue.



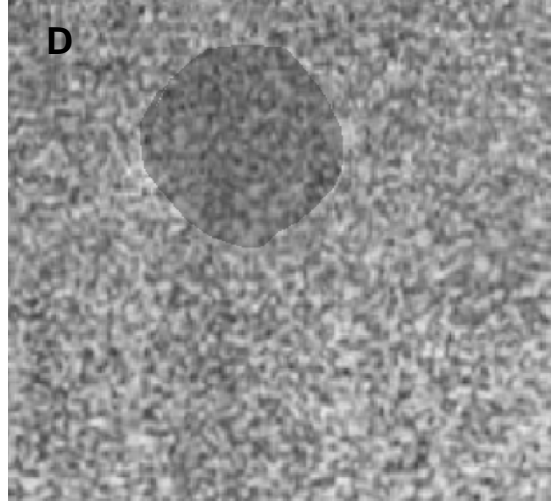
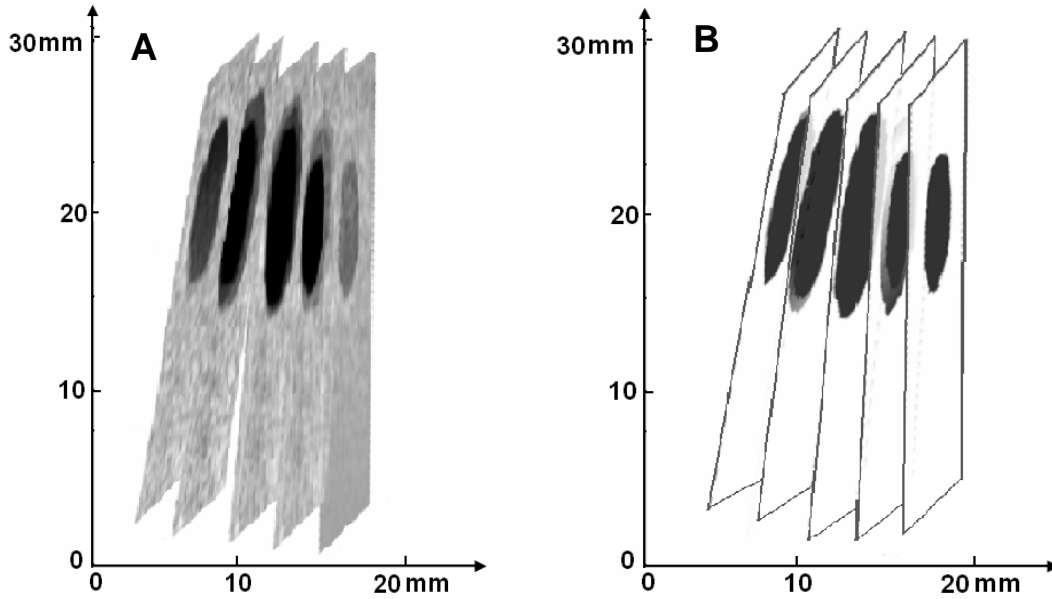


Fig. 5. The lesion detection process. The lesion is barely identifiable in the original B-mode image (A). A displacement image is illustrated in (B). The lesion is clearly identifiable in the strain image (C). Figure (D) is a hybrid B-mode strain image in which the B-Mode image is overlaid with a binary translucent mask outlining a region of enhanced stiffness – as determined by low strain.

The 3D volume of the detected lesion was calculated after segmenting the 2D contour in each slice and estimating the inter-slice distance. A multiple slice view and a 3D surface view of the identified lesion were rendered based on the 3D dataset as shown in Fig. 6. The volume measured in the elastography and 3D reconstruction is approximately  $339 \pm 11 \text{ mm}^3$  less than 15% volumetric error from the volume of  $300 \pm 30 \text{ mm}^3$  measured using Archimedes principle.



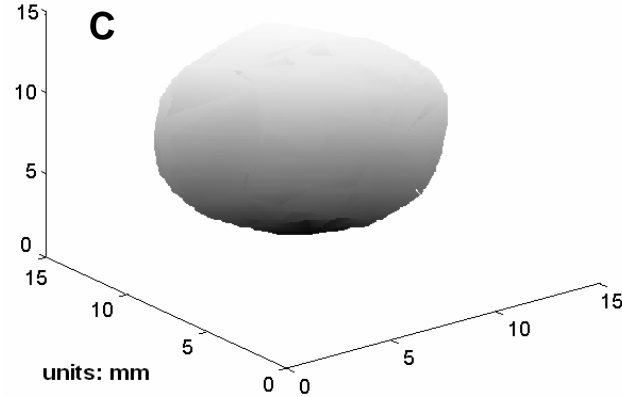


Fig. 6. 3D reconstruction of the lesion. A: The multiple 2D image slices acquired were rendered in three dimensions. The lesion was shown darker than surrounding tissue. B: The multiple slices of elasticity images with the detected lesion shown in black. C: The prostate lesion detected from the ultrasound images. The lesion was segmented from the surrounding tissue and its 3D surface was rendered.

#### 4. DISCUSSION

The approach of water inflation driven by a quantitative and automatic syringe pump proposed in this paper offers the benefits of uniform stress and reduces the non-uniform stress artifacts and out-of-plane problem due to manual motion. In addition, it also provides an opportunity to improve elastographic signal-to-noise ratio and contrast-to-noise ratio by averaging multiple strain estimates from an image sequence, without any loss of axial resolution [17]. Additionally, this quantitative process possesses a high degree of repeatability, which helps to decrease inter-observer variation and is required for longitudinal studies in the setting of cancerous tissue progressing or receding.

#### 5. CONCLUSIONS

We proposed a prostate cancer detection approach combining elasticity and 3D imaging, using an ultrasound system with the exceptionally high precision complex data, and an I-Beam transducer with 3D capability. The approach was tested on a prototype using a prostate tissue-mimicking phantom. The prostate strain imaging performed here using a slightly inflated sheath over the transrectal transducer significantly enhanced tumor visibility (a hard inclusion in the phantom, the lesion was nearly invisible in the regular B-mode image.) The I-Beam transducer enabled reconstruction of discrete 2D image acquisitions (including sets of 2D elasticity acquisitions) in to 3D grid space, and thus allowed the simulated tumor to be rendered in 3D despite the lack of contrast in the original B-Mode images.

#### ACKNOWLEDGEMENTS

Siemens Medical Solutions provided the loan of a Sequoia 512 scanner with research (raw beamformer data) interface and provided engineering support. Vernon SA (Tours, France) fabricated the transrectal I-Beam transducer. This work was supported by US Army CDMRP grant (W81XWH-04-1-0240).

#### REFERENCES

- [1] J. A. Hossack, T. Sumanaweera, S. Napel, and J. Ha, "Quantitative 3D diagnostic ultrasound imaging

- using a modified transducer array and an automated image tracking technique," *IEEE Transactions on Ultrasonics Ferroelectrics & Frequency Control*, vol. 49, pp. 1029-1038, 2002.
- [2] "American Cancer Society, Prostate Cancer Statistics from [www.cancer.org](http://www.cancer.org)," 2004.
  - [3] J. Taylor, K. Gancarczyk, G. Fant, and D. Mcleod, "Increasing the number of core samples taken at prostate needle biopsy enhances the detection of clinically significant prostate cancer," *Urology*, vol. 60, pp. 841-845, 2002.
  - [4] E. Crawford, S. Leewansangtong, S. Goktas, K. Hothaus, and M. Baier, "Efficiency of Prostate-Specific Antigen and Digital Rectal Examination in Screening, Using 4.0 ng/mL and Age Specific Reference Range as a Cutoff for Abnormal Values," *The Prostate*, vol. 38, pp. 296-302, 1999.
  - [5] A. Sarvazyan, "Mechanical imaging: a new technology for medical diagnostics," *Journal of Medical Informatics*, vol. 49, pp. 195-216, 1998.
  - [6] F. Frauscher, A. Klauser, E. Halperm, W. Horninger, and G. Bartsch, "Detection of Prostate Cancer with a Microbubble Ultrasound Contrast Agent," *The Lancet*, vol. 357, pp. 1849-1850, 2001.
  - [7] F. Forsberg, D. Johnson, D. Merton, J. Liu, P. Losco, E. Hagen, and B. Goldberg, "Contrast-Enhanced Transrectal Ultrasonography of a Novel Canine Prostate Cancer Model," *J Ultrasound Med* vol. 21, pp. 1003-1013, 2002.
  - [8] Y. C. Fung, *Biomechanics: Mechanical Properties of Living Tissue*. New York: Springer, 1981.
  - [9] D. Rubens, M. Hadley, S. Alam, L. Gao, R. Mayer, and K. Parker, "Sonoelasticity imaging of prostate cancer: in vitro results," *Radiology*, vol. 195, pp. 379-383, 1995.
  - [10] A. R. Skovoroda, S. Y. Emelianov, and M. O'Donnell, "Tissue Elasticity Reconstruction Based on Ultrasound Displacement and Strain Images," *IEEE, Ultrasonics, Ferroelectrics and Frequency Control*, vol. 42, pp. 747-765 1995.
  - [11] M. O'Donnell, A. Skovoroda, B. Shapo, and S. Emelianov, "Internal Displacement and Strain Imaging Using Ultrasonic Speckle Tracking," *IEEE Transactions on Ultrasonics Ferroelectrics & Frequency Control*, vol. 41, pp. 314-325, 1994.
  - [12] A. Lorenz, H. Sommerfeld, M. Garcia-Schurmann, S. Philippou, T. Senge, and H. Ermert, "Diagnosis of prostate carcinoma using multicompression strain imaging: data acquisition and first in vivo results," presented at IEEE Ultrasonics Symposium, 1998.
  - [13] B. S. Garra, I. Céspedes, J. Ophir, S. Spratt, R. A. Zuurbier, C. M. Magnant, and M. F. Pennanen, "Elastography of Breast lesions: initial clinical results," *radiology*, vol. 202, pp. 79-86, 1997.
  - [14] A. Lorenz, H. Sommerfeld, M. Garcia-Schurmann, S. Philippou, T. Senge, and H. Ermert, "A new system for the acquisition of ultrasonic multicompression strain images of the human prostate in vivo," *IEEE, Ultrasonics, Ferroelectrics and Frequency Control*, vol. 46, pp. 1147-1054, 1999.
  - [15] S. Alam, E. Fellepa, A. Kalisz, S. Ramchandran, R. Ennis, F. Lizzi, C.-S. Wu, and J. Ketterling, "In vivo Prostate Elastography: Preliminary Results," *Proceedings of IEEE Ultrasonics Symposium*, 2004.
  - [16] J. Ophir, S. Alam, F. Kallel, E. Konofagou, T. Krouskop, and T. Varghese, "Elastography: ultrasonic estimation and imaging of the elastic properties of tissues," *Proc. Institution of Mechanical Engineers*, vol. 213, pp. 203-233, 1999.
  - [17] J. Liu, C. K. Abbey, and M. F. Insana, "Linear approach to axial resolution in elasticity imaging," *IEEE, Ultrasonics, Ferroelectrics and Frequency Control*, vol. 51, pp. 716 - 725, 2004.
  - [18] Y. Li and J. Hossack, "Combined elasticity and 3D imaging of the prostate," *Proceedings of SPIE Medical Imaging*, vol. 5750, pp. 7-15, 2005.
  - [19] L. Negron, F. Viola, E. Black, C. Toth, and W. Walker, "Development and characterization of a vitreous mimicking material for radiation force imaging," *IEEE Transactions Ultrasonics, Ferroelectrics and Frequency Control*, vol. 49, pp. 1543-1551, 2002.
  - [20] J. Hossack, T. Sumanaweera, and S. Napel, "Quantitative 3D Ultrasound Imaging Using an Automated Image Tracking Technique," presented at IEEE Ultrasonics Symposium, 2000.
  - [21] M. A. Lubinski, S. Y. Emelianov, K. R. Raghavan, A. E. Yagle, A. R. Skovoroda, and M. O'Donnell, "Lateral Displacement Estimation using Tissue Incompressibility," *IEEE Transactions on Ultrasonics, Ferroelectrics and Frequency Control*, vol. 43, pp. 247-256, 1996.

# Combined elasticity and 3D imaging of the prostate

Yinbo Li, Abhay Patil, John A. Hossack  
Biomedical Engineering Department  
University of Virginia  
Charlottesville, VA 22908-0759

**Abstract**— A 3D volumetric elasticity reconstruction method is proposed for prostate elastography. The method uses crosscorrelation based I/Q data tracking technique in 2D with I-Beam transducer to reconstruct 3D volumetric elastograms. The elevational motion is tracked using block matching based on minimum of the sum-of-absolute differences between the successive elevational frames. 3D elasticity reconstruction estimates the 3D shape and size of cancers, which may be an important step towards their classification as a malignant or a benign.

**Keywords**—elastography, elasticity, prostate, 3D reconstruction, I-Beam.

## I. INTRODUCTION

Adenocarcinoma of prostate is the most prevalent malignant cancer and the second cause of cancer specific deaths in men. Each year there are approximated 220,000 new cases and 28,900 deaths [1]. Current best approaches for detecting a prostate cancer include the digital rectal examination (DRE), and the prostate specific antigen (PSA) blood test. PSA provides the clinician with an indication of the presence of a cancer and hints on its overall development. However, both PSA and DRE exhibit low levels of specificity and sensitivity with latter being a subjective approach. Additionally, prostate cancer is known to possess echogenicity that is similar to that of the surrounding tissue and hence often passes unnoticed in a trans-rectal ultrasound scan [4]. However, cancers are known to be stiffer than the surrounding tissue [11] and hence can be detected by imaging their elastic properties as in ultrasound elastography [15]. Ultrasound elastography involves application of an external compression or stress followed by tracking of the pre- and post-compression radio frequency (RF)/ In-phase/Quadrature (I/Q) echo data to produce maps of internal tissue displacement, spatial derivative of which produces a map of local tissue strains. The advantages of this quantitative technique include a higher sensitivity, repeatability for serial analysis, and a spatial resolution, which is almost in par with the conventional ultrasound B-mode images [3-6]. Previous work on 2D prostate elastography was also reported by Souchon et al. [15] and Alam et al. [2]. In our work we describe an in-vitro 3D volumetric prostate cancer detection technique based on ultrasound elastography. The 3D portion of this work was enabled using an ‘I-Beam’ transducer [7]. Our preferred strain display approach is to colorize the underlying B-Mode image data according to measured strain consequently maintaining a higher spatial resolution of the original B-Mode data.

## II. METHODS

### A. Prostate Phantom

The experiments were performed on a laboratory-built acrylamide based tissue mimicking phantom, prepared with a protocol based on the method by Negron [8]. The phantom comprises four components as shown in figure 1. A pea-sized inclusion is made of 17% (by weight) acryl amide gel to simulate a hard lesion. An egg-shaped surrounding is made of 5% acrylamide gel to mimic the soft prostate tissue. A round cavity (diameter 20 mm) on top of the egg-shaped surrounding holds the transrectal transducer and an outer body, also made of 5% acrylamide gel, encloses all the other three structures. Sephadex was added to provide speckle to the surrounding tissue and the inclusion, but not to the outside body. In the figure 1, on the right, the cavity is obscured in the image because the soft acrylamide-based outer body, which is not echogenic.

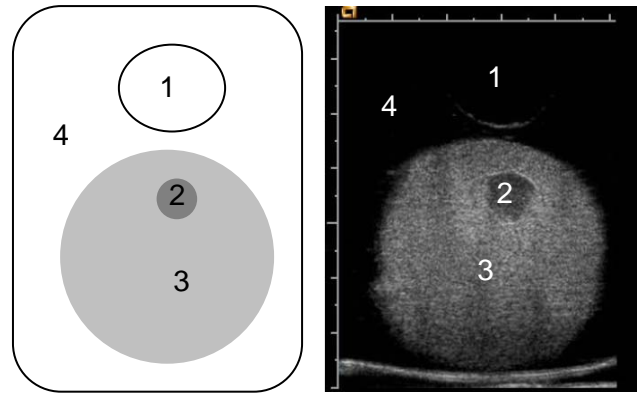


**Figure 1: The prostate phantom, 1-cavity to put probe, 2-pea sized inclusion, 17% acrylamide, 3-prostate tissue, 5% acryl amide, 4-outer body, 5% acryl amide.**

### B. Imaging

The A latex condom over the transrectal transducer was sealed in a conventional manner on the outside surface using elastic bands. The condom was controllably inflated with water using a syringe. The syringe volume of 60mL was chosen to provide sufficient displacement of the rectal wall for a measurable tissue strain signal while intrinsically avoiding the risk of over inflation of the condom. The pressure and displacement are both well within safe limits for in vivo use. During the syringe inflation, a programmable syringe pump (PHD 2000, Harvard Apparatus, Holliston MA) was attached



to the syringe to control the amount and rate of water injection. This permitted a continuous, and uniform inflation process that enabled the image data set to be collected as one image sequence capture process. A Siemens Sequoia 512 scanner (Siemens Medical Solutions, Mountain View, CA) was used in this study. Multiple demodulated (In-phase/Quadrature, I/Q) radio frequency beam-formed lines of acoustic data were acquired from the ultrasound scanner using a research interface employing an IQ data capture board. The data were then analyzed offline on a PC.

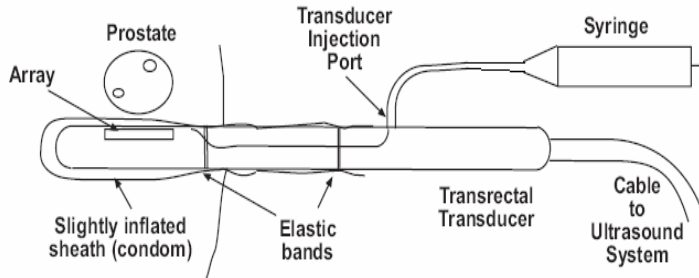


**Figure 2: Schematic setup for prostate elastography.**

The I-Beam transducer allows for simultaneous acquisition and tracking of the 2D planar images as the transducer sweeps across the phantom; it is compatible with our ultrasound biplane trans-rectal probes. The apparatus allows high accuracy in the dimensional measurements with standard deviation of around 4.6% [7]. The I-Beam transducer is also uniquely matched to this particular application for the following reasons: a) the trans-rectal probe with the tracking mechanism near the transducer prevents any numerical ill-conditioning. b) The I-Beam transducer estimates the relative tissue motion rather than absolute tissue motion, for more efficient and accurate measurements [12].

Injection of water in the latex condom results in an application of a controlled stress. This external stress deforms the phantom. The resulting internal displacements are estimated by tracking the pre- and the post-compression I/Q echo data using time-domain crosscorrelation. The shift in the peak of the crosscorrelation function corresponds to the local tissue displacements. The reconstructed tissue displacement image is differentiated to estimate the local strain. Elevational motion is tracked using an I-Beam transducer and block matching using minimum of the sum-of-absolute difference technique. For accurate elevational tracking, the 2D frames were sampled every 2 mm and with less than 3 degrees of angular rotation. The obtained 2D slices were interpolated thus enabling 3D volume rendering using Matlab (Natick, MA).

### III. RESULTS

Figures 3 and 4 illustrate the lesion detection process. The displacement and strain maps were calculated from the I/Q data as discussed above. The reconstructed elastograms were filtered using a 3 X 3 Gaussian filter and time averaged using five independent renditions. Low strain regions (i.e. resulting from high stiffness) were rendered using a translucent green mask, superimposed onto the B-mode image so as to maintain

the higher spatial resolution of the original B-Mode data while simultaneously highlighting elastically anomalous tissue. The volumes calculated from the three independent ultrasound

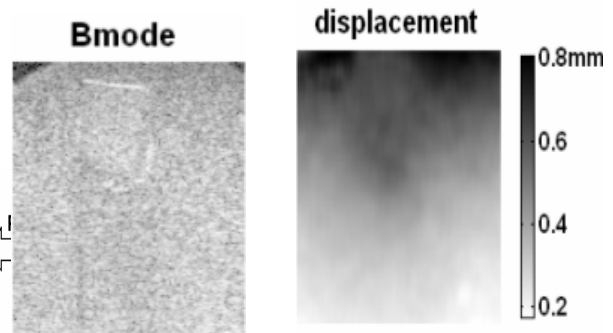


**Figure 3: Observed B-mode image and the internal tissue displacement.**

measurements of this inclusion were 258, 267 and 274  $\mu\text{l}$  corresponding to a mean value of 266  $\mu\text{l}$  with a standard deviation of 8  $\mu\text{l}$ . The volume of the actual inclusion was measured to be approximately 300  $\mu\text{l}$  using Archimedes's principle in a graduated cylinder. The estimated standard deviation of the reconstructed inclusion volume was  $\pm 30 \mu\text{l}$  (10%).

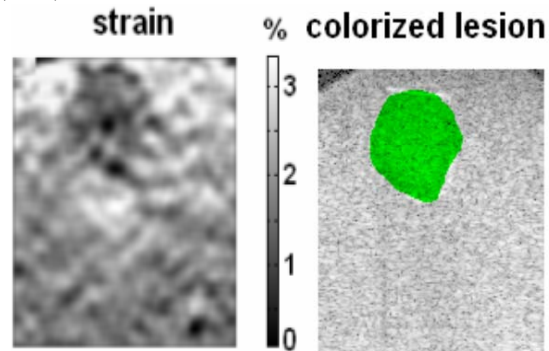


**Figure 4: Reconstructed strain image with the strain superimposed on the B-mode image.**

Nevertheless, this early result is encouraging when taking account of the fact that errors in all three orthogonal directions can compound to degrade the final volumetric accuracy. Furthermore, in previous studies using a transducer with similar acoustic characteristics to the one used here, we obtained a standard deviation of 4.6% in the reconstructed (transducer elevation) dimension [7]. Figures 5 and 6 illustrate the reconstructed volume and the original volume of the inclusion, respectively.



#### IV. DISCUSSION

In this work we have used the base band or I/Q data, which decorrelates much slower than the RF data thereby enabling the imaging of higher induced strains though at a relatively lower resolution [16]. Also, 3D volume rendering may help in better estimating the size and the shape of the detected tumor, which may be of great value in determining whether the tumor is malignant or benign [10]. In addition, we have acquired a transducer with higher center frequency, which will improve

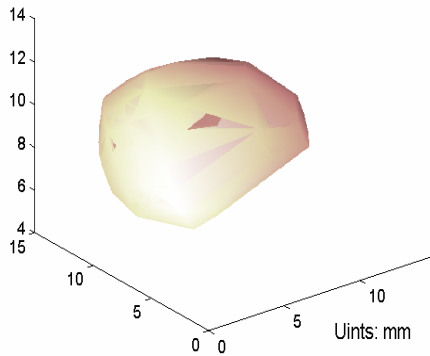


**Figure 5: The re-constructed 3D volume of the pea-shaped inclusion.**

the spatial resolution of the elastographic strain images in the future studies. Figure 7 illustrates the comparison of two B-mode images obtained from the current (8 MHz, spatial resolution of 0.18 mm) and the new (14 MHz, spatial resolution of 0.1 mm) phased-array transducer..



**Figure 6: The original dimensions of the pea-shaped inclusion.**

It is important to note that the speckle pattern in the 14 MHz transducer is finer than that in the 8 MHz. Also, prostate elastography requires imaging of the shallower part of the prostates and hence depth dependent attenuation is minimized with a gain in spatial resolution.

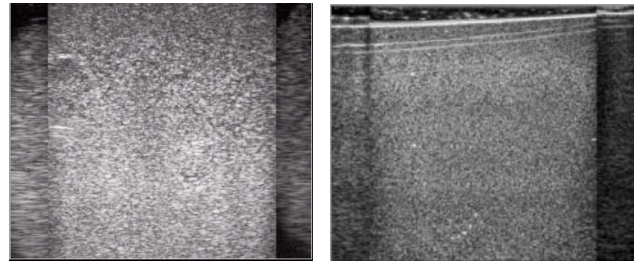


**Figure 7: The B-mode images obtained from the 8 MHz (left) and 14 MHz (right) transducer.**

#### V. CONCLUSIONS

The prostate strain imaging performed here using a slightly inflated sheath over the transrectal transducer significantly enhanced tumor visibility (a hard inclusion in the phantom). (The inclusion was nearly invisible in the regular B-mode image.) The I-Beam transducer enabled reconstruction of discrete 2D image acquisitions onto regular 3D grid space, and thus the tumor was rendered in 3D. The volume calculated for this tumor had standard deviation of approximately 11% compared to the actual (independently determined) volume.

#### ACKNOWLEDGMENTS

Siemens Medical Solutions provided the loan of a Sequoia 512 scanner with research (raw beamformer data) interface and provided engineering support. Vernon SA (Tours, France) fabricated the transrectal I-Beam transducer. This work was financially supported by the Department of Defense Prostate Cancer Research Program (PCRP) of the Office of Congressionally Directed Medical Research Programs (CDMRP) Grant number PC030402.

#### REFERENCES

- [1] Society, American Cancer, Prostate Cancer Statistics from [www.cancer.org](http://www.cancer.org). 2004.
- [2] S. Alam, E.F., A. Kalisz, S. Ramchandran, R. Ennis, F. Lizzi, C.-S. Wu, and J. Ketterling, In vivo Prostate Elastography: Preliminary Results. Proceedings of IEEE Ultrasonics Symposium, 2004.
- [3] Pesavento, A., and A. Lorenz., Real time strain imaging and in vivo applications in prostate cancer. In IEEE Ultrasonics Symposium, **12**, pp.1251-1253, 2001.
- [4] Ophir, J., Alam, S. K., Garra, B.S., Kallel, F., Konofagou, E. E., Krouskop, T. A., and Varghese, T, Elastography: Ultrasonic Estimation and Imaging of the Elastic Properties of Tissues. Journal of Engineering in Medicine, **213**(H3), pp 203-233, 1999.
- [5] Erkamp, R., Exploiting strain-hardening of tissue to increase contrast in elasticity imaging. In IEEE Ultrasonics Symposium. **2**: pp. 1833-1836, 2000.
- [6] Pesavento A, L.A., Ermert H, Sommerfeld H, Garcia-Schurmann M, Senge Th, Philippou S. Frame-to-frame statistics of real-time strain images .In IEEE Ultrasonics Symposium, 2000.
- [7] Hossack, J.A., Sumanaweera, T.S., Napel, S., Ha, J.S, Quantitative 3D Diagnostic Ultrasound Imaging Using a Modified Transducer Array and an Automated Image Tracking Technique. IEEE Transactions on Ultrasonics

- Ferroelectrics & Frequency Control, **49**(8): pp. 1029-1038, 2002.
- [8] Negron, L.A.; Viola, F.; Black, E.P.; Toth, C.A.; Walker, W.F, Development and characterization of a vitreous mimicking material for radiation force imaging. IEEE Transactions Ultrasonics, Ferroelectrics and Frequency Control, **49**(11): pp. 1543-1551, 2002.
  - [9] Hossack, J., T. Sumanaweera, and S. Napel., Quantitative 3D Ultrasound Imaging Using an Automated Image Tracking Technique. In IEEE Ultrasonics Symposium. 2: pp. 1593-1596, 2000.
  - [10] Garra BS, Cespedes EI, Ophir J, Elastography of breast lesions: Initial clinical results. Radiology, **202**, pp. 79-86, 1997.
  - [11] Fung, Y. G., Biomechanical properties of the living tissue. New York Springer, Chapter 7, 1981.
  - [12] R. W. Prager, and R.N.R., Rapid Calibration For 3-D Freehand Ultrasound. Ultrasound in Med. & Biol., **24**(6): pp. 855-869, 1998.
  - [13] Lubinski, M.A.E., S.Y.; O'Donnell, M., Speckle tracking methods for ultrasonic elasticity imaging using short-time correlation. Ultrasonics, Ferroelectrics and Frequency Control, IEEE Transactions on., **46**(1): pp. 82 - 96, 1999
  - [14] Ophir, J., Céspedes, I., Ponnekanti, H., Yazdi, Y. and Li, X., *Elastography: A method for imaging the elasticity of the biological tissue*. Ultrasonic Imaging, **13**, pp. 269-279, 1991.
  - [15] 15. Souchon, R., Hervieu, V., Gelet, A., Ophir, J., Chapelon J. Y., *Human prostate elastography, an in-vitro study* . In Proceedings of IEEE Ultrasonics Symposium, **2**, pp.1251-1253, 2003.
  - [16] 16. Alam, S. K. and Ophir, J, *On the use of baseband and RF signal decorrelation as tissue strain estimators*. Ultras. Med. and Biol., Vol. **23**(9), pp. 1427-1434, 1997.

# Ultrasound Despeckling for 3-D Rendering

Peter C. Tay, *Member, IEEE*, Chris Garson, *Student, IEEE*, Scott T. Acton, *Senior Member, IEEE*, and John Hossack, *Senior Member, IEEE*

## Abstract

Surface rendering of three dimensional (3-D) objects from two dimensional (2-D) images require features such as edges to be accurately delineated and contrast between differing regions to be well pronounce. In this regard, images produced by an ultrasound system are adversely hampered by a stochastic process known as speckle. When a set of 2-D ultrasound slices are used to autonomously render 3-D surfaces, the ambiguities caused by the speckle phenomena prohibit an accurate depiction of an object's surface. In this paper, we objectively evaluate a variety of known despeckling filters to be used as a preprocessing step to remove or reduce speckle from each slice prior to applying a 3-D gradient vector flow active contour to determine the surface of an object. We provide a novel efficient despeckling method that is well suited for this pre-rendering process. This novel despeckling technique visually displays excellent contrast enhancement in both actual and simulated ultrasound images. A quantitative evaluation on simulated ultrasound images and using a relative contrast performance enhancement metric verifies our qualitative evaluation. More importantly, an autonomous 3-D rendering using our novel despeckling method yields an excellent approximation to the object's actual surface. Excellence in the sense the size, shape, and volume estimate of the object enclosed by the surface rendering accurately reflect the size, shape, and volume of the actual object, *resp.*

P. C. Tay and S. T. Acton are with the Dept. of Electrical and Computer Engineering, University of Virginia, Charlottesville, VA 22904 USA (email: ptay@virginia.edu; acton@virginia.edu).

This work was supported by NIH NIBIB grant EB001826 and US Army CDMRP grant (W81XWH-04-1-0240).

# Ultrasound Despeckling for 3-D Rendering

## I. INTRODUCTION

An accurate 3-D rendering of organs such as the heart, kidney, prostate, liver, *etc.*, would in many ways be a beneficial aid to health practioners in diagnosing ailments or assessing the health of that organ. These 3-D renderings are possible by layering 2-D images or slices attained from an incremental scan to construct a 3-D matrix. A 3-D surface of the object can be formed from the 3-D matrix, which hold edge information contained in the 2-D slices. A straightforward method to determine the 3-D surface from the 3-D matrix of 2-D slices is to implement the 3-D version of the gradient vector flow (GVF) active contour (*i.e.* snake). The GVF active contour of Xu and Prince found in [1] is robust in determining the surfaces of objects that are in great generality star convex. The GVF snake derives pixelwise gradient information from either the binary or grayscale edge map. A diffusion of the edge map gradients form a vector flow field. From some initial set of snaxels (short for snake elements and are defined as pixels on the current contour), the GVF iteratively forces the snaxels and the interpolated surface to converge towards strong (well defined) edge or border locations. A surface interpolation using the final set of snaxels determines the 3-D surface of the object.

Before we can apply the 3-D GVF snake to the 3-D matrix composed of 2-D ultrasound images, the speckle in each ultrasound image must be reduced so that a faithful edge map can be determined because the GVF is dependent on this edge map. Although the ultrasound images are affected by a stochastic process seen as a granular pattern commonly known as speckle, the use of ultrasound as an imaging modality is preferred for the following reasons:

- only safe non-ionized sound waves are used in the scanning process;
- the portability of the hardware is advantageous for telemedical purposes or imaging patients where transporting them is problematic;
- cost is inexpensive when compared to other medical imaging modalities; and

- real-time or near real-time functional information such as blood or tissue velocities can easily be attained by taking advantage of the Doppler effect of the sound waves.

Goodman in [2] offers a physical explanation of laser speckle as due to the roughness with respect to the wavelength of the laser on the surface being imaged. The cause of laser speckle can be mathematically models as a sum of a large number of complex phasor, *a.k.a.* a complex random walk. These complex phasors can have a constructive or destructive relationship with each other. Thus bright and dark points can be observed in close proximity of each other. The relationship and relevance of acoustic speckle to laser speckle is given by Abbott and Thurstone in [3]. More relevant and detailed descriptions of ultrasound image formation and the statistics of ultrasound speckle can be found in [4], [5]. From the experimentation performed in [4], the intensity or pre-logarithm compressed enveloped detected amplitudes can be modeled as the multiplicative model given in equation (1)

$$J(n, m) = P(n, m) * (I(n, m)\eta_{\times}(n, m)) \quad (1)$$

where  $\eta_{\times}(n, m)$  is statistically independent of  $I(n, m)$  or as the additive model

$$J(n, m) = P(n, m) * I(n, m) + \eta_{+}(n, m) \quad (2)$$

where  $\eta_{+}(n, m)$  is statistically dependent to  $I(n, m)$ . In both equations (1) and (2), the point spread function (PSF) of the ultrasound imaging system is denoted by the  $P(n, m)$  and maybe spatially varying.

The smoothing of speckle and preservation of edges are in a general sense opposite processes, which are difficult to accomplish concurrently. This problem is not only directly relevant to enhancing ultrasound images, but also relevant to enhancing synthetic aperture radar (SAR), optical laser, and other imaging methods. A wide variety of methods have been proposed to address speckle removal or reduction, commonly referred to as despeckling, with success dependent on improvements to a post-despeckling application or visual interpretation. When addressing speckle as unwanted noise non-linear adaptive filtering [6]–[12] and anisotropic diffusion [13], [14] methods have been proposed. Although other more recent types of methods like multiscale thresholding [15], Bayesian multiscale method [16] or

improvements on existing methods such as those in [17] have been proposed, we restrict our survey to the Wiener filter [18]; the non-linear adaptive methods of Nagao and Matsuyama [6], the Lee filter [7], the Frost *et al.* filter [8], the Kuan *et al.* filter [10]; and the anisotropic diffusion method SRAD [14]. Later in this paper, a quantitative evaluation on the performance of these filters in improving the contrast enhancement will be assessed.

The problem of attaining the noise free unblurred image  $\mathbf{I}$  from a detected image  $\mathbf{J}$ , modeled as in equations (1), (2), or others, is generally considered ill posed, that is, the solution may not be unique or impossible to verify. To state a well posed problem, either the restoration is to be accomplished under some constraints on  $\mathbf{I}$ , *i.e.* regularization [19], [20], or the ideal unblurred noise free image  $\mathbf{I}$  is known *a priori*. The experiments and results using simulated ultrasound images given later in this paper will be in the spirit of the latter. We will evaluate the performance of various sharpening and/or denoising algorithms based on the *a priori* knowledge of the desired image. The general goal of an image restoration or segmentation algorithm should be to decrease the variance in a homogeneous region while distinct regions should be well defined. A novel metric, which is a generalization of the Fisher discriminant, will be given to quantify how well various algorithms achieve this general goal. An evaluation of various despeckling algorithms using simulated ultrasound images will be presented. This evaluation will provide support for the use of a novel stochastically driven compression filter as a preprocessing step prior to 3-D surface rendering using a 3-D GVF snake. We substantiate our results by comparing the 3-D surface rendering produced by the 3-D GVF snake using a human optimized SRAD followed by a morphological hole filling operation with the surface rendering produced by the 3-D GVF snake using our proposed efficient compression method.

## II. VARIOUS DESPECKLING FILTERS

### A. Wiener Filter

Suppose the detected image is given as the additive model in equation (2) where the PSF  $\mathbf{P}$  is known or estimated. Applying the Wiener filter as described in [18] to the detected image  $\mathbf{J}$  results in an ideal

(or approximately ideal) low pass filtered version of the ideal image  $\mathbf{I}$  polluted with the noise component  $\eta_+(n, m)$ , provided that the PSF  $\mathbf{P}$  is an low pass filter. Wiener filtered image  $\tilde{\mathbf{J}}$  is determined as

$$\tilde{\mathbf{J}} \xleftrightarrow{DFT} \hat{\tilde{\mathbf{J}}} = \tilde{\mathbf{P}}\hat{\mathbf{J}} = \tilde{\mathbf{P}} \left\{ \hat{\mathbf{P}}\hat{\mathbf{I}} + \hat{\eta}_+ \right\} \quad (3)$$

where  $\mathbf{P} \xleftrightarrow{DFT} \hat{\mathbf{P}}$  (i.e.  $\mathbf{P}$  and  $\hat{\mathbf{P}}$  are discrete Fourier transform pairs), likewise for  $\mathbf{J}$ ,  $\mathbf{I}$ ,  $\eta_+$  and  $\hat{\mathbf{J}}$ ,  $\hat{\mathbf{I}}$ ,  $\hat{\eta}_+$ , resp.,

$$\tilde{P}(k, l) = \begin{cases} \frac{\hat{P}^*(k, l)}{|\hat{P}(k, l)|^2 + \sigma_{\eta_+}^2} & \text{if } \hat{P}(k, l) \neq 0 \\ 1 & \text{otherwise,} \end{cases} \quad (4)$$

and  $\sigma_{\eta_+}^2$  is the variance of the noise. The fortuitous side of applying the Wiener filter is that edges are in a generally relative sense enhanced. Unfortunately, the Wiener filter indiscriminately enhance the speckle present within a homogeneous region.

It should be noted that the Wiener filter is applied in the *DFT* domain. This requires *a priori* knowledge of the PSF, which for ultrasound images is spatially varying. Even if the spatially varying PSF is known or could be accurately calibrated, incorporating a spatially varying PSF into the Wiener filtering framework is problematic and will be topics for our future research papers.

### B. Nagao Filter

Nagao and Matsuyama in [6] proposed a recursive edge preserving smoothing algorithm. One iteration of this algorithm replaces each pixel value with the mean of some segment  $w_k$  originating from  $J(n, m)$  and the variance of  $w_k$  is the minimum variance attained from a set of variances in all eight directions. Precisely,

$$\hat{J}(n, m) = E(w_k), \quad (5)$$

where  $E(\cdot)$  is the expected value operator,

$$\text{var}(w_k) = \min \{ \text{var}(w_i) \mid \text{for } i = 0, 1, 2, \dots, 7 \}$$

and  $w_0, w_1, w_2, \dots, w_7$  are equal length segments, which originate from  $J(n, m)$  and span all eight directions. This recursion is allowed to continue until convergence in most of the pixel values is established.

This method they claim and empirically show in [6] enhances the edges of an image in addition to adaptively smoothing the image.

Though this method is simplistic, it is evolutionary in which this filter adaptively uses local statistics, variances in the eight different direction, to determine a window to derive a replacement pixel value. In addition, the iterative nature of this method may offset some of the problems with using a fixed window length.

### C. The Lee Filter

Lee in [7] proposed methods to contrast enhance an image and to restore an image corrupted by noise. Lee's noisy image models in [7] are

$$J(n, m) = I(n, m) + \eta(n, m) \quad (6)$$

for the additive noise case and

$$J(n, m) = I(n, m)\eta(n, m) \quad (7)$$

for multiplicative noise. In addition to proposing a method to contrast enhance an image, his paper proposes an adaptive filter to aggressively smooth, via local averaging, in homogeneous regions while regions which contain significant image features such as edges are to be left unmolested.

To emphasize the significance of Lee's contribution in [7], the interrelated contents of his paper, contrast enhancement, additive and multiplicative noise suppression algorithms are briefly and thoroughly described. To enable contrast enhancement, at each pixel Lee's algorithm used a linear rescaling of the local mean summed with the multiplication of a gain applied to the difference of the pixel value with the local mean to determine the new pixel value. Formally, let  $J(n, m)$  be the original pixel value of some image  $\mathbf{J}$ , then the new pixel value  $\hat{J}(n, m)$  is set at

$$\hat{J}(n, m) = g(\mu) + k(J(n, m) - \mu), \quad (8)$$

where  $\mu$  is the local mean. The function  $g(\cdot)$  is a linear rescaling of the mean that is  $g(\mu) = a\mu + b$  where the parameters  $a, b \in \mathbb{R}$  were determined to allow the new pixel value to utilize the full eight bit dynamic



range. As pointed out in [7], if  $0 \leq k < 1$ , then equation (8) determines a smoothing filter, *i.e.*, a low pass filter. When the gain  $k$  is greater than one, then equation (8) attempts to “sharpen” image features that is enhance the edges.

If the image is determined or assumed to be polluted with zero mean additive white noise<sup>1</sup>, then the gain  $k$  is adaptively chosen as a function of the local statistics. To be precise, the new pixel value  $\hat{J}(n, m)$  is set at

$$\hat{J}(n, m) = \mu + k(J(n, m) - \mu) \quad (9)$$

where  $\mu$  is the mean in some window. The gain  $k$  is determined as

$$k = \frac{\sigma^2 - \sigma_\eta^2}{\sigma^2} \quad (10)$$

where  $\sigma^2$  is the local variance in the same window about  $J(n, m)$  that determined  $\mu$  and  $\sigma_\eta^2$  is the global noise variance. When  $\sigma^2 \gg \sigma_\eta^2 \neq 0$ , the gain parameter is less than but approximately one. In which case the filter in equation (9) performs like an identity filter that is  $\hat{J}(n, m) \approx J(n, m)$ . If the local variance  $\sigma^2$  is greater than but nearly equal to the global noise variance  $\sigma_\eta^2$ , then  $\hat{J}(n, m) \approx \mu$  and the filter specified by equation (9) serves as a low pass filter. Since the global noise variance can only be greater than or equal to zero, the gain parameter  $k$  can never exceed one. Thus, in homogeneous regions  $k$  should be set to zero and equation (9) provides local smoothing. When  $J(n, m)$  is determined to be an edge pixel, then  $k$  should be set to one and the pixel is left undeteriorated.

When the image is determined or assumed to be degraded by multiplicative noise as in equation (7), then Lee in [7] approximates the image as an additive noise model of the form

$$\tilde{J}(n, m) = AI(n, m) + B\eta(n, m) + C \quad (11)$$

where  $A, B, C \in \mathbb{R}$  are chosen so that mean square error between the  $J(n, m)$  of the multiplicative model from equation (7) and  $\tilde{J}(n, m)$  of the additive model in equation (11) is minimized. Since the image polluted by multiplicative noise is recast as an image with additive noise, the adaptive filter employed in

<sup>1</sup>Lee in [7] does not specify any distribution on the noise values.

the additive case, given in equation (9), can be used, though the gain parameter  $k$  is redefined. Given an *a priori* determination of the mean and variance of the stationary noise,  $\mu_\eta$  and  $\sigma_\eta^2$  *resp.*, the adaptive gain parameter is determined as

$$k = \frac{\mu_\eta Q}{\mu_I^2 \sigma_\eta^2 + \mu_\eta^2 Q} \quad (12)$$

where  $\mu_I$  is the mean of  $I(n, m)$  determined as

$$\mu_I = \frac{\mu}{\mu_\eta} \quad (13)$$

within some fixed window and  $\mu$  is the local mean of  $J(n, m)$  within the same window. The variable  $Q$  is determined as

$$Q = \frac{\sigma^2 + \mu^2}{\sigma_\eta^2 + \mu_\eta^2} - \mu_I^2 \quad (14)$$

where  $\sigma^2$  is the local variance of  $J(n, m)$  within some window.

Lee's modification of the adaptive approach of R. Wallis<sup>2</sup> is a significant contribution because his method incorporated local statistics of an image to determine the gain parameters of an adaptive filter to smooth additive or multiplicative noise. Discouragingly, the Lee filter relies on an unrealistic approximation of the local mean of the ideal image  $\mu_I$  given in equation (13). This is not favorable, since this approximation is difficult (if not impossible) to verify its accuracy and can be considered a blind variable.

#### D. The Frost Filter

Frost, Stiles, Shanmugan, and Holtzman in [8] derived that an image recorded from a synthetic aperture radar system can be modeled as a PSF applied to an ideal image polluted by multiplicative noise. Their image model is given in equation (1). Their goal in [8] was to apply an optimum minimum mean squared error (MMSE) filter to estimate the local regions of a ideal image while avoid degrading edge features. The motivation of Frost *et al.*'s method consist of determining a filter  $f(n', m')$ , so that in a local homogeneous region of  $J(n, m)$  and in the presence of white noise, the expectation criteria

$$E[(I(n, m) - \tilde{I}(n, m))^2] \quad (15)$$

<sup>2</sup>The reference to R. Wallis' contributions is cited in [7].

is minimized. The term  $\tilde{I}(n, m)$  is a windowed weighted sum about  $I(n, m)$ . Formally,

$$\tilde{I}(n, m) = \sum_{n'=-\lfloor \frac{N'}{2} \rfloor}^{\lfloor \frac{N'}{2} \rfloor} \sum_{m'=-\lfloor \frac{M'}{2} \rfloor}^{\lfloor \frac{M'}{2} \rfloor} f(n', m') I(n + n', m + m') \quad (16)$$

where  $\lfloor x \rfloor$  denotes the greatest integer less than or equal to  $x$  and  $N' \times M'$  is the window size. Normally,  $N'$  and  $M'$  are equal and odd. Under the assumption that the noise is white and the transfer function of the PSF is constant over some finite bandwidth, they derived the filter that minimizes (15) as

$$f(n', m') = K \alpha e^{-\alpha |\tau(n', m')|} \quad (17)$$

where

$$\alpha = \sqrt{2a \left( \frac{\mu_\eta}{\sigma_\eta} \right)^2 \left( 1 + \left( \frac{\mu}{\sigma} \right)^2 \right)^{-1} + a}, \quad (18)$$

$K$  is some normalizing constant,  $a$  is an region dependant constant,  $\mu_\eta$  is the mean of the noise,  $\sigma_\eta$  is the standard deviation of the noise,  $\mu$  is the local mean in some window about  $J(n, m)$ , and  $\sigma$  is the local standard deviation of  $J(n, m)$  within the same window that is used to determine the mean. The window size used to determine the local mean and local variance of  $J(n, m)$  does not necessarily have to equal the weighting window size,  $N' \times M'$ . The function  $\tau : \mathbb{Z} \times \mathbb{Z} \longrightarrow \mathbb{R}$  was not explicitly specified in [8]. Rather, a description of  $\tau(n, m)$  was simply given as a monotonically decreasing function. This can be achieved, for example, when  $\tau(n, m) = \sqrt{n^2 + m^2}$  for  $n = \left[ -\frac{\lfloor N' \rfloor}{2}, \frac{\lfloor N' \rfloor}{2} \right]$  and  $m = \left[ -\frac{\lfloor M' \rfloor}{2}, \frac{\lfloor M' \rfloor}{2} \right]$ . The window dimensions  $N'$  and  $M'$  are usually odd and equal.

#### E. The Kuan Filter

Kuan, Sawchuk, Strand, and Chavel in [9] develop a nonlinear filter that they claim in a local neighborhood provides a linear minimum mean square error (LLMMSE) estimate  $\hat{I}(n, m)$  of the ideal noise free image  $I(n, m)$  from the sensed or detected image  $J(n, m)$ . In 1987, Kuan *et al.* published the application of the LLMMSE estimate to image restoration in [10]. The LLMMSE estimate of the ideal noise free image is given as

$$\hat{I}(n, m) = \mu + \frac{\omega^2 - \sigma_\eta^2}{\omega^2} (J(n, m) - \mu) \quad (19)$$

where  $\mu$  is the local variance in some window about  $J(n, m)$  and  $\omega^2$  is the local variance in some weighted window about  $J(n, m)$ . The local weighted variance  $\omega^2$  is defined as

$$\omega^2 = \frac{1}{N'M'} \sum_{n'=-\lfloor \frac{N'}{2} \rfloor}^{\lfloor \frac{N'}{2} \rfloor} \sum_{m'=-\lfloor \frac{M'}{2} \rfloor}^{\lfloor \frac{M'}{2} \rfloor} w(n', m') (J(n + n', m + m') - \mu)^2 \quad (20)$$

where  $\sum_{n', m'} w(n', m') = 1$ ,  $N'$  and  $M'$  are typically odd and equal.

#### F. The Adaptive Weighted Median Filter

Loupas, McDicken, and Allan in [11] develop a filter they named the adaptive weighted median filter (AWMF). The AWMF was specifically designed to suppress speckle noise inherent to ultrasound images. It is should be noted that the motivation for the AWMF is motivated by the following ultrasound image model

$$J(n, m) = I(n, m) + \sqrt{I(n, m)}\eta(n, m). \quad (21)$$

It is easily derived from the image model given in equation (21) that the local variance of the observed image  $J(n, m)$  in a homogeneous region is proportional to the noise variance, provided that the  $\eta(n, m)$  is independent of  $I(n, m)$ . Precisely, let the ideal image be equal to a constant  $c$  in some local neighborhood,  $I(n, m) = c$ , then

$$\sigma^2 = c\sigma_\eta^2 \quad (22)$$

where  $\sigma^2$  and  $\sigma_\eta^2$  are the local variance of the observed image and the variance of the wide sense stationary noise, *resp.* With this motivation Loupas *et al.* defines the AWMF as

$$\hat{J}(n, m) = \text{median} \left\{ \underbrace{J(n + n', m + m'), J(n + n', m + m'), \dots, J(n + n', m + m')}_{w(n', m')} \right\}_{\forall n', m' \in [-\lfloor \frac{N'}{2} \rfloor, \lfloor \frac{N'}{2} \rfloor]} \quad (23)$$

where  $w(n', m')$  is a nonnegative integer. Loupas *et al.* in [11] defined the  $N' \times N'$ , where  $N'$  is odd, window of weight terms as

$$w(n', m') = \text{round}_{\text{nonneg}} \left\{ w(0, 0) - \frac{c\sigma^2 \sqrt{n'^2 + m'^2}}{\mu} \right\} \quad (24)$$

where  $\text{round}_{\text{nonneg}}\{\cdot\}$  means round to the nearest non-negative integer,  $c$  is some constant,  $\mu$  is the local mean, and  $\sigma^2$  is the local variance. The constant  $c$  and the window term  $w(0,0)$  determines the AWMF's ability to preserve edges.

### G. Speckle Reducing Anisotropic Diffusion

Inspired by the time dependant heat diffusion equation, Perona and Malik in [13] published a method to perform anisotropic diffusion on noisy images. In [13], the diffusion equation of an image with continuous variables over time  $J(x, y, t)$  is given as

$$J(x, y, t) = \text{div}\{c(x, y, t)\nabla J(x, y, t)\} = c(x, y, t)\nabla^2 J(x, y, t) + \nabla c(x, y, t) \cdot \nabla J(x, y, t) \quad (25)$$

where  $(x, y, t) \in \mathbb{R}^3$ ,  $\text{div}$  is the divergence operator,  $\nabla$  is the gradient operator,  $\nabla^2$  is the Laplacian operator,  $\mathbf{v} \cdot \mathbf{w}$  represents the dot product of two vectors, and  $J(x, y, 0) = J(x, y)$ . When  $c(x, y, t)$  is a constant, then equation (25) defines isotropic diffusion. For anisotropic diffusion, the function known as the conduction coefficient (*a.k.a.* coefficient of variation, diffusion coefficient)  $c(\cdot)$  is given as

$$c(x, y, t) = \exp\left(-\left(\frac{\|\nabla J(x, y, t)\|}{K}\right)^2\right) \quad (26)$$

or

$$c(x, y, t) = \left(1 + \left(\frac{\|\nabla J(x, y, t)\|}{K}\right)^2\right)^{-1} \quad (27)$$

where  $K$  is some constant and  $\|\cdot\|$  is the norm.

Yu and Acton in [14] proposed a anisotropic diffusion method where the coefficient of variation is determined as a function of the ratio of the instantaneous variance to the instantaneous mean squared. In other words, their speckle reducing anisotropic diffusion method, which they acronymically named SRAD, utilizes the instantaneous coefficient of variation (ICOV) as a variable in their conduction coefficient function. The ICOV of SRAD determine whether a pixel should be smoothed or left unbludgeoned. The SRAD algorithm iteratively processes a nonzero valued image  $I(x, y) := I(x, y; 0)$  according to

$$\frac{\partial I(x, y; t)}{\partial t} = \text{div}[c(q)\nabla I(x, y; t)] \quad (28)$$

and

$$\left. \frac{\partial I(x, y; t)}{\partial \vec{n}} \right|_{B(\Omega)} = 0 \quad (29)$$

where  $\vec{n}$  is the outward normal vector to  $B(\Omega)$ , the border of  $\Omega$ . Equations (28) and (29) are known as the SRAD partial differential equations (PDEs). The diffusion coefficient  $c(\cdot)$  is defined either as the quotient

$$c(q(x, y; t)) = \frac{q_0^4(t) + q_0^2(t)}{q_0^4(t) + q^2(x, y; t)} \quad (30)$$

or as the exponential function

$$c(q(x, y; t)) = \exp \left( \frac{q_0^2(t) - q^2(x, y; t)}{q_0^4(t) + q_0^2(t)} \right). \quad (31)$$

In both equations (30) and (31), if  $q(x, y; t) \approx q_0(t)$ , then  $c(q(x, y; t)) \approx 1$  and smoothing with respect to equation (28) is enacted. If  $q(x, y; t) \gg q_0(t)$ , then the diffusion coefficient is very small and smoothing in a local region around  $(x, y)$  is averted. When at time  $t$ , if  $(x, y)$  resides in a homogeneous region, then smoothing can be promoted by allowing  $q(x, y; t) \approx q_0(t)$ . When  $(x, y)$  lie on an edge or in the vicinity of an edge, then defining  $q(x, y; t) \gg q_0(t)$  would prohibit deterioration of the edge. Yu and Acton defined  $q_0(t)$ , the coefficient of variation in fully developed speckle, as the ratio of the noise standard deviation to the noise mean,

$$q_0(t) = \frac{\sigma_\eta(t)}{\mu_\eta(t)}, \quad (32)$$

and the instantaneous coefficient of variation is defined as

$$q(x, y; t) = \sqrt{\frac{\frac{1}{2} \left( \frac{|\nabla I|}{I} \right)^2 - \frac{1}{16} \left( \frac{\nabla^2 I}{I} \right)^2}{\left( 1 + \left( \frac{1}{4} \right) \left( \frac{\nabla^2 I}{I} \right)^2 \right)}}. \quad (33)$$

The standard deviation and the mean of the noise in equation (32) are determined by calculating the mean and standard deviation within a homogeneous region where noise is prevalent.

The coefficient of variation used in equations (26) and (27) rely solely on the gradient norm. The inclusion of the Laplacian operator in determining the instantaneous coefficient of variation defined in equation (33) and the characterization of fully developed speckle by equation (32) provides a more robust method to determine the diffusion coefficient defined in equation (30) or (31) within different possibly

disconnected region. Lastly, it should be noted that though we outlined the intuitive ideas of SRAD using continuous variables  $(x, y, t) \in \mathbb{R}^3$ , our implementation of SRAD used in the evaluation given in section IV of this paper is the discrete form detailed in [14].

### III. A STOCHASTICALLY DRIVEN METHOD

With the exception of the Wiener filter, the despeckling methods described in section II evaluate every sample in a image and adaptively determines whether to smooth (locally average) or not. The Wiener filter relies on *a priori* knowlegde of the PSF and the noise variance to determine a convolution kernel, which is applied to every pixel in the entire image. The iterative filtering method we presented in this section only considers samples which are outliers of some probability density function (PDF) and applies local smoothing to these outliers. The local extrema are considered outliers and are not used in the determination of the local mean. The choice of the neighborhood  $\mathcal{N}$  is extremely important, since the mean of some PDF is determined by samples in  $\mathcal{N}$ . A large neighborhood fully contained in a homogeneous region will produce a local mean that is closer to the mean of the homogeneous region. Yet, a neighborhood that is too large will extend pass the homogeneous region and yield a local mean, which will erroneously reflect the mean of the homogeneous region. Each iteration of the method currently being described produces a sequence with locally reduced variance. The local extrema of the new sequence are consider as outliers and the process is iterated. The steps of our proposed iterative method are as follow:

- 1) Each iteration  $i$  begins by determining the set of locations of local maxima and local minima. The locations of these extrema are defined by the set

$$\mathcal{N}_E = \{(n, m) \mid J_{i-1}(n, m) \text{ meets condition 1 or 2} \}$$

Condition 1:  $J_{i-1}(n, m) > J_{i-1}(n + k, m + l)$

Condition 2:  $J_{i-1}(n, m) < J_{i-1}(n + k, m + l)$

where  $k, l = -1$  or  $1$ .

- 2) Without using the local extrema values, our algorithm replaces the extremum with the local mean taken from neighboring samples. For all  $(n, m) \in \mathcal{N}_E$

$$J_i(n, m) = \frac{1}{|\mathcal{N}|} \sum_{(k,l) \in \mathcal{N}} J_{i-1}(k, l) \quad (34)$$

where  $\mathcal{N}$  is some local neighborhood of  $(n, m)$ ,  $|\mathcal{N}|$  is the cardinality of set  $\mathcal{N}$ , and  $(n, m) \notin \mathcal{N}$ .

- 3) If convergence is not attained, that is

$$\sum_{\forall n, m} |J_{i-1}(n, m) - J_i(n, m)| > \epsilon \quad (35)$$

for some predefined  $\epsilon > 0$ , then another iteration is performed. If convergence is attained, then only further trivial insignificant improvements can be attained with this filtering method and the process is stopped.

By removing outliers at each iteration, this method reduces the local variance at each pixel. In effect, this method produces a convergent sequence of images by squeezing or compressing the stochastically distributed pixel values to a limiting value. Thus, we call this stochastically driven method the squeeze box filter (SBF).

#### IV. EVALUATIONS AND RESULTS

##### A. Using Simulated Images

To evaluate the despeckling performance of the Wiener filter, the various adaptive non-linear filters, and the anisotropic diffusion method SRAD against the stochastically driven SBF method, four templates were created and are denoted as  $\mathbf{T}^I$ ,  $\mathbf{T}^{II}$ ,  $\mathbf{T}^{III}$ , and  $\mathbf{T}^{IV}$ . These templates represent the ideal noise free images and are shown in the top row of Fig. 1. The pixel values of the background class of all templates are set at one. Templates  $\mathbf{T}^I$  and  $\mathbf{T}^{II}$  consist of two classes: the background class, shaded in black for  $\mathbf{T}^I$  and white for  $\mathbf{T}^{II}$ ; and a class consisting of ten disks of various size, shaded in white and with pixel values five for  $\mathbf{T}^I$ , and for  $\mathbf{T}^{II}$  this class is shaded as black and the pixel values are set at zero. Templates  $\mathbf{T}^{III}$  and  $\mathbf{T}^{IV}$  consist of three classes: the background class, which is shaded in gray; a class consisting



of five disks of various diameter shaded in white with the pixel values set at five for  $\mathbf{T}^{III}$  and zero for  $\mathbf{T}^{IV}$ , shaded in black; the third class is composed of five disks of various diameters, shaded in black and with pixel values set at zero for  $\mathbf{T}^{III}$  and for  $\mathbf{T}^{IV}$  this class is shaded in white and with pixel values set at five.

The Field II simulation [21] of the four templates are shown in the bottom row of Fig. 1 and are denoted as  $\mathbf{J}^I$ ,  $\mathbf{J}^{II}$ ,  $\mathbf{J}^{III}$ , and  $\mathbf{J}^{IV}$ . The simulations are constructed with the transducer at the top of the image. The focus point for each simulation is set at 70mm axial distance from the transducer and at lateral position 0mm. In each simulation, the spatial varying PSFs are shown along the column at lateral position -15mm at axial distances 40mm, 50mm, 60mm, 70mm, and 80mm.

To evaluate which method in sections II and III provide the best improvements to an ultrasound image a meaningful quantifiable measure and a method to attain this measure is needed. This measure should indicate when different homogeneous regions are properly defined. Additionally, this metric should account for differences in pixel values from the mean of a class. A class is taken to be a collection of homogeneous regions. This measure in essence will determine how well an algorithm despeckles the simulated ultrasound image while keeping the distinct classes well separated.

The method we propose to quantify the improvements made to an ultrasound image is as follow:

- 1) First, we create the ideal image that is a template  $\mathbf{T}$  with various classes  $C_1, C_2, C_3, \dots, C_N$ .
- 2) A simulation of an ultrasound image  $\mathbf{J}$  using the template  $\mathbf{T}$  is accomplished via the Fields II software.
- 3) A despeckling algorithm is applied to the simulated image  $\mathbf{J}$ . The output image is denoted as  $\mathbf{I}_{alg}$ .
- 4) The means and variances in each predefined classes of  $\mathbf{I}_{alg}$  are computed.
- 5) The ratio of the average squared differences of the inter-class means to the sum of the intra-class variances are calculated and this quantity is denoted as  $Q_{\mathbf{I}_{alg}}$ . Explicitly, the quantity to evaluate the performance of an despeckling algorithm to preserve distinct classes and promote smoothing within

homogeneous regions of each class is given as

$$Q_{\mathbf{I}_{alg}} \stackrel{def}{=} \frac{\sum_{k \neq l} (\mu_{C_k} - \mu_{C_l})^2}{(N-1) \sum_{k=1}^N \sigma_{R_k}^2} \quad (36)$$

where

$$\mu_{C_k} \stackrel{def}{=} \frac{1}{|C_k|} \sum_{(n,m) \in C_k} I_{alg}(n, m), \quad (37)$$

$$\sigma_{C_k}^2 \stackrel{def}{=} \frac{1}{|C_k|} \sum_{(n,m) \in C_k} (I_{alg}(n, m) - \mu_{C_k})^2, \quad (38)$$

and  $|C_k|$  denotes the number of pixels in class  $C_k$ .

- 6) To avoid sensitivity to resolution, the quantity we will use to measure the improvements to the image  $\mathbf{J}$  due to algorithm  $alg$  is

$$\tilde{Q}_{\mathbf{I}_{alg}} \stackrel{def}{=} \frac{Q_{\mathbf{I}_{alg}}}{Q_{\mathbf{J}}}. \quad (39)$$

We refer to this relative performance metric  $\tilde{Q}_{\mathbf{I}_{alg}}$  as the ultrasound despeckling assessment index (USDSAI).

If the classes are well separated, then the numerator in equation (36) will be large. If the segmentation or restoration algorithm produces small intra-class variances, then the denominator of equation (36) will be small, resulting in the USDSAI quantity  $\tilde{Q}_{\mathbf{I}_{alg}}$  to be large. Large value would indicate that  $alg$  produces the desirable restoration result. If  $\tilde{Q}_{\mathbf{I}_{alg}}$  is greater than one, then the algorithm being tested improved the ultrasound image  $\mathbf{J}$ . Larger  $\tilde{Q}_{\mathbf{I}_{alg}}$  values indicate better performance when comparing various algorithms. If  $\tilde{Q}_{\mathbf{I}_{alg}}$  is less than one, then we consider the algorithm being tested as detrimental to the ultrasound image  $\mathbf{J}$ . If  $\tilde{Q}_{\mathbf{I}_{alg}}$  is equal to one, then it is suspect that any improvements were accomplished.

To elucidate the significance of the USDSAI quantity  $\tilde{Q}_{\mathbf{I}_{alg}}$  defined in equation (39), we examine the three extreme cases. The first case is the simulated image  $\mathbf{J}$  is not constant and the resulting image of some algorithm  $\mathbf{I}_{alg}$  is constant. Clearly,  $Q_{\mathbf{I}_{alg}} = \frac{0}{0}$ , which we define as zero. Thus, the quantity  $\tilde{Q}_{\mathbf{I}_{alg}}$  is

equal to zero. We consider algorithms that yield small  $\tilde{Q}_{\mathbf{I}_{alg}}$  values, less than one, as indicative of poor performance.

In the second case, the simulated image  $\mathbf{J}$  is neither a constant nor a scaled version of the template image. The resulting image of some algorithm is the template image, that is  $\mathbf{I}_{alg} = \mathbf{T}$ . In this case

$$Q_{\mathbf{I}_{alg}} = \frac{K}{0} = \infty \Rightarrow \tilde{Q}_{\mathbf{I}_{alg}} = \infty \quad (40)$$

when the average of the squared differences of the inter-class means represented as  $K$  is not equal to zero. We will consider this quantity as indicative of an ideal improvement to the image  $\mathbf{J}$  and the algorithm being tested performed ideally.

The third and final case is when the simulated image  $\mathbf{J}$  be composed of classes  $C_1, C_2, C_3, \dots, C_N$  and the pixel values of the resulting image  $\mathbf{I}_{alg}$  is some constant except for a single point within each class  $C_1, C_2, C_3, \dots, C_N$ , without loss of generality, say the pixel values are all zero except at differing points in each class have values  $K_1|R_1|, K_2|R_2|, K_3|R_3|, \dots, K_N|R_N|$ , where  $K_i \geq 0$ . In other words, the algorithm being tested sets the pixels in each class to the same constant except one pixel differs from the rest. In this case, the sum of the inter-class mean differences squared is

$$\sum_{k>l} (\mu_{C_k} - \mu_{C_l})^2 = \sum_{k>l} (K_k - K_l)^2 \leq (N-1) \sum_{k=1}^N K_k^2. \quad (41)$$

The inequality of equation (41) is attain from the safe assumption that  $K_k \geq 0$  for all  $k$ . The variance for each class  $C_k$  where  $k = 1, 2, 3, \dots, N$  is

$$\sigma_{C_k}^2 = (|C_k| - 1)K_k^2. \quad (42)$$

The sum of the intra-class variances is

$$\sum_{k=1}^N \sigma_{C_k}^2 = \sum_{k=1}^N (|C_k| - 1)K_k^2. \quad (43)$$

Let  $C_{min} = \min\{|C_k| \text{ where } k = 1, 2, 3, \dots, N\}$ , so that

$$\sum_{k=1}^N \sigma_{C_k}^2 \geq (C_{min} - 1) \sum_{k=1}^N K_k^2. \quad (44)$$

Using the inequalities from equations (41) and (44), the quantity  $Q_{I_{alg}}$  defined in equation (36) is bounded above by

$$Q_{I_{alg}} \leq \frac{(N-1) \sum_{k=1}^N K_k^2}{(N-1)(R_{min}-1) \sum_{k=1}^N K_k^2} = \frac{1}{C_{min}-1}. \quad (45)$$

In this present case, the algorithm being evaluated produces an image composed of a scaled Kronecker delta function in each class. When  $C_{min}$  is very large, the original unprocessed image contain large classes of homogeneous regions and the metric  $Q_{I_{alg}}$  returns a small number. Thusly, the  $\tilde{Q}_{I_{alg}}$  value would be smaller than  $\tilde{Q}_J$ .

To present an objective comparison, we perform an exhaustive search varying the parameters of each algorithm so that the USDSAI value  $\tilde{Q}_{I_{alg}}^{III}$  was maximized. We used these optimal parameters of each algorithm to perform the comparison with the other test images. The result of this exhaustive search for the Wiener filter PSF that was derived from the simulation is a two dimensional Gaussian function with horizontal and vertical means of zero and standard deviations of 0.1.

The resulting images using the Nagao, Lee, Frost, Kuan, AWMF, SRAD, Wiener, and SBF are shown in Fig. 2 and 3. The USDSAI values  $\tilde{Q}_{I_{alg}}^i$  of each filter is given in Table I. The observant readers will notice that the subjective results shown in Fig. 2 and 3 reflect the quantitative results of Table I. The average of all USDSAI values  $\tilde{Q}_{I_{alg}}^i$  for all algorithms tested is given in the rightmost column of Table I.

The resulting images produce by the Nagao filter are shown in Figs. 2(a)- 2(d). A close inspection of these images show that the Nagao filter produces small “patchy” regions in place of the speckle. More detrimental, it is very evident that the edges of the various circular regions are greatly distorted. The USDSAI values  $\tilde{Q}_{I_{Nagao}}^I$  and  $\tilde{Q}_{I_{Nagao}}^{II}$  given in Table I are less than one, indicating that the Nagao filter is counter productive in improving the contrast enhancement of these simulated ultrasound images. An intraclass reduction in the variances of the different classes of the simulated images shown in Fig. 2(c)- 2(d) produced USDSAI values  $\tilde{Q}_{I_{Nagao}}^{III}$  and  $\tilde{Q}_{I_{Nagao}}^{IV}$ , to be greater than one. Thus, a overall modest quantitative improvement due to the Nagao filter is indicated by the average USDSAI value slightly greater than one

and given in the rightmost column of Table I.

The images shown in Figs. 2(e)- 3(d) are due to the application of the Lee, Frost, Kuan filters, and AWMF, *resp.* Compared with the simulated images shown in Fig. 1, the subjective or qualitative improvements due to these filters are at best trivial, if any improvements can even be claimed. The USDSAI values of these four algorithms are given in Table I. The rightmost column of Table I shows the average USDSAI from the four simulated images of each algorithm. A qualitative visual inspection and quantitative assessment using the USDSAI values of the Lee, Frost, Kuan filters and AWMF indicate lackluster results when compared with the image quality and USDSAI values of SRAD, Wiener filtering, and SBF.

A qualitative assessment of the resulting images after applying SRAD is given in Fig. 3(e)- 3(h) and visibly shows that the variances in the different classes are decreased. The decrease in variances in the different classes due to SRAD is indicated by significantly larger USDSAI values shown in Table I. The rightmost column in the SRAD row of Table I gives the average USDSAI value and is noticeably greater than the average USDSAI values attained by the Nagao, Lee, Frost, Kuan filters, and AWMF.

The result of Wiener filtering shown in Fig. 3(i)- 3(l). Except for the results due to SBF, these results are perceptively better than the images produced by the other algorithms. The different classes of each image are well defined and the edges are noticeably more pronounced than in the unprocessed simulated images shown in Fig. 1(e)- 1(h) and the results of the other algorithms. The enhancements provided by Wiener filtering result in an increased USDSAI value, even over SRAD. Unfortunately, it could also equally be argued that a low pass version of the speckle persists and reduction in the intraclass variance could be improved.

The resulting four images produced by the SBF despeckling method using a applied to the four Field II simulated images are shown in Figs. 3(m)- 3(p). It is visually obvious that the edges of the various disks are equivalently as well preserved when compared with the results of the Wiener filter. Equally important the intraclass variance is decreased in each simulated image. These noticeable contrast improvements

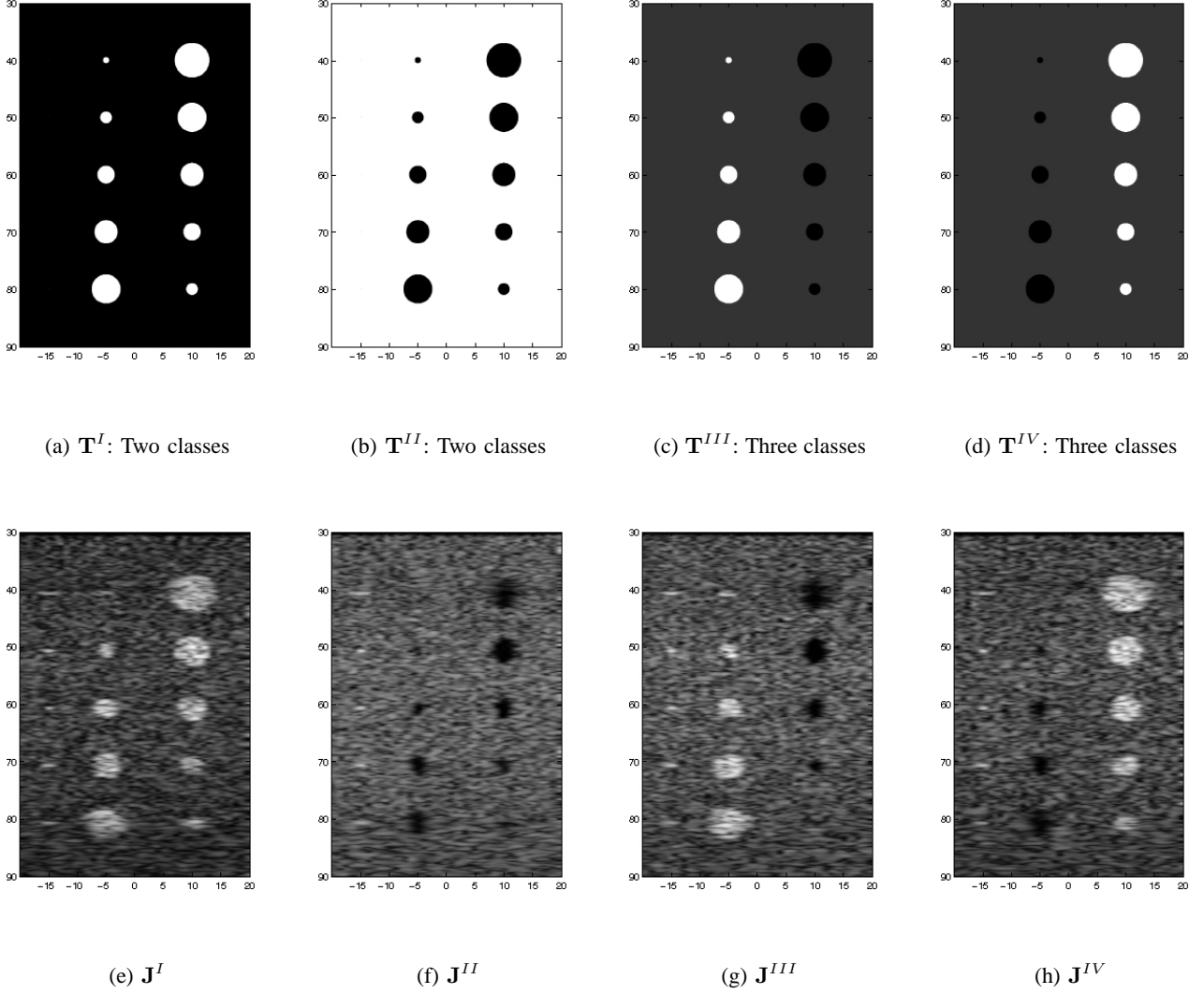


Fig. 1. Two and three class templates and ultrasound simulations used in the comparison.

are reflected by the USDSA values in the last row of Table I. Except for  $\tilde{Q}_{\mathbf{I}_{SBF}^I}$ , which is slightly less than  $\tilde{Q}_{\mathbf{I}_{Wiener}^I}$ , the other quantitative results show improved contrast enhancement over the other algorithms, even over the Wiener filter. The average USDSA values of the SBF method indicate greater contrast improvements over the Wiener filter and significantly greater contrast improvements over the other despeckling algorithms.

### B. Using Actual Phantom Image

The SRAD and SBF despeckling methods that performed well on simulated images were evaluated using an actual ultrasound scan of a phantom. Since the Wiener filter requires prior knowledge of the PSF

		$\tilde{Q}_{I_{alg}^I}$	$\tilde{Q}_{I_{alg}^{II}}$	$\tilde{Q}_{I_{alg}^{III}}$	$\tilde{Q}_{I_{alg}^{IV}}$	Average
F	Nagao	0.9901	0.9730	1.0315	1.3651	1.09
	Lee	1.2014	1.1760	1.2007	1.2097	1.197
	Frost	1.0479	1.0211	1.0446	1.0457	1.04
	Kuan	1.0007	1.0006	1.0012	1.0016	1.001
	AWMF	1.1005	1.0936	1.0959	1.1025	1.098
	SRAD	1.5344	1.4729	1.8603	1.8187	1.6716
	Wiener	2.0884	1.8423	2.0256	2.0072	1.9909
	SBF	1.9974	2.1160	2.1491	2.1144	<b>2.0942</b>

TABLE I

USDSAI VALUES  $\tilde{Q}_{I_{alg}^i}$  FOR THE VARIOUS ALGORITHMS TESTED.

and this paper is not focused on estimating or calibrating the PSF of the ultrasound system, the Wiener filter was not evaluated. Rather, we visually evaluate the performance of SRAD and SBF at various iterations. This evaluation uses an actual B mode image taken from a scan of a real phantom. The original phantom image is shown in the top image of Fig. 4. The phantom consist of three equal size disks with varying brightness. The three images in Figs. 4(b), 4(d), and 4(f) show the results of SRAD at 10, 25, and 50 iterations, *resp.* The images on the right column of Fig. 4 show in Figs. 4(c), 4(e), and 4(g) are the results of the SBF method using an  $11 \times 11$  window at 10, 25, and 50 iterations, *resp.* All the images in Fig. 4 are shown scaled to eight bit dynamic range, that is 256 gray levels. A visual comparison of these images show that at the three iterations the brightness of rightmost disk is greater than the middle disk and the brightness of the middle disk is greater than the the leftmost disk with the results of the SBF method than SRAD. Additionally, the leftmost darkest disk at 50 iterations almost blends into the background, while even at the 50<sup>th</sup> iteration of SBF this disk is well pronounced. It is well worth noting that the bright dots between the leftmost and the middle disks are better preserved with SRAD than SBF. From the result of this evaluation using an actual ultrasound phantom image, we conclude that SBF is

better at preserving the contrast of the three disks at a cost of decimating the fine resolution features such as the bright dots between the leftmost and middle disks.

### C. 3-D GVF Active Contour Surface Rendering

Preserving or enhancing the contrast of large blunt objects at the cost of losing or fading smaller objects is preferred in our ultimate goal of rendering a 3-D surface from 2-D ultrasound slices of an organ such as a heart, prostate, kidney, *etc.* In this evaluation we used an linear array transducer to scan an egg shaped phantom. The 2-D slices are taken at every 1mm along the long axis of the egg phantom. There is a total of 41 slices and the B mode middle slice of the egg phantom is shown in Fig. 5(a). The 3-D rendering using a naive implementation of SRAD processed slices yielded a surface that in no way resemble the egg phantom. So each slice was SRAD processed by meticulously adjusting the parameters and iterations of SRAD so that a well defined high contrast image was produces. After each slice was optimally visually contrast enhanced by SRAD, a post despeckling algorithm of morphologically filling in the holes was applied. The result of the optimized SRAD followed by morphologically filling the holes applied to the image in Fig. 5(a). Albeit labor intensive, the result of these processes are exceptionally excellent. We will used the 3-D GVF active contour rendering of these exceptional SRAD with morphological hole filling slices as ground truth, a gold standard to compare the results of processing with SBF. We applied the same 75 iteration SBF process using a  $11 \times 11$  window to each of the 41 slices. This processing was implemented using Mathworks Matlab 7.0.0.19920 on a Intel P4 3.8 GHZ CPU. The processing time need by the SBF to process all 41 slices was 8.8268 minutes. The result of SBF applied to the middle slice is shown in Fig. 5(c).

The 3-D rendering of the final contour using the same number of iteration of the 3-D GVF snake produced from the 41 slices processed by the human optimized SRAD-morphological hole filling operation and SBF are shown in Figs. 6(a) and 6(b), *resp.* The 3-D renderings are displayed so that the worst part of each 3-D surface is shown. In the 3-D rendering provided by the human optimized SRAD with morphological hole filling, there is an erroneous indentation just above the horizontal bisecting plane. The



3-D rendering using the SBF processed slices exhibits two unwanted steps above the horizontal bisecting plane. Both 3-D GVF active contour rendering using the human optimized SRAD with morphological holes filled and SBF processed perform well in that overall shape of the egg is captured. Estimation of the volume enclosed by each the surface created from the human optimized SRAD with morphological hole filling errs by approximately 7% of the true volume. Volume estimate enclosed by the 3-D GVF surface using SBF processed slices yields a 10% error to the true volume. The slightly high error using the 3-D rendering from the SBF processed slices is insignificant when one considers the effortlessness of attaining SBF processed slices over optimizing each slice with SRAD and subsequently applying a morphological hole filling operation.

## V. CONCLUSION

The removal or reduction of speckle noise while preserving or enhancing edge information of an ultrasound image is an extremely difficult task. Since the GVF is derived from an edge map, robustly despeckling each slice is vital prior to apply the 3-D GVF snake to determine a surface from ultrasound slices. We consider of a wide variety of filtering algorithms for this pre-rendering step. The despeckling methods describe in this paper and in general scrutinize every pixel values. We present a novel iterative despeckling method SBF that at each iteration only scrutinize the value, which are considered outliers. Without using the outlying values to determine the local, the SBF method replaces these outliers by values that approach the mean of the local homogeneous region. Each iteration of this new method compress the image pixel values so that the differences in interclass means are preserved or possibly enhanced while the intraclass variance is decreased. The superior contrast enhancement performance of the SBF method is established by our experimentation using Field II simulated ultrasound images and evaluated with USDSAI performance metric defined in equation (39). Our next experimentation evaluation compare the anisotropic diffusion method SRAD with SBF on an actual ultrasound image of a phantom consisting of three disks of the same size but varying brightness. The SBF exhibited excellent contrast improvements of the three disks over SRAD, but at the cost of fading the small bright spots. This tradeoff is preferred

in our ultimate goal of applying a 3-D GVF snake to render an accurate surface. Our last experiment shows that the surface found by the 3-D GVF snake using the SBF processed slices is comparable in size, shape, and volume of the surface rendered by applying the 3-D GVF snake to the tediously human optimized SRAD and morphologically hole filled slices.

## ACKNOWLEDGMENT

The authors would like to thank University of Virginia (UVA) graduate student Bing Li for implementing the 3-D GVF snake and the other members of Virginia Image and Video Analysis (VIVA) group at the UVA for meticulously optimizing SRAD and methodically applying the morphological hole filling operation.

## REFERENCES

- [1] C. Xu and J. L. Prince, "Snakes, shapes, and gradient vector flow," *IEEE Trans. Image Processing*, vol. 7, no. 3, pp. 359–369, March 1998.
- [2] J. W. Goodman, "Statistical properties of laser speckle patterns," in *Laser Speckle and Related Phenomena*, J. C. Dainty, Ed. Berlin: Springer-Verlag, 1984, pp. 9–75.
- [3] J. G. Abbott and F. L. Thurstone, "Acoustic speckle: theory and experimental analysis," *Ultrasonic Imaging*, vol. 1, pp. 303–324, 1979.
- [4] R. F. Wagner, S. W. Smith, J. M. Sandrik, and H. Lopez, "Statistics of speckle in ultrasound B-scans," *IEEE Trans. Sonics Ultrason.*, vol. 30, no. 3, pp. 156–163, May 1983.
- [5] R. F. Wagner, M. F. Insana, and S. W. Smith, "Fundamental correlation lengths of coherent speckle in medical ultrasonic images," *IEEE Trans. Ultrasonics, Ferro., and Freq. Control*, vol. 35, no. 1, pp. 34–44, Jan. 1988.
- [6] M. Nagao and T. Matsuyama, "Edge preserving smoothing," *Computer Graphics and Image Processing*, vol. 9, no. 4, pp. 394–407, April 1979.
- [7] J. S. Lee, "Digital image enhancement and noise filtering by use of local statistics," *IEEE Trans. Pattern Anal. Machine Intell.*, vol. PAMI-2, no. 2, pp. 165–168, March 1980.
- [8] V. S. Frost, J. A. Stiles, K. S. Shanmugan, and J. C. Holtzman, "A model for radar images and its application to adaptive digital filtering of multiplicative noise," *IEEE Trans. Pattern Anal. Machine Intell.*, vol. PAMI-4, no. 2, pp. 157–166, March 1982.
- [9] D. T. Kuan, A. A. Sawchuk, T. C. Strand, and P. Chavel, "Adaptive noise smoothing filter for images with signal-dependent noise," *IEEE Trans. Pattern Anal. Machine Intell.*, vol. PAMI-7, no. 2, pp. 165–177, March 1985.
- [10] —, "Adaptive restoration of images with speckle," *IEEE Trans. Acoust., Speech, Signal Processing*, vol. ASSP-35, no. 3, pp. 373–383, March 1987.

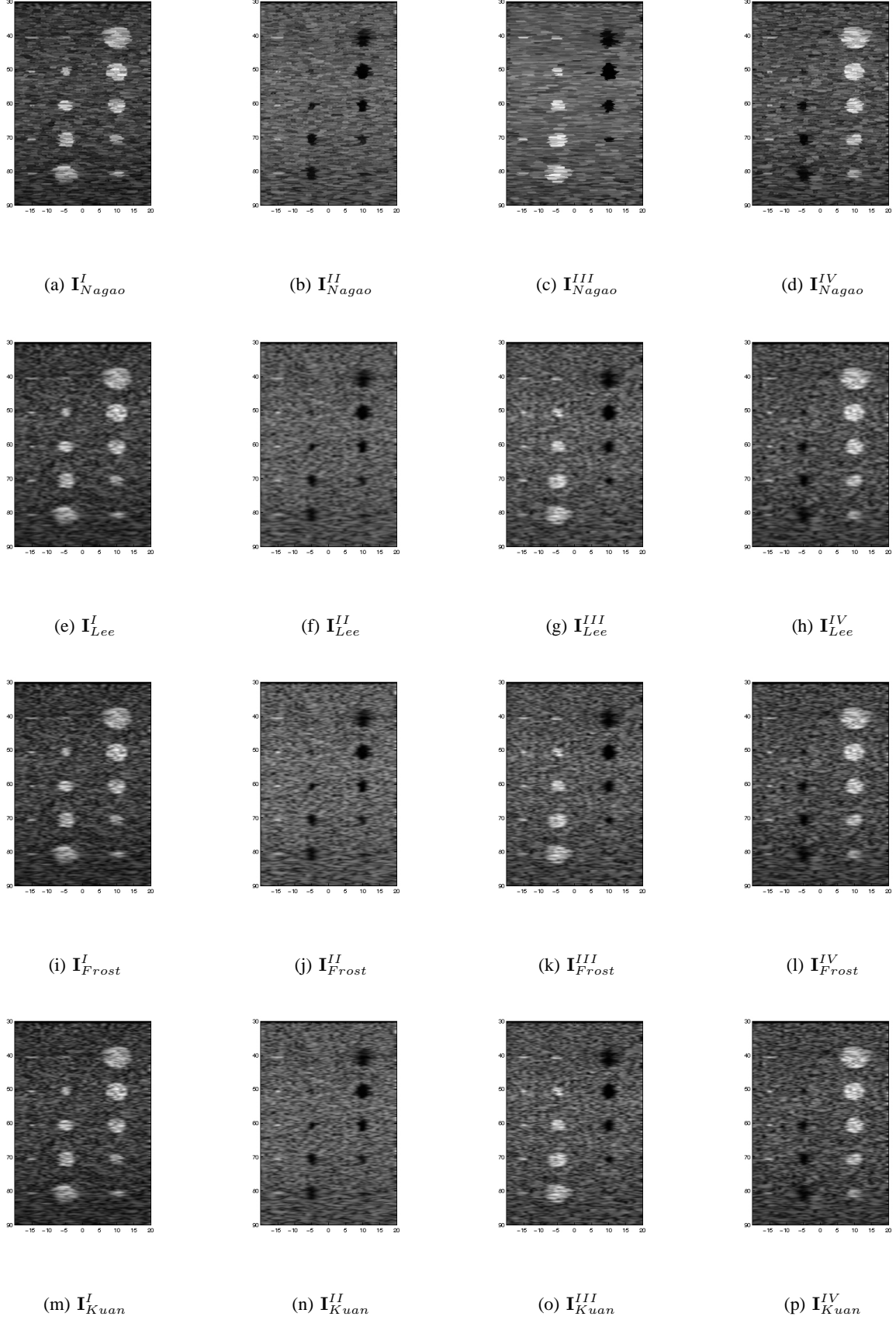


Fig. 2. The resulting images from various adaptive filtering algorithms.

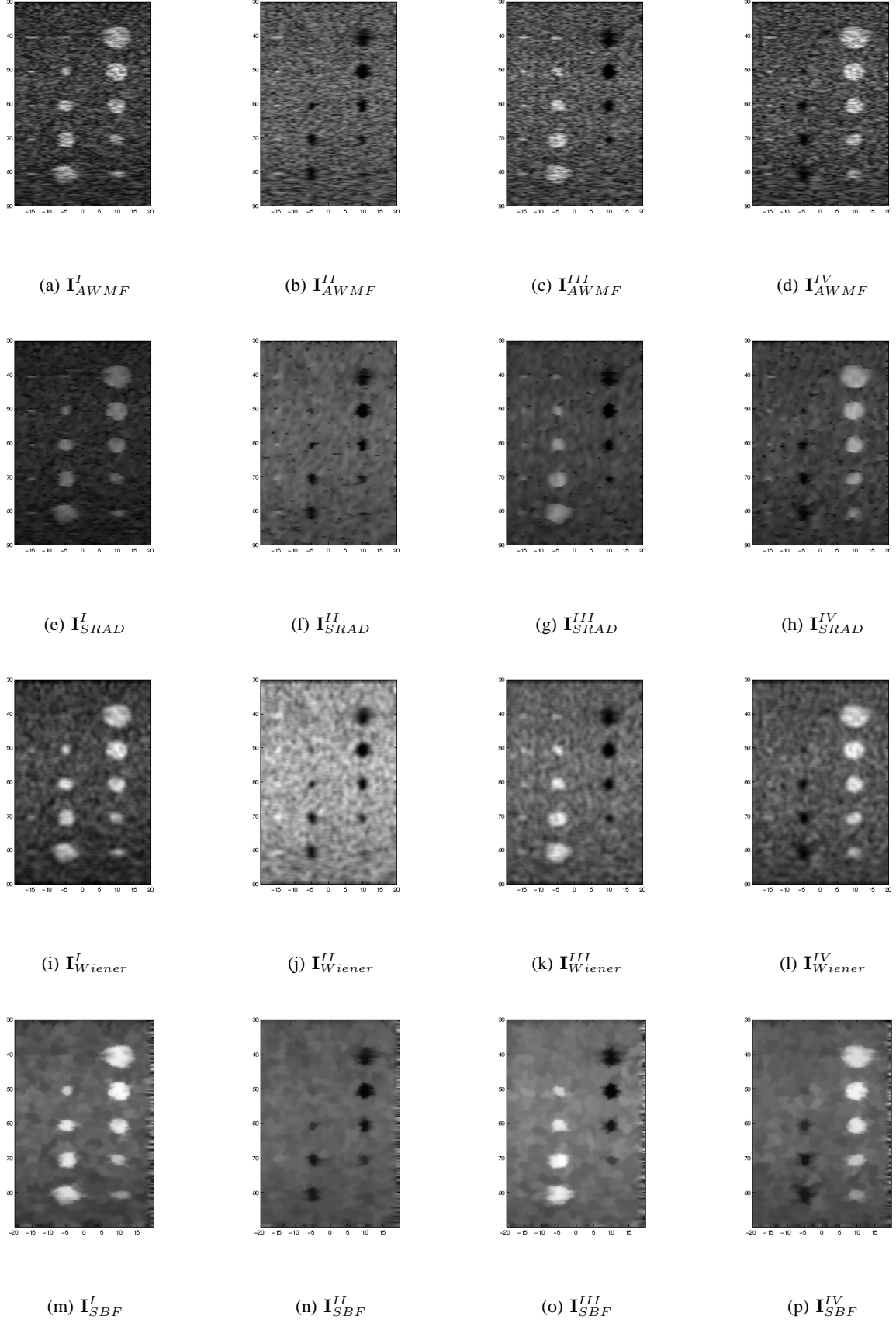
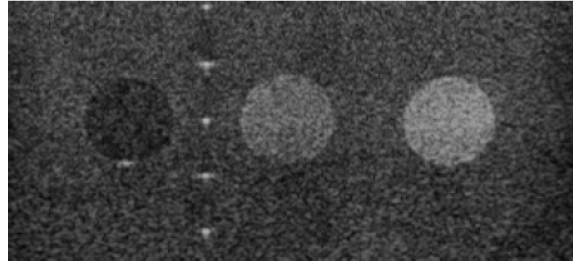
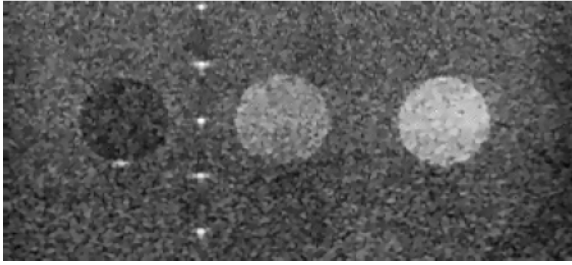


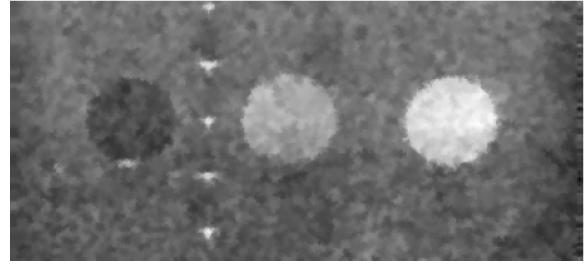
Fig. 3. The resulting images from AWMF, SRAD, Wiener, and SBF filters.



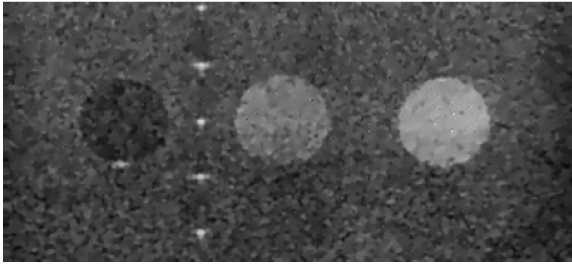
(a) Original phantom image.



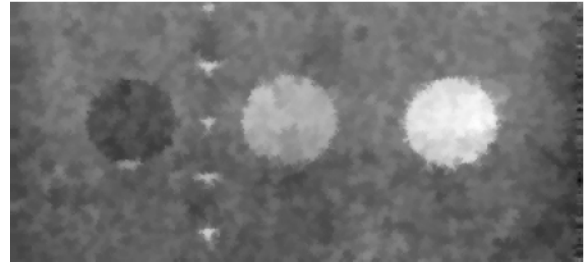
(b) 10 iterations of SRAD.



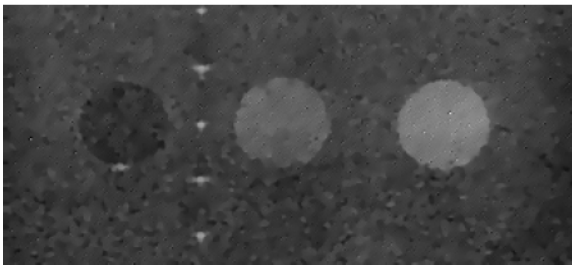
(c) 10 iteration of SBF.



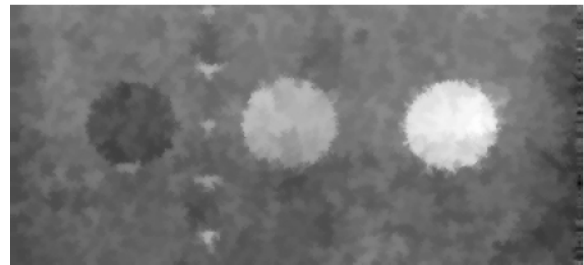
(d) 25 iterations of SRAD.



(e) 25 iteration of SBF.

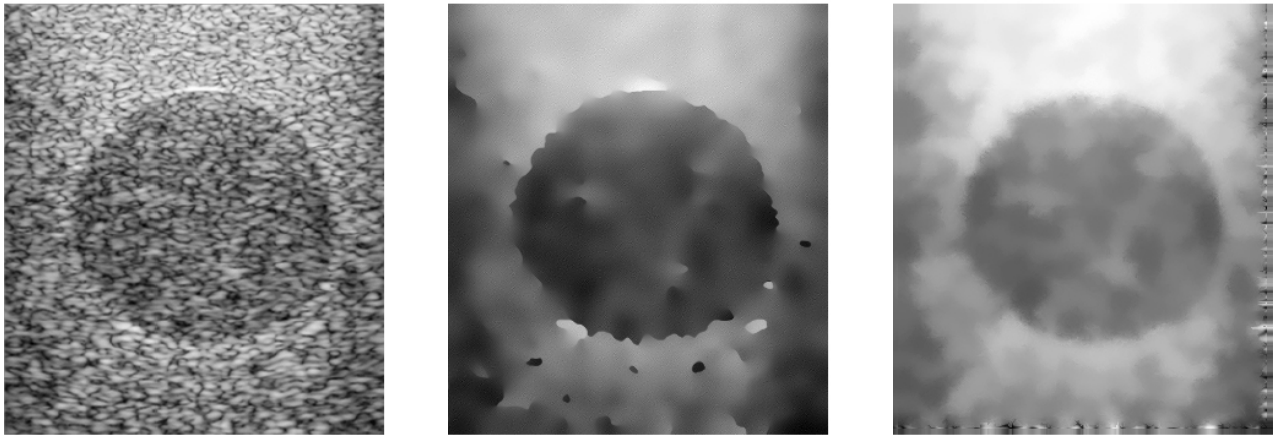


(f) 50 iterations of SRAD.



(g) 50 iteration of SBF.

Fig. 4. The resulting images from 10, 25, 50 iterations of SRAD and SBF.



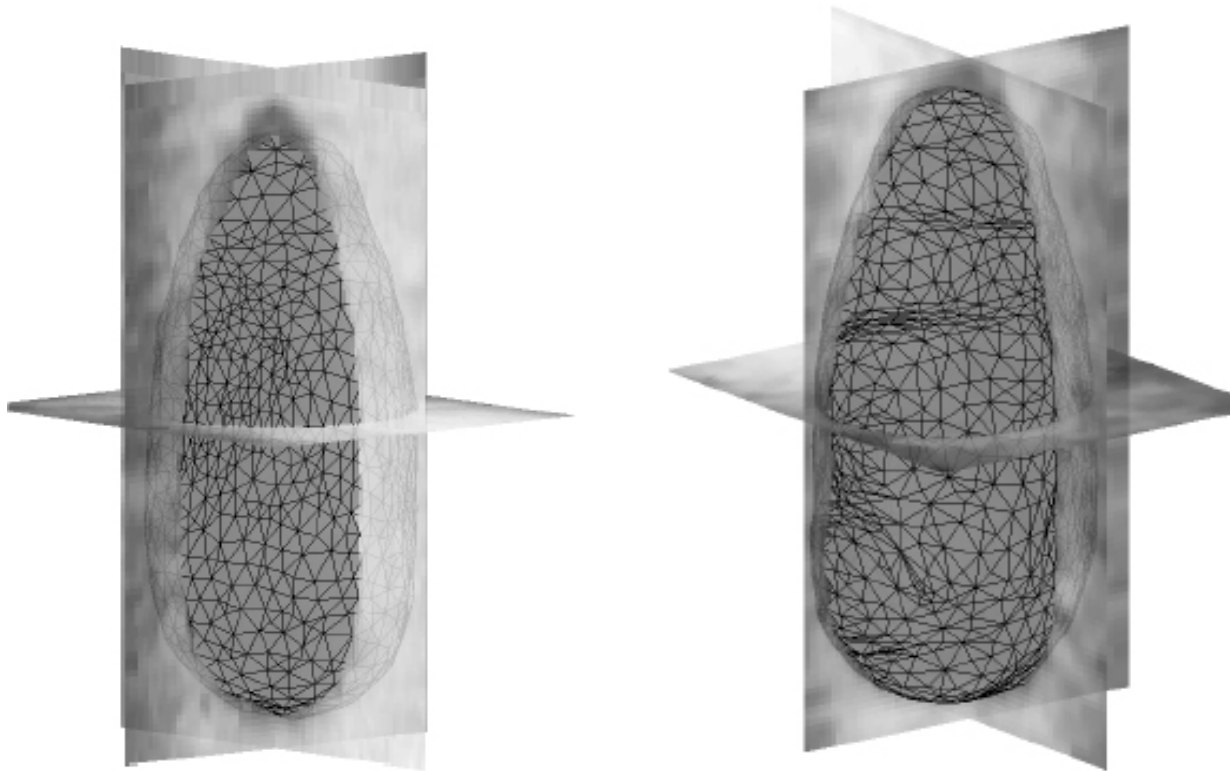
(a) The middle slice of a 3-D egg phantom.

(b) The visually optimized SRAD followed by a morphological hole filling processed middle slice.

(c) The SBF processed middle slice.

Fig. 5. The original middle slice, the processed slice using SRAD (optimized by human interactions) and a morphological hole filling operation, and SBF using an  $11 \times 11$  window.

- [11] T. Loupas, W. N. McDicken, and P. L. Allan, "An adaptive weighted median filter for speckle suppression in medical ultrasonic images," *IEEE Trans. Circuits Syst.*, vol. 36, no. 1, pp. 129–135, January 1989.
- [12] M. Karaman, M. A. Kutay, and G. Bozdagi, "An adaptive speckle suppression filter for medical ultrasonic imaging," *IEEE Trans. Med. Imag.*, vol. 14, no. 2, pp. 283–292, June 1995.
- [13] P. Perona and J. Malik, "Scale-space and edge detection using anisotropic diffusion," *IEEE Trans. Pattern Anal. Machine Intell.*, vol. 12, no. 7, pp. 629–639, July 1990.
- [14] Y. Yu and S. T. Acton, "Speckle reducing anisotropic diffusion," *IEEE Trans. Image Processing*, vol. 11, no. 11, pp. 1260–1270, November 2002.
- [15] S. G. X. Hao and X. Gao, "A novel multiscale nonlinear thresholding method for ultrasonic speckle suppressing," *IEEE Trans. Med. Imag.*, vol. 18, no. 9, pp. 797–794, Sept. 1999.
- [16] A. Achim, A. Bezerianos, and P. Tsakalides, "Novel Bayesian multiscale method for speckle removal in medical ultrasound images," *IEEE Trans. Med. Imag.*, vol. 20, no. 8, pp. 772–783, Aug. 2001.
- [17] A. Lopes, R. Touzi, and E. Nezry, "Adaptive speckle filters and scene heterogeneity," *IEEE Trans. Geosci. Remote Sensing*, vol. 28, no. 6, pp. 992–1000, Nov. 1990.
- [18] T. Kailath, "Equations of Wiener-Hopf type in filtering theory and related applications," in *Norbert Wiener: Collected Works vol. III*, P. Masani, Ed. Cambridge, MA: MIT Press, 1976, pp. 63–94.
- [19] P. Charbonnier, L. Blanc-Féraud, G. Aubert, and M. Barlaud, "Deterministic edge-preserving regularization in computed imaging,"



(a) 3-D surface rendering of an egg using a human optimized SRAD followed a morphological hole filling operation.

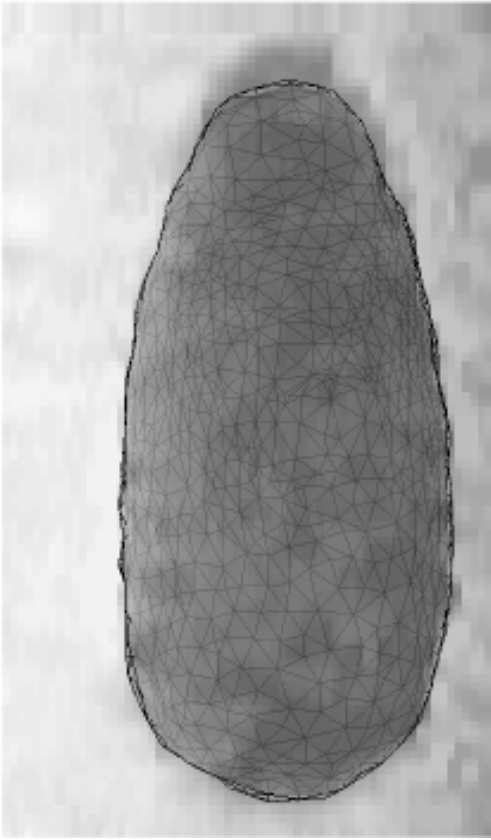
(b) 3-D surface rendering of an egg using SBF.

Fig. 6. The 3-D surface renderings of the egg phantom where each slice is processed with the visually optimized SRAD followed by a morphological hole filling operation and the SBF using an  $11 \times 11$  window.

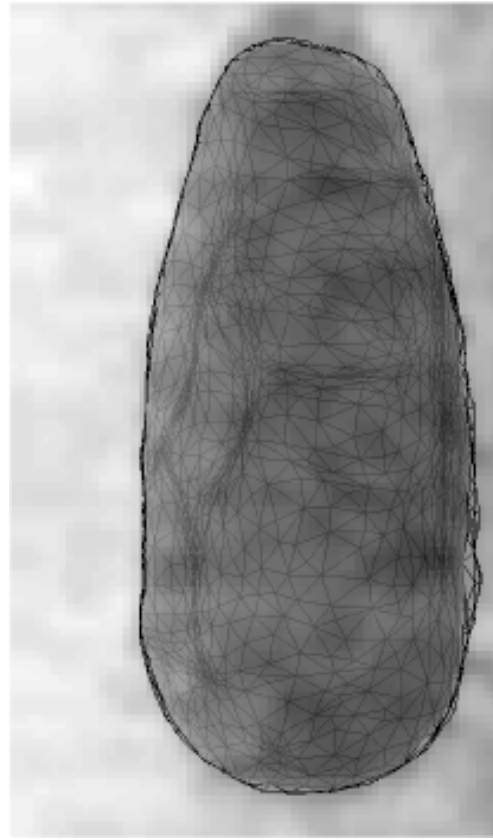
*IEEE Trans. Image Processing*, vol. 6, no. 2, pp. 298–311, Feb. 1997.

[20] S. Teboul, L. Blanc-Féraud, G. Aubert, and M. Barlaud, “Variational approach for edge-preserving regularization using coupled PDE’s,” *IEEE Trans. Image Processing*, vol. 7, no. 3, pp. 387–397, March 1998.

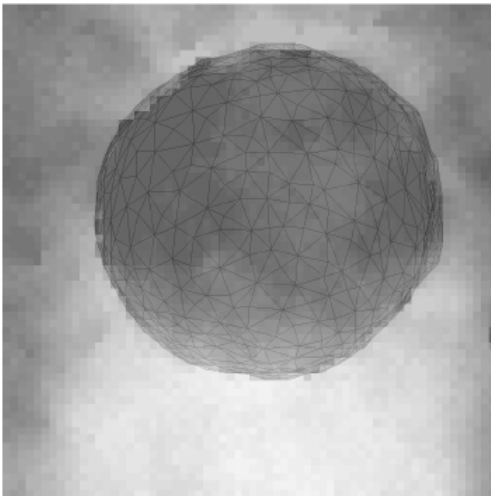
[21] J. A. Jensen and N. B. Svendsen, “Calculation of pressure fields from arbitrarily shaped apodized and excited ultrasound transducers,” *IEEE Trans. Ultrasonics, Ferro., and Freq. Control*, vol. 39, no. 2, pp. 262–267, Feb. 1992.



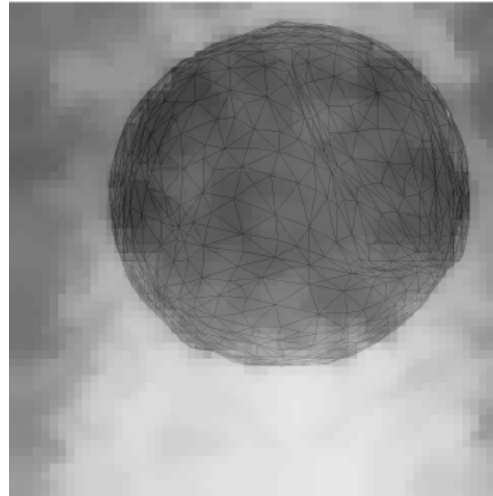
(a) The side view of egg using SRAD.



(b) The side view of egg using SBF.



(c) The top view of egg using SRAD.



(d) The top view of egg using SBF.

Fig. 7. Side and top views of the 3-D rendering of the egg phantom using the human optimized SRAD followed by a morphological hole filling operation and the surface rendering using SBF.



# A Stochastic Approach to the Noise Restoration Problems

Peter C. Tay, *Member, IEEE*, Scott T. Acton, *Senior Member, IEEE*,  
and John A. Hossack, *Senior Member, IEEE*

## Abstract

This paper proposes a robust method to restore piecewise constant signals contaminated by additive and/or multiplicative noise. Additionally, the signal maybe distorted by the underlying physics of the signal acquisition system. The possible distortion caused by an signal acquisition system is modeled as a convolution with some impulse response. Analytic analysis will establish that when the signal is view as a stochastic process and regardless of whether the noise is additive or multiplicative, exact or perfect restoration is pausable. The implementation of these well known and firmly established analytic facts about random processes will utilize a stochastically driven filter that we appropriately call the squeeze box filter. We will empirically show that the squeeze box filter can provide a faithful and accurate solution to the additive and multiplicative noise restoration problems under the regularization constraint that the ideal or desired signal is piecewise constant and provided that the expected value, *i.e.* mean or average, of the stationary noise is known *a priori*. Even if the expected value of the noise is not known, the proposed filtering method produces a robust method to decrease variances within intervals where the signal is a constant value, while the opposing task of preserving edges is maintained.

P. C. Tay and S. T. Acton are with the Dept. of Electrical and Computer Engineering and the Dept. of Biomedical Engineering, University of Virginia, Charlottesville, VA 22904 USA (email: ptay@virginia.edu; acton@virginia.edu). J. A. Hossack is with the Dept. of Biomedical Engineering, University of Virginia, Charlottesville, VA 22904 USA (email: hossack@virginia.edu).

# A Stochastic Approach to the Noise Restoration Problems

## I. INTRODUCTION

The physical nature of ultrasonic sound wave as an imaging modality allows a safe (uses non-ionizing energy), noninvasive, and relatively inexpensive medical diagnostic imaging tool. Though these justifications for using ultrasound images as a medical diagnostic tool are appealing, the images provided by an ultrasonic imaging system is relatively unfavorable when compared to systems that use X-rays (*e.g.* film-screen or digital radiography, fluoroscopy, computed tomography) and nuclear magnetic resonance. The basic physics of ultrasound imaging and other medical imaging modalities are well described in [1].

As with all known nonbiological imaging systems, the images produced by an ultrasonic imaging system are degraded by some form of noise. The noise inherent to ultrasound imaging is dependant on several factors such as axial/lateral resolutions of the transmit/receive frequencies, axial and lateral distances from the transducer, the image resolution, the characteristics of the tissue(s), organ(s), or object(s) being scanned, electronic noise, scalar quantization of the reflectivity values, *etc.* Though the appearance of the noise can vary, the inherent noise can corrupt the ultrasound system by rendering an image with a grainy texture, that is the image appear contaminated with “salt and pepper” like texture. This type of noise is commonly called speckle by the ultrasound and synthetic aperture radar communities. To show how speckle appears in a typical medical ultrasound image, we offer Fig. 1(a), which displays a B-mode logarithmically compressed envelop detected ultrasound image of a phantom. The phantom

consist of three disks each with different intensity values and are approximately 50 pixels in diameter. The centers of each disk are approximately on row 225. The phantom also contains several point scatters with large intensities along row 90 and along column 120. The noise is evident in this image where the graininess is prominent throughout the entire image and the salt and pepper texture could appear coarser in the far field<sup>1</sup> (not evident in this image). Also evident in Fig. 1(a) are the shadow artifacts that occur away from the transducer immediately below each high intensity point scatters and appear like darkened comet tails. Though not as visually evident, a shadow artifact is present below the center disk. This shadowing phenomena is a known problem with ultrasound imaging and results in smaller intensity values on average within the shadow regions to erroneously occur. The shadowing problem is beyond the scope this paper and we will address this in our future research.

In Fig. 1(b) we show the intensity profile of row 225 of Fig. 1(a). This row approximately bisects all three disks through the center. From the profile in Fig. 1(b) it is difficult to determine which intervals corresponds to the various three disks. Even more difficult is to determine exactly the actual reflectivity values<sup>2</sup> of each phantom disk, since the processing used to produce a visually appealing image skews these values. In Fig. 1(c) is a plot of a possible noise free signal of the intensity profile signal shown in Fig. 1(b). This piecewise constant signal was determine by taking the average in intervals that are known to be a constant. It can be observed from the proposed noise free signal shown in Fig. 1(c) that the intensity value in interval  $[50, 100]$  corresponds to the left most black (low intensity value) disk, the intensity value in interval  $[140, 190]$  corresponds to the middle disk, and the intensity value in interval  $[240, 290]$

<sup>1</sup>The region away from the transducer and pass the focal point.

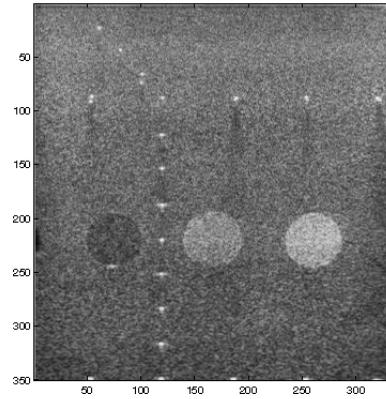
<sup>2</sup>The actual reflectivity value directly relates to tissue/organ elasticity, compressibility, and/or density.

corresponds to the right most brightest (high intensity value) disk of Fig. 1(a).

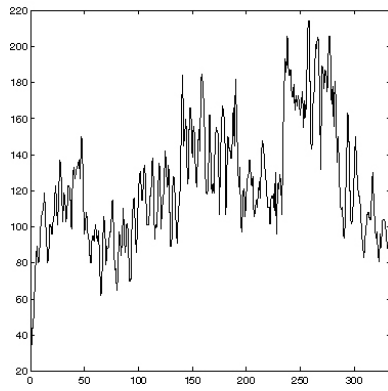
In Fig. 1(d), we show the intensity profile of column 165, which approximately vertically bisects the middle disk of Fig. 1(a). Fig. 1(e) is a plot of a piecewise constant signal determined by taking the average with intervals that are known to be constant. The lower intensity value in the right most interval of the plot in Fig. 1(e) is a shadowing artifact. Ideally, the average intensity value in this interval should be the same as the average intensity value in the left most constant interval of Fig. 1(e).

In creating the noise free piecewise constant signal in Figs 1(c) and 1(e), we used our knowledge of the phantom to determine the values and location of each constant intervals, that is we knew where the edges are located. This in all practical and clinical use of medical ultrasound imaging as a diagnostic tool is not the case. Determining a possible noise free signal such as the ones shown in Figs 1(c) and 1(e) from the noisy signals shown in Figs 1(b) and 1(d) is a classical signal restoration problem.

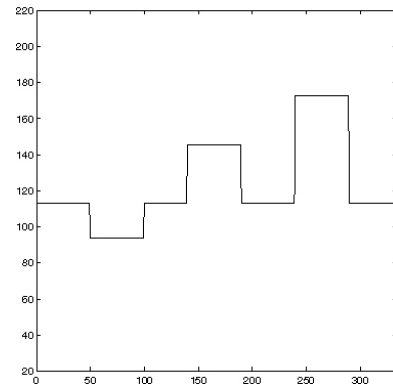
The restoration problem of determining the ideal signal from a distorted and noisy signal is considered ill posed in which the solutions are nonunique and/or it maybe difficult to verify the significance of the proposed solution. To consider the problem well posed, either *a priori* knowledge of the desired signal is needed or constraints on the ideal signals are required. The latter is called *regularization*. Some regularization constraints for signals are proposed in [2], [3]. Some examples of two dimensional regularization constraints for images are proposed in [4]–[7]. To avoid being clouded by dimensionality, the explanations and examples given in this paper are strictly using one-dimensional signals. This allows us to present our ideas on signal restoration in a clear concise manner without being bothered by the technicalities of extending one-dimensional algorithms to multiple dimensions. Since the composition of ultrasound images



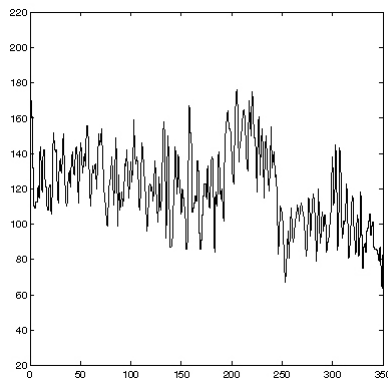
(a) Ultrasound Phantom Image



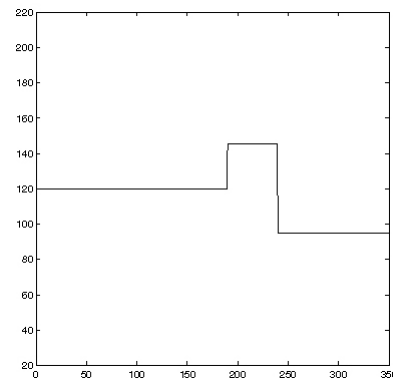
(b) Intensity profile of row 225



(c) Row 225 noise free signal



(d) Intensity profile of column 165



(e) Column 165 noise free signal

Fig. 1. Ultrasound phantom image, the intensity profiles, and possible noise free signals.

is an synchronous arrangement of one dimensional signals, the analysis and processing of one dimensional signal in this paper is relevant to enhancing and improving ultrasonic imaging.

The mathematical modeling of ultrasound data is debateable. The evidence provided by Wagner *et. al.* in [8], [9] suggest that ultrasound speckle is multiplicative and Rayleigh distributed. While Loupas *et. al.* in [10] and Karaman *et. al.* in [11] claim speckle is composed of a combination of multiplicative and additive components<sup>3</sup>. The determination of the best method to model ultrasound data is beyond the scope of this paper. Instead this paper will focus on the usual additive and multiplicative signal restoration problems.

The two usual restoration problems [12] are to determine the ideal signal  $f(n)$  from the detected signal  $g(n)$  given by the additive model

$$g(n) = p(n) * f(n) + \eta(n) \quad (1)$$

or by the multiplicative model

$$g(n) = p(n) * \{f(n)\eta(n)\} \quad (2)$$

where  $p(n)$  denotes the impulse response of some system, the asterick symbol represents linear convolution, and  $\eta(n)$  is a random variable with some probability density function (PDF). The noise samples  $\eta(n)$  are generally assumed to be white and Gaussian distributed. Moreover, the noise is typically assumed to be independent of  $f(n)$ . Generally, there is an unmentioned assumption that the noise is a wide sense stationary process and we will accept this underlying assumption throughout this paper. In the models given in equations (1) and (2), the distorted signal is modeled as a convolution by an impulse response,  $p(n)$ . This distortion is usually a

<sup>3</sup>They do not mention the noise distribution.

blurring or smoothing of the desired signal. Thus the impulse response is in nature a low pass filter.

The additive restoration problem given in equation (1) has extensively been studied and many solutions to this problem have been employed with varying success. These solutions include linear filtering such as a moving average, non-linear filters such as the various adaptive median and mean filters [4], [23], Weiner filtering [13], wavelet thresholding [12], *etc.*

Methods to solve the multiplicative restoration problem of equation (2) are and have been of great interest to ultrasound and SAR image processing societies. Solutions to the two dimensional extension of the multiplicative noise model have been proposed in [7], [10], [11], [14]–[22]. None of the proposed method especially for multiplicative noise restoration claim an exact restoration of the ideal signal and may only offer subjective improvements. Provided the usual assumptions, the noise is stationary and is a zero mean Gaussian distributed random process, are accepted, exact reconstruction of the ideal signal will be shown to be analytically possible from both the additive model given in equation (1) or the multiplicative model given in equation (2). Though exact reconstruction is possible in an analytic sense, the practical implementation of these analytic concepts is not without trade-offs. Namely, the task of determining the characteristics of a random process, *e.g.* mean and variance, from only a few recorded samples is debateable. Nevertheless, we will reasonably compromise when required and develop a practical implementation of the analytic concepts presented in this paper. Our examples will empirically show using the assumptions that the noise is white, normally distributed, and stationary that the stochastically driven proposed filter robustly extracts the ideal piecewise constant signal.

## II. VARIOUS SIGNAL RESTORATION METHODS

In this section we will describe a variety of signal restoration methods. The performance of our proposed method will be compared with the performance of the filters described in this section. The quantitative and qualitative assessment of this comparison will be given in section V.

### A. Order Statistic Filters

In [23] Bovik *et. al.* described a family of order statistic filters (OSF). The OSF replaces each and every sample of the noisy signal with the weighted sum of ordered values taken from an odd length window. More precisely, given a window of odd length  $N$ , the value of the current sample is set to

$$g_{OSF}(n) = \sum_{i=n-M}^{n+M} \alpha_i \tilde{g}(i) \quad (3)$$

where  $M = \lfloor \frac{N}{2} \rfloor$ ,  $\lfloor \cdot \rfloor$  is the greatest integer function,  $\tilde{g}(i) \in \{g(i) \mid n - M \leq i \leq n + M\}$ , and  $\tilde{g}(i)$  are ordered so that  $\tilde{g}(i) \leq \tilde{g}(i + 1)$  for all  $i \in [n - M, n + M - 1]$ . These weights  $\alpha_i$  are computed so that the expected value of the filtered signal is optimal in the mean squared error sense. The optimality of the OSF is under the constraint that the signal is constant and the weights of the filter are dependant on the additive noise distribution. For example, if  $\alpha_i = \frac{1}{N}$  for all  $i \in [n - M, n + M]$ , then the filter described in equation (3) is the moving average filter<sup>4</sup>. Bovik *et. al.* analytically show the moving average is optimal, that is the expected value of the mean squared error is minimized, when the ideal signal is constrained as an constant signal and the noise is zero mean and normally distributed. If  $\alpha_n = 1$  and  $\alpha_i = 0$  for all  $i \neq n$ , then the filter in equation 3 is the median filter. The justifications in [23] does not claim that the median

<sup>4</sup>The moving average filter is technically not a OSF, since ordering of the windowed values are not required. We place this example in this section purely for the purpose of efficiency.



is optimal with any of the considered noise distribution. We will include the median filter in our comparison in section V so that a wide range of OSF filters are represented in the experimental comparison. The last OSF we will include in our comparative study has a window length of nine and the following symmetric weight values:

$$\begin{aligned}
 \alpha_n &= 0.36469 \\
 \alpha_{n-1} &= 0.23795 = \alpha_{n+1} \\
 \alpha_{n-2} &= 0.06965 = \alpha_{n+2} \\
 \alpha_{n-3} &= 0.02904 = \alpha_{n+3} \\
 \alpha_{n-4} &= -0.01899 = \alpha_{n+4}.
 \end{aligned} \tag{4}$$

In [23] Bovik *et. al.* claims the OSF with the weights given in equation 4 is optimal in minimizing the expected value of the mean squared error for a Laplacian noise distribution and provided that the ideal signal is a constant.

### B. Wiener Filter

The Wiener filter [13] is a frequency domain solution to the additive noise problem in equation 1. Let  $g(n) \longleftrightarrow G(e^{j\omega})$  be discrete time Fourier transform (DTFT) be pairs, then the Wiener filter is implemented in the Fourier domain as

$$g_{wnr}(n) \longleftrightarrow G_{wnr}(e^{j\omega}) = G(e^{j\omega}) W(e^{j\omega}) \tag{5}$$

where

$$W(e^{j\omega}) = \frac{P^*(e^{j\omega})}{|P(e^{j\omega})|^2 + \sigma_\eta^2} \tag{6}$$

and  $\sigma_\eta^2$  is the variance of the additive noise component. It is important to note that the performance of the Wiener filter is dependant on *a priori* knowledge or an approximation of the transfer function of  $p(n)$  and the noise variance  $\sigma_\eta^2$ .

### C. Wavelet Thresholding

It has been shown in [24] and [25] that applying a threshold operator to the discrete wavelet transform (DWT) coefficients is a useful method to remove or reduce additive white noise. The DWT of a signal described by Mallat in [26] decomposes the signal into various subbands. Assuming that the noise power is below some threshold, then applying a hard [25] or a soft thresholding [24] operation to the DWT coefficients reduces the noise power. In effect the inverse DWT (IDWT) reconstruction of the threshold coefficients produces an approximate noise free signal.

Let  $w(n) = DWT\{g(n)\}$  be the DWT of  $g(n)$ . For  $T \geq 0$  the hard thresholding operation is defined as

$$w_{hard}(n) = \begin{cases} w(n) & \text{if } |w(n)| > T \\ 0 & \text{otherwise.} \end{cases} \quad (7)$$

The soft thresholding operation is defined as

$$w_{soft}(n) = \begin{cases} w(n) - T & \text{if } |w(n)| > T \text{ and } w(n) > 0 \\ w(n) + T & \text{if } |w(n)| > T \text{ and } w(n) < 0 \\ w(n) & \text{otherwise.} \end{cases} \quad (8)$$

An approximation of the additive noise free ideal signal is taken to be the IDWT of  $w_{hard}(n)$  or  $w_{soft}(n)$ . The robustness of the thresholding operations are dependant on the choice of  $T$  and a optimal choice [24], [25] is  $T = \sigma_\eta \sqrt{2 \log N}$  where  $\sigma_\eta$  is the noise standard deviation and  $N$  is the length of  $g(n)$ .

## III. A STOCHASTICALLY DRIVEN FILTER

Even without any *a priori* knowledge of the noise characteristics besides stationarity, the proposed stochastically driven filter will provide a meaningful restoration of a piecewise constant

signal. We use the term “*meaningful*” in the sense that the proposed restoration method will produce a constant value in intervals where the ideal signal is a constant value. Equally as important, the opposing task of preserving step up and step down edges will be maintained.

For a random variable  $X$  it is well known and can be shown that even without prior knowledge of the stationary noise distribution that

$$E\{cX + b\} = cE\{X\} + b \quad (9)$$

where  $b, c$  are constants,  $E\{X\} = \int_{-\infty}^{\infty} x \Pr_X(x) dx$ , and  $\Pr_X(x)$  is the probability density function (PDF) of the random variable  $X$ . Importantly, determining the expected value or mean of a random value will preserves edges, that is for constants  $c_1 \neq c_2$ ,  $X_1$  and  $X_2$  are independent and identically distributed random variables, it can be deduced that

$$E\{c_1 x_1 - c_2 x_2\} = (c_1 - c_2)E\{X\} \neq 0$$

provided that  $E\{X\} \neq 0$ .

From the well know fact given in equation (9) and without loss of generality let  $b = 0$ , a simple algebraic malipulation yields

$$c = \frac{E\{cX\}}{E\{X\}}. \quad (10)$$

Provided that the expected value of the random variable  $X$  is not equal to zero, the triviality of equation (10) yields the *a priori* unknown value  $c$  provided that  $E\{cX\}$  and  $E\{X\}$  are known or can be determined. In the context of the multiplicative noise restoration problem modeled in equation (2) and ignoring the impulse response<sup>5</sup>  $p(n)$  for now, we arrive at the  $n^{th}$  sample of the ideal signal from

$$f(n) = \frac{E\{g(n)\}}{E\{\eta(n)\}} \quad (11)$$

<sup>5</sup>Restrict the impulse response to be the delta function. We will counter effect the impulse response later in this paper.

where  $g(n)$  and  $\eta(n)$  are cast as random variables. If the expected value of the noise term  $\eta(n)$  is known and not equal to zero, then to achieve exact restoration it is only required to determine the expected value of the detected or acquired signal  $g(n)$ .

To determine the expected value of  $g(n)$ , we view the local extrema, that is the local peaks and valleys, to be outliers of some PDF. In opposition to the methods in section II, where every sample is scrutinized, the filtering method presented in this section only scrutinizes the samples that are considered outliers. These outliers are replaced with a value that occurs with greater probability. To ensure that the outliers are replaced with a value with a greater probability, we replace them with the mean determined from some local neighborhood  $\mathcal{N}$ . It is important to keep in mind that the local extrema are considered outliers and should not be used in the determination of the local mean. The choice of the neighborhood  $\mathcal{N}$  is extremely important, since the mean of some PDF is determined by samples in  $\mathcal{N}$ . This produces another sequence with locally reduced variance. This new sequence may contain local extrema, which we consider as outliers. Thus, the filtering process is iterated until the limiting sequence in the Cauchy sense, *i.e.* the root signal, is attained. More precisely, to arrive at  $E\{g(n)\}$  for all  $n$ , we propose the following iterative method.

- 1) Each iteration  $i$  begins by determining the set of locations of local maxima (peaks) and local minima (valleys). The locations of these extrema are defined by the set

$$\mathcal{N}_E = \{n \mid g_{i-1}(n) \text{ meets condition 1 or 2} \} \quad (12)$$

Condition 1:  $g_{i-1}(n) > g_{i-1}(n-1)$  and  $g_{i-1}(n) > g_{i-1}(n+1)$ ,

Condition 2:  $g_{i-1}(n) < g_{i-1}(n-1)$  and  $g_{i-1}(n) < g_{i-1}(n+1)$ .

The local peaks and valleys of a length twenty randomly generated sequence are shown in Fig. 2 as  $\triangle$  and  $\nabla$ , *resp.* This length twenty sequence only has seven samples that are

not considered a local extremum. They occur at sample 0, 3, 4, 6, 14, 18, and 19. The first and last samples are never considered as extrema and get replaced by the local mean after convergence is verified. All the other samples are either a local peak or a local valley, so in this example the set  $\mathcal{N}_E = \{1, 2, 5, 7, 8, 9, 10, 11, 12, 13, 15, 16, 17\}$ .

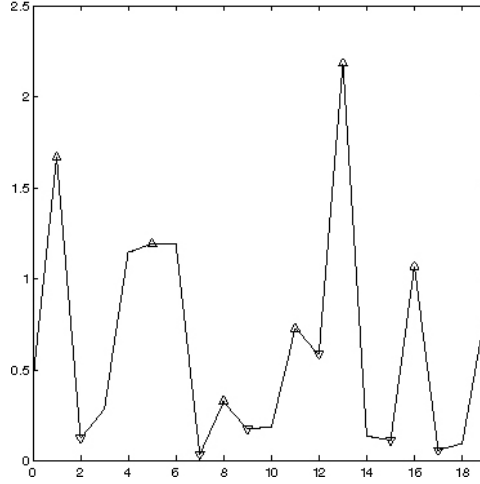


Fig. 2. Step 1 of SBF:  $\triangle$  indicates a local maximum and  $\nabla$  indicates a local minimum.

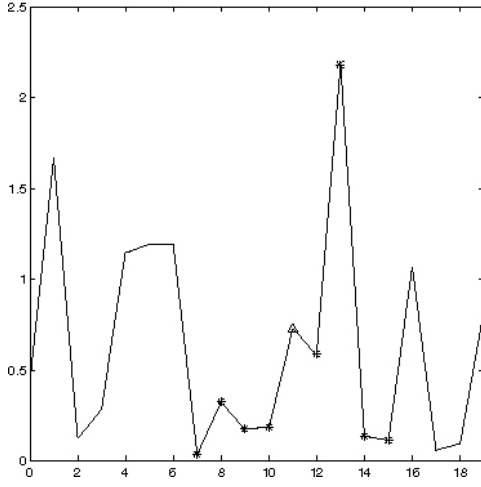
- 2) Without using the local extrema values, poll neighboring samples to determine the local mean. These extrema are replaced with the local mean values that is for  $n \in \mathcal{N}_E$

$$g_i(n) = \frac{1}{|\mathcal{N}|} \sum_{m \in \mathcal{N}} g_{i-1}(m) \quad (13)$$

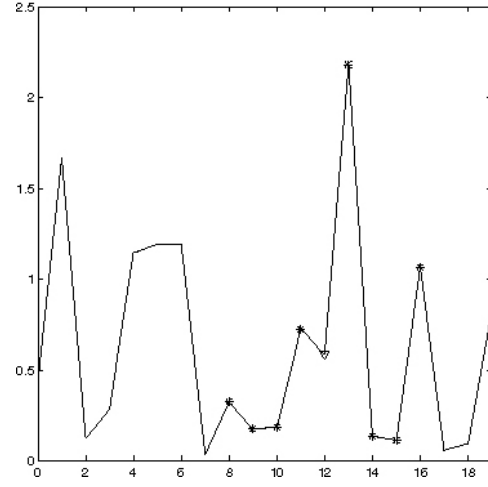
where  $\mathcal{N}$  is some local neighborhood of  $n$ ,  $|\mathcal{N}|$  is the cardinality of set  $\mathcal{N}$ , and  $n \notin \mathcal{N}$ .

In Fig. 3, we illustrate with astricks (\*) the possible values used to calculate the local means of a local maximum ( $\triangle$ ) and a local minimum ( $\nabla$ ) in Figs 3(a) and 3(b), *resp.*

The values shown as  $\triangle$  and  $\nabla$  are not used to calculate the local mean. In Fig. 4 we show the replacement values of each extrema as “o”s.



(a) A local maximum is shown with a  $\triangle$ .  
The astricks (\*) show possible values used  
to compute the local mean.



(b) A local minimum is shown with a  $\nabla$ .  
The astricks (\*) show possible values used  
to compute the local mean.

Fig. 3. Step 2. The \* denote the possible sample values used to determine the local mean. Note that the local peak shown as a  $\triangle$  and the valley shown as  $\nabla$  are not used to determine the local mean.

3) If convergence in the Cauchy sense is not attained, that is

$$\sum_n |g_{i-1}(n) - g_i(n)| > \epsilon \quad (14)$$

for some predefined  $\epsilon > 0$ , then another iteration is performed. If Cauchy convergence is attained, then  $g_i(n)$  is termed the root signal. Essentially nonconvergence indicates a substantial amount of peaks and valleys still exists. Convergence indicates that the outlier values are removed. The ideal signal is the root signal in the additive noise case

$$f(n) \approx g_i(n). \quad (15)$$

In the multiplicative noise restoration case the ideal noise free signal is taken to be the

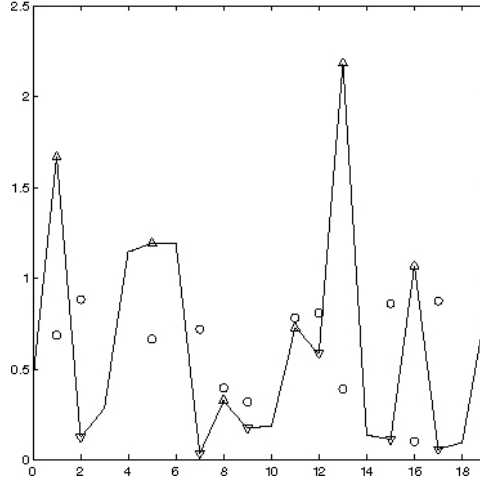


Fig. 4. Step 3 of SBF: local mamimum ( $\triangle$ ) and local minimum ( $\nabla$ ) are replaced by the mean within a local neighborhood ( $\circ$ ).

root signal scaled by the reciprocal of the nonzero expected value of the stationary noise,

$$f(n) \approx \frac{g_i(n)}{E\{\eta(n)\}}. \quad (16)$$

To show that this method produces a convergent sequence of sequences, let  $g_i(n)$  be the sequence produced by the  $i^{th}$  iteration of the proposed method, where  $g_0(n) = g(n)$ . Denote the local minimum value in a neighborhood  $\mathcal{N}'$  of sequence  $g_i(n)$  as  $m_i = \min\{g_i(n) \mid n \in \mathcal{N}'\}$  and analogously the local maximum value in  $\mathcal{N}'$  of the sequence  $g_i(n)$  as  $M_i = \max\{g_i(n) \mid n \in \mathcal{N}'\}$ . It is clear by the definition that  $m_i \leq g_i(n) \leq M_i$  or equivalently restated  $g_i(n) \in [m_i, M_i]$  for all  $n \in \mathcal{N}'$ . Suppose at some iteration  $i$  that  $g_i(n')$  is a local extremum, we replace  $g_i(n')$  with the mean of  $\{g_i(\tilde{n}) \mid \tilde{n} \in \mathcal{N} \text{ and } \tilde{n} \neq n'\}$ . We get  $m_i \leq g_{i+1}(n') \leq M_i$ . Thusly, we can ascertain that  $m_i \leq m_{i+1}$  and  $M_{i+1} \leq M_i$ . Equivalently restated, we have a nested set relation  $[m_{i+1}, M_{i+1}] \subset [m_i, M_i]$ . As the iteration  $i$  is allowed to go to infinity, the nested set of possible values of  $g_i(n)$  converges to some single value. Since the local peaks and valleys are iteratively replaced by a collapsing range of values over some local neighborhood, we aptly name this

method the squeeze box filter (SBF). In our implementation of the SBF, we only check for Cauchy convergence, that is give some  $\epsilon > 0$  when

$$\sum_{n=-\infty}^{\infty} (g_i(n) - g_{i+1}(n))^2 < \epsilon \quad (17)$$

then  $g_{i+1}(n)$  is deemed the limiting signal or what we like to refer to as the root signal.

#### IV. SIGNAL RESTORATION

##### A. Additive Noise Restoration

There are a number excellent methods to perform restoration for signals degraded by the additive noise of equation (1) that are not constrained to piecewise constant signals. We admittedly believe when no such regularization constraints are provided, the additive noise restoration provided by the SBF maybe subpar when compared with methods such as wavelet thresholding, median filtering, Wiener filtering, OSF, and others. When constrained to piecewise constant sequences the robustness of the SBF is exemplary in the two opposing task of decreasing the variation in intervals where the ideal signal is constant and preservation of edges.

In the context of the additive model given in equation (1), assuming the noise has a stationary zero mean PDF, to attain the ideal signal  $f(n)$ , it is only required to determine the expected value of the detected signal  $g(n)$ , that is

$$\begin{aligned} E\{g(n)\} &= E\{p(n) * f(n) + \eta(n)\} \\ &= p(n) * f(n) + E\{\eta(n)\} \\ &= p(n) * f(n). \end{aligned}$$

Thus, a robust method to arrive at  $E\{g(n)\}$  yields  $p(n) * f(n)$ . A deconvolution method such as applying the Weiner filter [13] to  $E\{g(n)\}$  would provide an estimation for the ideal signal  $f(n)$ . This step is ignored in the additive noise examples in section V.



### B. Multiplicative Noise Restoration

Our proposed restoration method is not limited to reconstruction of the ideal signal polluted by zero mean white Gaussian noise, but given this typical assumption of the noise, it will be shown that the blurring caused by the system impulse response can be mathematically accounted for in the variance of the density function. It will be shown that this translates to including the  $l^2$ -norm of the impulse response in the final scaling of the root signal.

The SBF requires that the expected value of the noise to be nonzero. When starting with a zero mean random variable, to productively apply the SBF, the random variable must be transformed so that the SBF can be applied to the resulting nonzero mean random variable. So given a zero mean normally distributed random variable  $X$  with variance  $\sigma_X^2$  the PDF is defined as

$$\Pr_X(x) = \frac{1}{\sigma_X \sqrt{2\pi}} e^{-\frac{x^2}{2\sigma_X^2}} \quad (18)$$

where  $\sigma_X^2 = E\{(X - E\{X\})^2\}$ . Now, the random variable defined by taking the absolute value  $y = |x|$  is a non-Gaussian distributed random variable and  $y \in [0, \infty)$  with a nonzero mean, unless the variance of the original random variable was zero<sup>6</sup>. The PDF of  $y$  is the exponential distribution

$$\Pr_Y(y) = \Pr_Y(|x|) = \begin{cases} \Pr_X(0) & \text{if } y = 0 \\ 2\Pr_X(y) & \text{if } 0 < y \end{cases} \quad (19)$$

where  $\Pr_X(x)$  is given in equation (18). The expected value of  $Y$  is determined as

$$\begin{aligned} E\{Y\} &= \int_0^\infty y \Pr_Y(y) dy \\ &= \frac{2}{\sigma_X \sqrt{2\pi}} \int_0^\infty y e^{-\frac{y^2}{2\sigma_X^2}} dy. \end{aligned} \quad (20)$$

<sup>6</sup>This is consider a noninteresting case and save for this footnote is ignore.

With a simple substitution ( $u = y^2$ ), the integral in equation (20) can be evaluated and

$$E\{Y\} = \sigma_X \sqrt{\frac{2}{\pi}} \quad (21)$$

is easily derived. If  $y = c|x|$  for some constant  $c \geq 0$ , then

$$E\{Y\} = c\sigma_X \sqrt{\frac{2}{\pi}}. \quad (22)$$

When the ideal signal is equal to a constant  $f(n) = c \geq 0$ , the expected value of the absolute value of the multiplicative model from equation (2) is

$$\begin{aligned} E\{|g(n)|\} &= E\{|p(n) * (f(n)\eta(n))|\} \\ &= cE\left\{\left|\sum_{m=-\infty}^{\infty} p(m)\eta(n-m)\right|\right\}. \end{aligned} \quad (23)$$

We have assumed that the noise component is zero mean, normally, independent, and identically distribute random variable. It is shown in [27] that the weighted sum of normally distributed random variables

$$X = \sum_{m=-\infty}^{\infty} p(m)\eta(n-m) \quad (24)$$

is a normally distributed random variable with a standard deviation of

$$\sigma_X = \sigma_\eta \sqrt{\sum_{m=-\infty}^{\infty} p^2(m)}. \quad (25)$$

Substituting equation (25) into equation (22) in the context of equation (23), we get

$$E\{|g(n)|\} = c\sigma_\eta \sqrt{\frac{2}{\pi} \sum_{m=-\infty}^{\infty} p^2(m)}. \quad (26)$$

Using the root signal of the SBF to determine  $E\{|g(n)|\}$ , the ideal signal  $f(n) = c$  is acquired by an appropriate scaling of the root signal, that is

$$f(n) = E\{|g(n)|\} \sqrt{\frac{\pi}{2\sigma_\eta^2}} \left( \sum_{m=-\infty}^{\infty} p^2(m) \right)^{-\frac{1}{2}}. \quad (27)$$

## V. EXAMPLES AND COMPARATIVE RESULTS

In this section, we provide examples using three different piecewise constant sequences corrupted by a stationary zero mean white Gaussian noise and a signal acquired from one column of a Field II simulated ultrasound image [28]. The three noisy piecewise constant sequences are either convolved with the delta function, a known finite length low pass filter with  $l^2$ -norm equal to one, or the known low pass filter scaled so that the  $l^2$ -norm is equal to three. The values of the unit impulse response are listed in table I and shown in Fig. 5. For all the test sequence

$p(0)$	0.4714	
$p(-1)$	0.4362	$p(1)$
$p(-2)$	0.3457	$p(2)$
$p(-3)$	0.2345	$p(3)$
$p(-4)$	0.1363	$p(4)$
$p(-5)$	0.0678	$p(5)$
$p(-6)$	0.0289	$p(6)$
$p(-7)$	0.0105	$p(7)$
$p(-8)$	0.0033	$p(8)$
$p(-9)$	0.0009	$p(9)$

TABLE I

VALUES OF THE UNIT  $l^2$ -NORM IMPULSE RESPONSE USED IN THE TEST SEQUENCES.

$\eta(n)$  is a stationary white zero mean normally distributed random variable,  $\tilde{p}(n) = 3p(n)$ , and

$*$  denotes linear convolution.

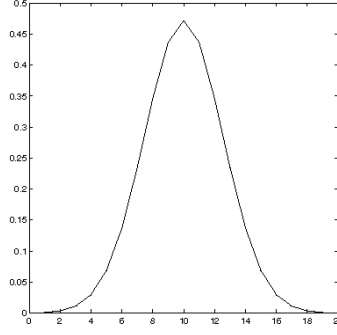


Fig. 5. The length 19 impulse response.

The ideal sequences used in table II are

$$f_0(n) = \begin{cases} 1 & \text{if } 0 \leq n \leq 99 \\ 5 & \text{if } 100 \leq n \leq 199 \\ 1 & \text{if } 200 \leq n \leq 299, \end{cases} \quad (28)$$

,

$$f_1(n) = \begin{cases} 5 & \text{if } 0 \leq n \leq 99 \\ 1 & \text{if } 100 \leq n \leq 199 \\ 5 & \text{if } 200 \leq n \leq 299, \end{cases} \quad (29)$$

and

$$f_2(n) = \begin{cases} 10 & \text{if } 0 \leq n \leq 99 \\ 5 & \text{if } 100 \leq n \leq 199 \\ 1 & \text{if } 200 \leq n \leq 299 \\ 5 & \text{if } 300 \leq n \leq 399. \end{cases} \quad (30)$$

#### A. A Comparative Qualitative Assessment

The original noisy signals and results of the SBF are shown in Figs 8, 9, 10, and 11, *resp.* Though exact restoration is desired, the resulting signal produced by the SBF resemble the ideal piecewise constant signal. It is evident that the SBF is proficient at decreasing the variance in

I	$g_1(n) = f_0(n) + \eta(n)$
II	$g_2(n) = f_1(n) + \eta(n)$
III	$g_3(n) = f_2(n) + \eta(n)$
IV	$g_4(n) =  f_0(n)\eta(n) $
V	$g_5(n) =  p(n) * [f_0(n)\eta(n)] $
VI	$g_6(n) =  \tilde{p}(n) * [f_0(n)\eta(n)] $
VII	$g_7(n) =  f_1(n)\eta(n) $
VIII	$g_8(n) =  p(n) * [f_1(n)\eta(n)] $
IX	$g_9(n) =  \tilde{p}(n) * [f_1(n)\eta(n)] $
X	$g_{10}(n) =  f_1(n)\eta(n) $
XI	$g_{11}(n) =  p(n) * [f_2(n)\eta(n)] $
XII	$g_{12}(n) =  \tilde{p}(n) * [f_2(n)\eta(n)] $

TABLE II

TEST SEQUENCES.

intervals where the ideal signal is a constant while greatly preserving both step up and step down edges.

Fig. 6 is a Field II simulation [28] of an B-scan envelop detected and log compressed ultrasound image of five circular disks of the same diameter. The five disks are representatives of highly reflective cysts. This simulation is representative an image produced by a typical clinical ultrasound. Though the extension of the SBF to a two dimensional filter is straightforward, we save this extension for future publications and examine only one column of the simulated image. Fig. 7(a) we show the intensity profile of the center column of Fig. 6. The results of the SBF and moving average filter are in Fig. 7(b). The solid plot of Fig. 7(b) is the root signal found by the SBF and the dashed plot is the signal produced by the moving average filter. Though

we created the image where the ideal reflectivity values of the background are set to one and the values within the disks are set to ten, Field II, which claims a realistic representation of an actual ultrasound images, has rendered a visually appealing image but the true reflectivity values maybe impossible to recover. Nonetheless and important to visual acuity, the SBF has traced out a profile that is large constant in intervals that corresponds to the location occupied by the disks while the large differences in intensity values with intervals occupied by the disks and the background are preserved. The varying degree of the intensity values of the root signal produced by the SBF in intervals occupied by the disks may be explain by a unknown spatially varying PSF in the original simulated image. A spatially varying PSF is a known phenomena that occurs with fixed focus ultrasonic imaging systems. Since the PSF is spatially varying, it is reasonable to believe that the  $l^2$ -norm of the impulse response of the signal in each column of the simulated image is varying. Thus, each homogeneous intervals are scaled differently. This example serves to fortify our claim that for either additive or multiplicative noisy signals, which are representative of signals produced by ultrasonic imaging systems, the SBF is robust in reducing the variance in regions where the signal is constant while maintaining the opposing task of edge preservation.

### *B. A Comparative Quantitative Assessment*

To provide a quantitative assessment on the signal restoration performance of the SBF, the moving average filter, the median filter, Bovik *et. al.*'s OSF optimized for a Laplacian noise distribution, Wiener filter, the DWT hard and soft thresholding methods, we use a modified well known contrast metric used to measure contrast. For test sequence I, II, IV, V, VII, VIII, X, and

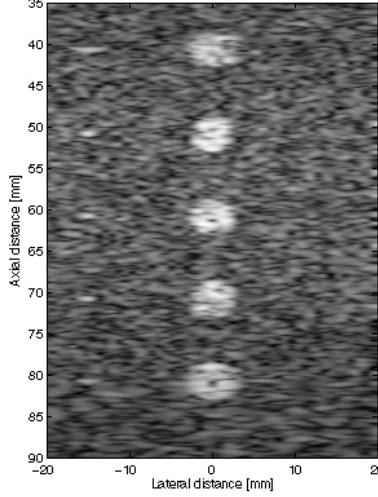


Fig. 6. Field II ultrasound image simulation.

XI to objectively evaluate the performance of a restoration algorithm let  $\hat{Q}(alg)$  be defined as

$$\hat{Q}(alg) = \frac{(\mu_1 - \mu_2)^2}{\sigma_1^2 + \sigma_2^2} \quad (31)$$

where  $g_{alg}(n)$  is the sequence produced by restoration algorithm 'alg',

$$\mu_i = \frac{1}{|I_i|} \sum_{n \in I_i} g_{alg}(n), \quad (32)$$

$$\sigma_i^2 = \frac{1}{|I_i|} \sum_{n \in I_i} (g_{alg}(n) - \mu_i)^2, \quad (33)$$

$I_1 = [0, 99] \cup [200, 299]$ , and  $I_2 = [100, 199]$ . For test sequence III, VI, and IX, we use the following performance metric

$$\hat{Q}(alg) = \frac{(\mu_1 - \mu_2)^2 + (\mu_1 - \mu_3)^2 + (\mu_2 - \mu_3)^2}{\sigma_1^2 + \sigma_2^2 + \sigma_3^2} \quad (34)$$

where  $\mu_i$  is defined in equation (32),  $\sigma_i^2$  is defined in equation (33),  $I_1 = [0, 99]$ ,  $I_2 = [100, 199] \cup [300, 399]$ , and  $I_3 = [200, 299]$ . The performance metric we use is the following ratio

$$Q(alg) = \frac{\hat{Q}(alg)}{\hat{Q}(id)} \quad (35)$$

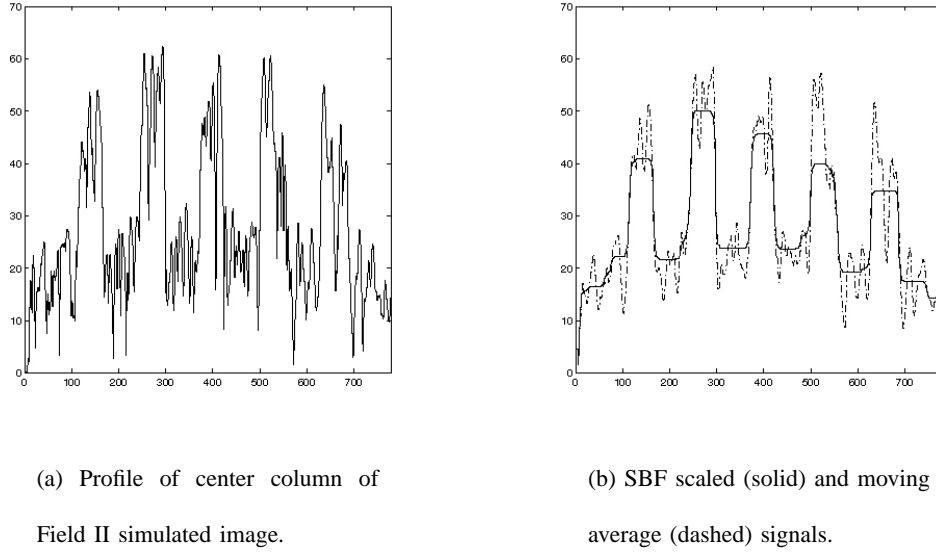


Fig. 7. Intensity profile of center column of Fig. 7, SBF root, and moving averaged sequences.

where  $g_{id}(n) = g(n)$ . When  $Q(alg)$  is a large number greater than one (preferred), then  $alg$  performs well. If  $Q(alg)$  is equal to one, then  $alg$  does not provide any improvements to the noisy signal. If  $Q(alg)$  is less than one, then the tested algorithm  $alg$  degrades the noisy signal.

In our experiment when performing the multiplicative noise restoration with Bovik's OSF optimized Laplacian distributed noise, DWT Hard and Soft thresholding, Wiener filtering, we logarithmically transformed the noisy signal in an attempt to cast the restoration as additive noise, which these filters were design to overcome. The exponentially transformed values of these filters were then used in the quantitative evaluation. In table III we list the results of these quantitative evaluations. The highest performance values in every case were attained by the SBF. This evaluation provide evidence that the SBF performs exceedingly well.

## VI. CONCLUSION

The additive and multiplicative signal restoration problem is relevant to many interesting applications like ultrasound and SAR imaging. In this paper, we constraint the solution to



Test sequence $\rightarrow$	<i>I</i>	<i>II</i>	<i>III</i>	<i>IV</i>	<i>V</i>	<i>VI</i>	<i>VII</i>	<i>VIII</i>	<i>IX</i>	<i>X</i>	<i>XI</i>	<i>XII</i>
$Q(MA)$	4.91	5.3	4.66	9.62	2.54	1.98	9.46	2.03	2.07	18.0	2.26	1.89
$Q(Median)$	4.35	7.79	5.22	4.65	1.75	1.41	5.81	1.82	1.65	14.0	1.65	1.64
$Q(OSF)$	5.24	6.59	5.42	6.01	2.0	1.53	6.49	1.83	1.64	12.77	1.72	1.66
$Q(Wnr)$	1.0	1.0	1.0	1.26	0.79	1.0	1.18	0.78	0.74	1.32	0.98	1.11
$Q(Hard)$	4.07	3.19	4.01	4.15	1.1	0.0	1.77	1.45	0.03	8.64	1.26	0.09
$Q(Soft)$	0.60	0.69	0.81	0.01	0.02	1.0	0.04	0.01	0.82	0.18	0.15	0.9
<b>SBF</b>	<b>7.18</b>	<b>7.88</b>	<b>5.4</b>	<b>23.01</b>	<b>20.21</b>	<b>20.82</b>	<b>36.11</b>	<b>7.58</b>	<b>6.77</b>	<b>71.31</b>	<b>16.35</b>	<b>21.56</b>

TABLE III

$Q$  VALUES FOR THE MOVING AVERAGE (*MA*), MEDIAN (*MEDIAN*), BOVIK'S OSF OPTIMIZED FOR ADDITIVE AND LAPLACIAN DISTRIBUTED NOISE (*OSF*), WIENER (*Wnr*), DWT HARD THRESHOLDING (*Hard*), DWT SOFT THRESHOLDING (*Soft*), AND SBF RESTORATION METHODS.

piecewise constant signals. When the restoration problem is viewed in the stochastic framework, it can be analytically shown that the ideal signal can be attained from a well know and easily provable property of the expectation operator. The practical implementation of this easily provable property is problematic and philosophically debateable. We overcome these problems by designing a stochastically driven method the SBF to determine the root signal of a noisy signal. In the additive noise restoration, the SBF was able to extract a exceedingly accurate depiction of the ideal noise free signal. The empirical evidence shows in the multiplicative noise restoration case that multiplication with the analytically derived scaling factor to the root signal yields a signal that very well resembles and very closely approximates the ideal signal. At the very least, the claim that the SBF produces a signal with reduced variances in intervals where the ideal signal is constant while the opposing task of preserving edges is equally maintained is

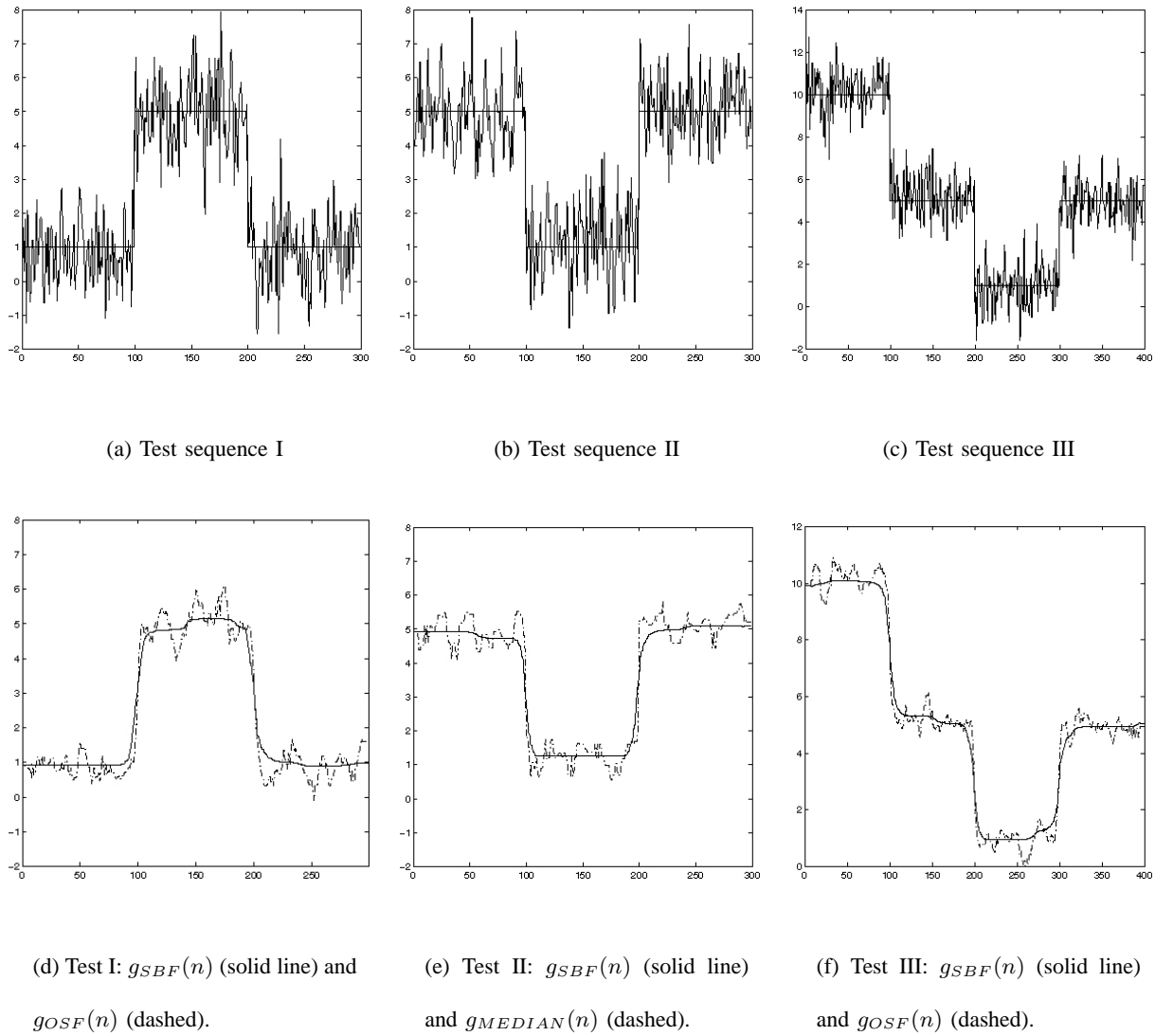


Fig. 8. Test I, Test II, and Test III noisy, ideal, SBF root, and next best Q valued sequences.

subjectively and objectively supported by the results of our experimentations.

#### ACKNOWLEDGMENT

This work was supported by NIH NIBIB grant EB001826 and US Army CDMRP grant (W81XWH-04-1-0240).

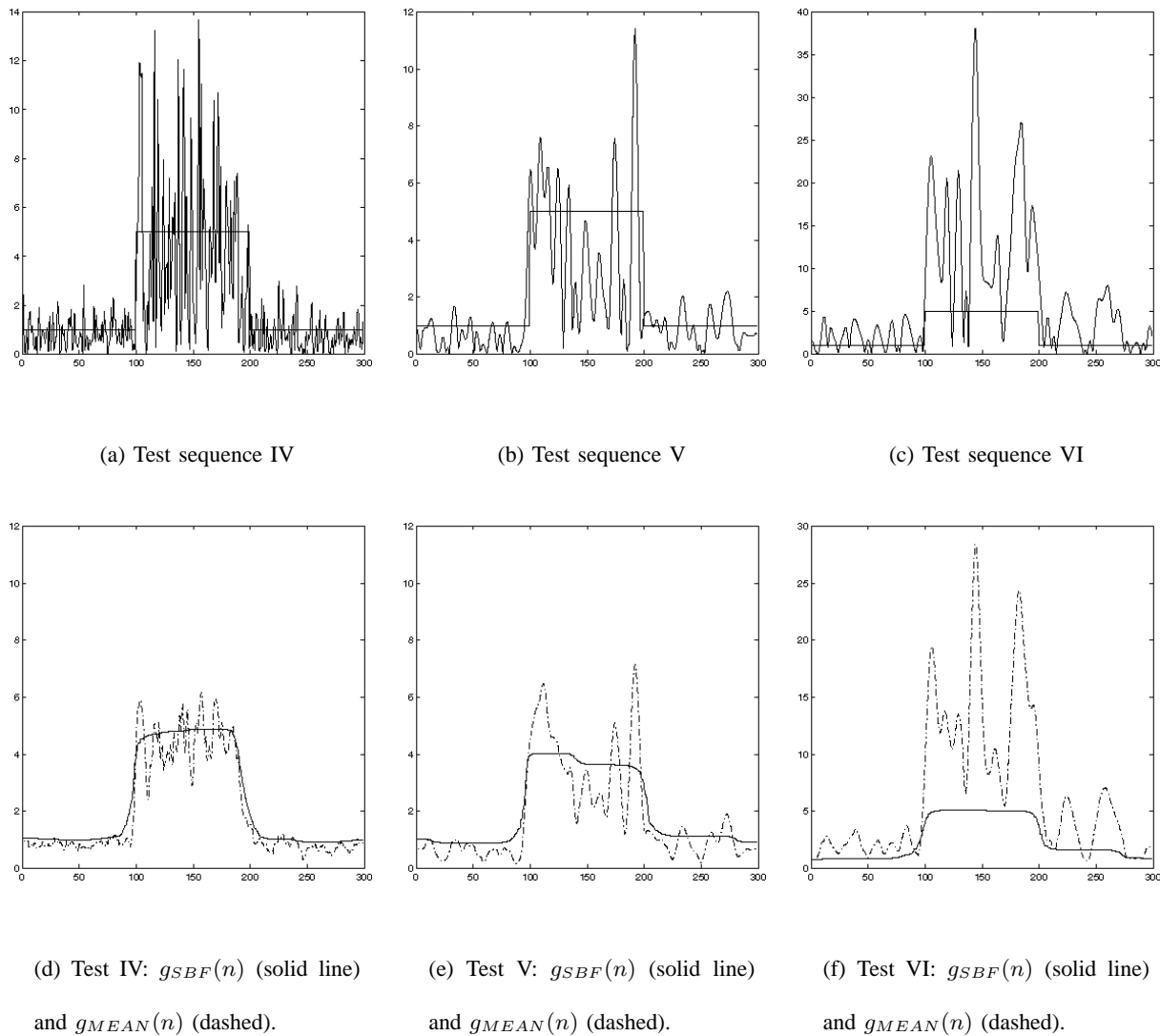


Fig. 9. Test IV, V, VI noisy, ideal, SBF scaled root, and moving averaged sequences.

## REFERENCES

- [1] J. T. Bushberg, J. A. Seibert, J. E. M. Leidholdt, and J. M. Boone, *The essential physics of medical imaging*. Baltimore: Williams and Wilkins, 1994.
- [2] A. Restrepo and A. C. Bovik, "Locally monotonic regression," *IEEE Trans. Signal Processing*, vol. 41, no. 9, pp. 2796–2810, Sept. 1993.
- [3] P. Perona and J. Malik, "Scale-space and edge detection using anisotropic diffusion," *IEEE Trans. Pattern Anal. Machine Intell.*, vol. 12, no. 7, pp. 629–639, July 1990.

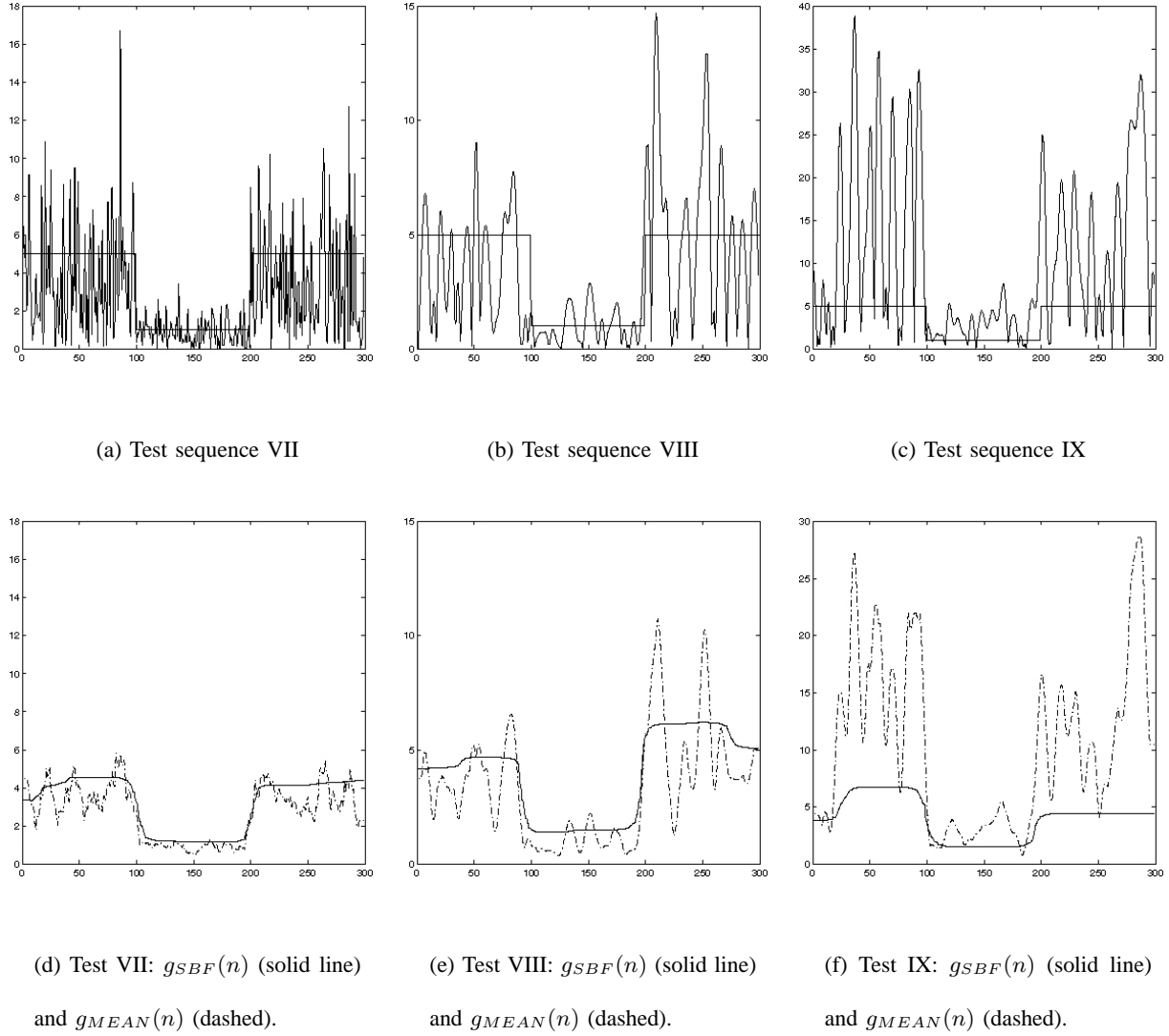
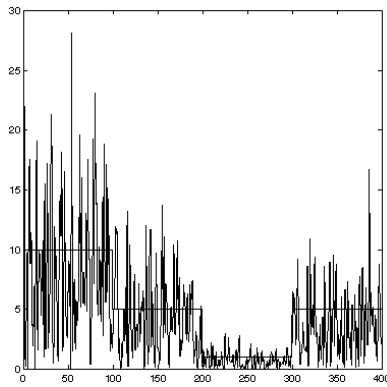
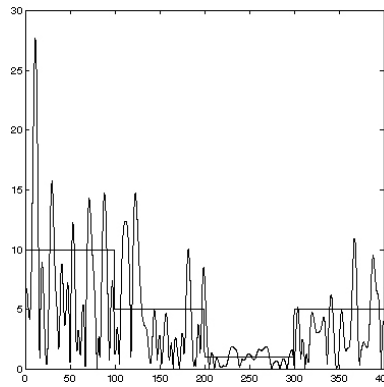


Fig. 10. Test VII, VIII, IX noisy, ideal, SBF scaled root, and moving averaged sequences.

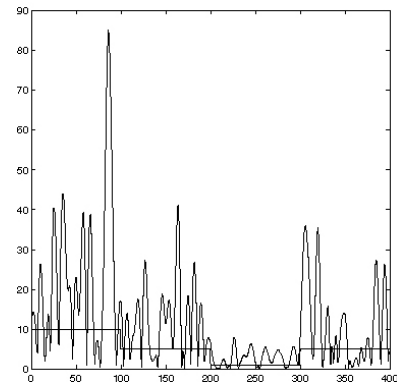
- [4] A. Restrepo and A. C. Bovik, "Adaptive trimmed mean filters for image restoration," *IEEE Trans. Acoust., Speech, Signal Processing*, vol. 36, no. 8, pp. 1326–1337, August 1988.
- [5] P. Charbonnier, L. Blanc-Féraud, G. Aubert, and M. Barlaud, "Deterministic edge-preserving regularization in computed imaging," *IEEE Trans. Image Processing*, vol. 6, no. 2, pp. 298–311, Feb. 1997.
- [6] S. Teboul, L. Blanc-Féraud, G. Aubert, and M. Barlaud, "Variational approach for edge-preserving regularization using coupled PDE's," *IEEE Trans. Image Processing*, vol. 7, no. 3, pp. 387–397, March 1998.
- [7] Y. You and M. Kaveh, "Blind image restoration by anisotropic regularization," *IEEE Trans. Image Processing*, vol. 8,



(a) Test sequence X



(b) Test sequence XI



(c) Test sequence XII

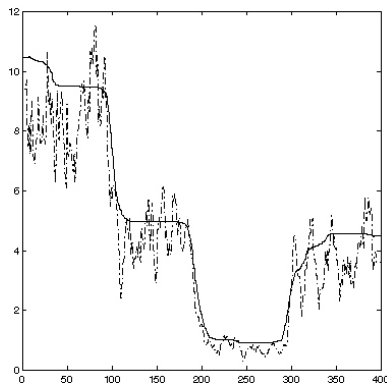
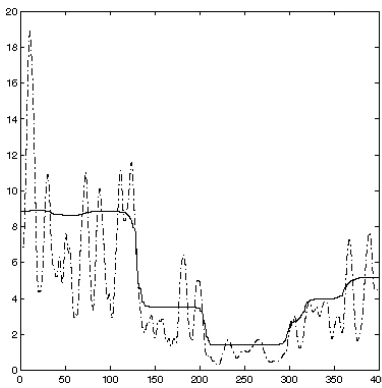
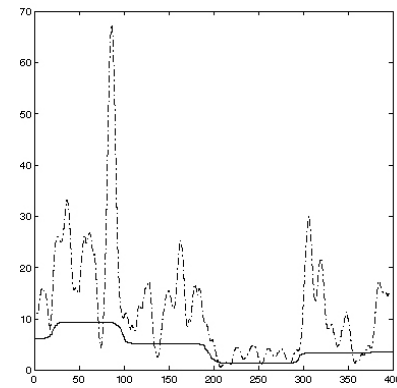
(d) Test X:  $g_{SBF}(n)$  (solid line)  
and  $g_{MEAN}(n)$  (dashed).(e) Test XI:  $g_{SBF}(n)$  (solid line)  
and  $g_{MEAN}(n)$  (dashed).(f) Test XII:  $g_{SBF}(n)$  (solid line)  
and  $g_{MEAN}(n)$  (dashed).

Fig. 11. Test X, XI, XII noisy, ideal, SBF scaled root, moving averaged sequences.

no. 3, pp. 396–407, March 1999.

- [8] R. F. Wagner, S. W. Smith, J. M. Sandrik, and H. Lopez, “Statistics of speckle in ultrasound B-scans,” *IEEE Trans. Sonics Ultrason.*, vol. 30, no. 3, pp. 156–163, May 1983.
- [9] R. F. Wagner, M. F. Insana, and S. W. Smith, “Fundamental correlation lengths of coherent speckle in medical ultrasonic images,” *IEEE Trans. Ultrasonics, Ferro., and Freq. Control*, vol. 35, no. 1, pp. 34–44, Jan. 1988.
- [10] T. Loupas, W. N. McDicken, and P. L. Allan, “An adaptive weighted median filter for speckle suppression in medical ultrasonic images,” *IEEE Trans. Circuits Syst.*, vol. 36, no. 1, pp. 129–135, January 1989.

- [11] M. Karaman, M. A. Kutay, and G. Bozdagi, "An adaptive speckle suppression filter for medical ultrasonic imaging," *IEEE Trans. Med. Imag.*, vol. 14, no. 2, pp. 283–292, June 1995.
- [12] S. Mallat, *A wavelet tour of signal processing*. San Diego: Academic Press, 1998.
- [13] T. Kailath, "Equations of Wiener-Hopf type in filtering theory and related applications," in *Norbert Wiener: Collected Works vol. III*, P. Masani, Ed. Cambridge, MA: MIT Press, 1976, pp. 63–94.
- [14] M. Nagao and T. Matsuyama, "Edge preserving smoothing," *Computer Graphics and Image Processing*, vol. 9, no. 4, pp. 394–407, April 1979.
- [15] J. S. Lee, "Digital image enhancement and noise filtering by use of local statistics," *IEEE Trans. Pattern Anal. Machine Intell.*, vol. PAMI-2, no. 2, pp. 165–168, March 1980.
- [16] D. T. Kuan, A. A. Sawchuk, T. C. Strand, and P. Chavel, "Adaptive noise smoothing filter for images with signal-dependent noise," *IEEE Trans. Pattern Anal. Machine Intell.*, vol. PAMI-7, no. 2, pp. 165–177, March 1985.
- [17] —, "Adaptive restoration of images with speckle," *IEEE Trans. Acoust., Speech, Signal Processing*, vol. ASSP-35, no. 3, pp. 373–383, March 1987.
- [18] C. Moloney, "Smoothing of SAR image speckle noise by multiplicative point estimation filters," in *Proc. IEEE Int'l. Conf. Image Proc.*, Lausanne, Switzerland, Sept. 16-19 1996, pp. 907–910.
- [19] V. S. Frost, J. A. Stiles, K. S. Shanmugan, and J. C. Holtzman, "A model for radar images and its application to adaptive digital filtering of multiplicative noise," *IEEE Trans. Pattern Anal. Machine Intell.*, vol. PAMI-4, no. 2, pp. 157–166, March 1982.
- [20] Y. Yu and S. T. Acton, "Speckle reducing anisotropic diffusion," *IEEE Trans. Image Processing*, vol. 11, no. 11, pp. 1260–1270, November 2002.
- [21] V. Dutt and J. Greenleaf, "Adaptive speckle reduction filter for log-compressed B-scan images," *IEEE Trans. Med. Imag.*, vol. 15, no. 6, pp. 802–813, Dec. 1996.
- [22] A. C. Bovik, "On detecting edges in speckle imagery," *IEEE Trans. Acoust., Speech, Signal Processing*, vol. 36, no. 10, pp. 1618–1627, Oct. 1988.
- [23] A. C. Bovik, T. Huang, and J. D. Munson, "A generalization of median filtering using linear combinations of order statistics," *IEEE Trans. Acoust., Speech, Signal Processing*, vol. 31, no. 6, pp. 1342–1350, Dec. 1983.
- [24] D. Donoho, "De-noising by soft-thresholding," *IEEE Trans. Inform. Theory*, vol. 41, no. 3, pp. 613–627, May 1995.
- [25] H. Krim, D. Tucker, S. Mallat, and D. Donoho, "On de-noising and best signal representation," *IEEE Trans. Inform. Theory*, vol. 45, no. 7, pp. 2225–2238, Nov. 1999.
- [26] S. Mallat, "A theory for multiresolution signal decomposition: the wavelet representation," *IEEE Trans. Pattern Anal.*

*Machine Intell.*, vol. 11, no. 7, pp. 674–693, July 1989.

- [27] A. Papoulis, *Probability, random variables, and stochastic processes*, 2nd ed. New York: McGraw-Hill Book Company, 1984.
- [28] J. A. Jensen and N. B. Svendsen, “Calculation of pressure fields from arbitrarily shaped apodized and excited ultrasound transducers,” *IEEE Trans. Ultrasonics, Ferro., and Freq. Control*, vol. 39, no. 2, pp. 262–267, Feb. 1992.

# A Transform Method To Remove Ultrasound Artifacts and Improve Volume Estimates

Peter .C. Tay\*, Chris Garson†, Scott T. Acton\*, and John Hossack†

\*Depts. of Electrical and Computer/ Biomedical Engineering

†Dept. of Biomedical Engineering

University of Virginia, Charlottesville, VA USA 22904

Email: {ptay,cdg6d,acton,hossack}@virginia.edu

**Abstract**—Reverberation and multi-path reflection artifacts are a common problem in ultrasound imaging. We propose a novel method to remove these artifacts. Regions adversely affected by these artifacts are replaced with textures that resemble the underlying object(s), which were originally obscured. Our proposed method incorporates optimally soft thresholding the 2D discrete wavelet transform of the artifact regions to produce a near optimal estimate of the reflectivity values due only to the reverberation and multi-path reflection artifacts. Simply subtracting this estimate from the original reflectivity values, we attain a near optimal estimate of the artifact free reflectivity values. We provide B mode images to substantiate the benefits of this method in producing a more useful and visually pleasing image.

## I. INTRODUCTION

The use of ultrasound to provide a useful imaging tool is preferred because of the noninvasive and nonionizing nature of this realtime imaging system that can provide functional information like motion and velocities. Although the images and videos produced by a ultrasound system are generally beneficial, its usefulness as a tool to aid medical diagnosis can be improved by removing the various artifacts that may arise. Two types of ultrasound artifacts are caused by reverberation and multi-path reflection of the ultrasonic sound wave as it travels across or around highly reflective objects or interfaces. The description of these artifacts given in [1] are paraphrased in the following:

- Reverberation artifacts occur when reflected ultrasound energy is reflected back and forth between two closely spaced interfaces during signal acquisition and prior to the next transmitted pulse.
- Artifacts due to multi-path reflection occur when the ultrasound beam is nonperpendicularly reflected or refracted off a highly reflective surface and subsequently detected at the transducer.

Since the range<sup>1</sup> is directly related to time in ultrasound imaging, reverberation artifacts can be seen as multiple equal spaced objects with amplitudes decreasing as depth increases. Also, the paths of the nonperpendicularly reflected beams are longer than the paths of perpendicularly reflected beams. Consequently, highly reflective objects may reappear further away from the transducer and the multi-path reflection artifacts

are seen as misplaced objects. In ultrasound images of organs, muscles, or tissues that are in close proximity of highly reflective structures such as bones or tissue/gas interfaces, the undesirable occurrences of reverberation and multi-path reflection artifacts are common.

An example application to show the importance of the removal of these artifacts is improving the ultrasound imaging system so that a 3D rendering of muscles and tissues within the heart can be better observed and important information such as the volume and surface area of the heart can be accurately assessed. In principle, by specifically removing the reverberation and multi-path reflection artifacts caused by the highly reflective nature of the ribs we offer improvements to the B mode or M mode ultrasound images so that the motions and borders of the myocardium<sup>2</sup> of the heart can accurately be evaluated by an automated algorithm, a physician, or both. Additionally, a 3D rendering that depicts the surface of the heart and volume information using these 2D images is not adversely skewed by these common artifacts.

An appropriately placed short axis scans of the left ventricle will show the myocardium contracting and expanding as the heart repeats its end diastole to end systole cycle. In acquiring a short axis view of the heart, the ultrasonic sound wave must traverse through or around the ribs. The highly reflective nature of the ribs can cause reverberation and/or multi-path artifacts to appear within the region of interest that is over or near the myocardium. The presence of these artifacts can obscure parts of the myocardium and makes determining its motions and borders problematic. We attempt to illustrate the problem in Fig. 2(a) where a typical short axis B mode ultrasound image of the left ventricle of a mouse heart is shown. In Fig. 2(a) the approximated location of the inner left ventricle myocardial border is shown by the ellipse. The reverberation or multi-path reflection artifacts most probably caused by the ribs are seen as bright objects. We have highlighted these artifacts with a bold “A” in Fig. 2(a). A B mode image that isolates these artifacts is shown in Fig. 2(b). It can be observed that the leftmost section of the myocardium are made ambiguous by these artifacts. To accurately assess the health of the myocardium or other obscured muscle(s)/tissue(s), it is

<sup>1</sup>The distance from the transducer or depth.

<sup>2</sup>The middle and thickest layer of the heart wall, composed of cardiac muscles [2].



necessary not only to remove these artifacts, but the reflectivity values of the muscle(s)/tissue(s) obscured by these artifacts should be accurately preserved.

## II. BACKGROUND

### A. The Discrete Wavelet Transform

In [3], Mallat's multiresolution wavelet transform provided a two dimensional (2D) subband decomposition of an image that allows perfect reconstruction. Although our proposed artifact removal method strives to remove certain components of the original image, perfect reconstruction is still preferred since no visual information loss due to the transform is guaranteed. Since one of our proposed goal is to render a more visually pleasing reverberation and multi-path reflection artifact free image, our DWT construction emulates the forty-three channel Gabor filter bank of [4]. The 2D filter bank composed of 2D Gabor filters in [4] was motivated by psychophysiological experimental evidence that the early stages of a biological vision system are well represented by conjointly well spatial and frequency localized bank of Gabor filters where the number of channels is in the forties. Another key characterization of this Gabor filter bank construction is that the magnitude response of the filters becomes wider and their magnitudes decrease as the center horizontal and/or vertical frequencies increase. With these characterizations in mind we emulate the Gabor filter bank in [4] with a 2D forty channel well conjointly localized perfect reconstruction DWT filter bank. The forty channel 2D DWT decomposition is shown in Fig. ?? and for comparison purpose the typical thirteen four level DWT decomposition is shown in Fig. ?. Evidence is provide in [5] that shows the multi-level DWT filter bank is conjointly well localized when the Coifman quadrature mirror filter bank (QMF), which maximizes the number vanishing moment for a given support width, is used. A description of the Coifman QMF used in our 2D forty channel DWT filter bank can be found in [6].

### B. Hard and Soft Thresholding Methods

For signals corrupted by additive white Gaussian noise such as in equation (1), a typical denoising method to recover the noise free signal  $x(n)$  is to apply a hard or soft thresholding operator to the DWT coefficients. These methods are commonly referred to as wavelet shrinkage. The hard and soft thresholding operation are given in equations (2) and (3), *resp.* where  $\mathbf{w} = DWT\{\mathbf{y}\}$ .

$$y(n) = x(n) + \eta(n) \quad (1)$$

The noise free signal is reconstructed from the threshold wavelet coefficients  $\hat{\mathbf{y}} = IDWT\{\tilde{\mathbf{w}}\} \approx \mathbf{x}$  where  $IDWT\{\cdot\}$  means inverse DWT (IDWT).

$$\tilde{w}(n) = \begin{cases} 0 & \text{if } |w(n)| < \lambda_{hard} \\ w(n) & \text{otherwise.} \end{cases} \quad (2)$$

$$\tilde{w}(n) = \begin{cases} w(n) - \lambda_{soft} & \text{if } w(n) > \lambda_{soft} \\ w(n) + \lambda_{soft} & \text{if } w(n) < -\lambda_{soft} \\ 0 & \text{otherwise.} \end{cases} \quad (3)$$

The robustness of the wavelet shrinkage method is dependant on the choice of threshold(s). Some various methods and criteria to consider in choosing a global or level dependant hard or soft threshold(s) based on *a priori* known or estimated noise statistics, signal length, mean squared error, and smoothness are described in [7]. In [7], [8], and [9], the wavelet shrinkage denoising of the signal  $y(n)$  using hard or soft thresholding of the DWT coefficient with a global soft threshold value

$$\lambda_{soft} = \sigma \sqrt{2 \ln(N)}, \quad (4)$$

or some variant of this threshold where  $\sigma$  is the standard deviation of the noise and  $N$  is length of the signal, is shown to be optimal or near optimal in the sense that the mean squared error is minimized (MMSE) or the maximum of the mean squared error is minimized (minimax). Additionally the reconstructed signal of the soft threshold wavelet shrinkage method, Donoho in [8] claim is nearly as smooth as the original signal where the smoothness of the reconstructed signal was determined from a "wide range" of smoothness metric [8].

As a stringent motivation in our ultrasound artifact removal algorithm, we desire mean squared error optimality or at least near optimality in the sense of MMSE or minimax. To prevent processing artifacts such as unwarranted oscillations (ringing) or discontinuities, we adhere to the constraint that the reconstructed signal/image should be equivalently as smoothness as the original signal/image. We will take advantage of the work accomplished in [7], [8], and [9] by using the soft threshold wavelet shrinkage method with the threshold value defined as in equation (4) in our proposed algorithm.

## III. THE ARTIFACT REMOVAL METHOD

In [10] Bjaerum and Torp proposed an additive model of the complex demodulated Doppler signal to remove clutter, which are objects that do not move or move slowly. In modeling the complex demodulated  $IQ$  data, we adopted a similar additive model. The model of the  $IQ$  data that we have adopted is the sum of three complex value components

$$IQ(n, m) = A(n, m) + T(n, m) + \eta(n, m) \quad (5)$$

where  $A(n, m)$  is the complex value due to the artifacts,  $T(n, m)$  is the complex reflectivity value due to the underlying muscle(s)/tissue(s) obscured by  $A(n, m)$ , and  $\eta(n, m)$  is complex valued white noise where the real and the imaginary parts of  $\eta(n, m)$  are zero mean Gaussian distributed. It is reasonable to assume that the complex values due to the artifacts and the reflectivity values due to the underlying muscle(s)/tissue(s) are independent of each other.

The B mode data is attained by log compressing the  $L^2$ -norm of the interpolated  $IQ$  data. The data flow of the  $IQ$  data to B mode data is shown in Fig. 1. Although the B mode data is used to produce a visually meaningful image for medical diagnosis, processing the  $IQ$  data is better suited for our current application of removing reverberation and multi-path reflection artifacts. It is more advantageous to process the  $IQ$  data instead of the B mode data for the following reasons:

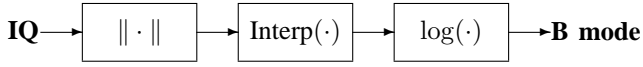


Fig. 1. IQ data to B mode image.

- The values of the IQ data encompass a greater dynamic range than the B mode data. Thus, samples that are greatly affected by artifacts are more easily distinguishable.
- The number of samples of IQ data is substantially less than the number of B mode data. Always important to real time or near real time algorithms is to process the fewest number of samples.
- The signal to noise ratio (SNR) of the IQ data is greater than the SNR of the B mode data where SNR is meant as the ratio of the power due to the underlying muscle/tissue reflectivity values  $T(n, m)$  and the power due to white noise  $\eta(n, m)$ . The reduction in SNR of the B mode data is due to log compression, which is necessary to render an image that is within the dynamic range of human vision.
- The real and imaginary part of  $T(n, m)$  are Gaussian distributed. This detail is required for the optimality or near optimality of the soft thresholding wavelet shrinkage method using the threshold given in equation 4. We will elaborate and establish this detail later in this section.

From the additive model we propose in equation (5), if a sample is adversely affected by the artifact component, then the  $L^2$ -norm of the artifact component is substantially greater than the  $L^2$ -norm of the muscle/tissue component, that is  $\|A(n, m)\| \gg \|T(n, m)\|$ . An estimate of samples where artifacts are prominent can be determined by thresholding the  $L^2$ -norm of the IQ data

$$\widetilde{IQ}(n, m) = \begin{cases} IQ(n, m) & \text{if } \|IQ(n, m)\| > \lambda \\ 0 & \text{otherwise.} \end{cases} \quad (6)$$

The estimated artifact dominated complex data  $\widetilde{IQ}$  contains the complex reflectivity values of the underlying muscle and/or tissue, which are obscured by the artifact(s). To provide an estimate of the reflectivity values of the underlying muscle and/or tissue, we consider the complex reflectivity values of the underlying muscle or tissue  $\widetilde{T}(n, m)$  of the estimated artifact dominated complex data  $\widetilde{IQ}(n, m)$  as unwanted additive noise, that is

$$\widetilde{IQ}(n, m) = \widetilde{A}(n, m) + \underbrace{\widetilde{T}(n, m) + \widetilde{\eta}(n, m)}_{\text{noise}}. \quad (7)$$

Applying a wavelet shrinkage algorithm to the real and imaginary parts of  $\widetilde{IQ}$  to remove  $\widetilde{T}$  and  $\widetilde{\eta}$ , we attain an estimate of the complex values due only to the artifact  $\widehat{\mathbf{A}}$ . More precisely, let  $\mathbf{W}_{real} = DWT\{real\{\widetilde{IQ}\}\}$  and  $\mathbf{W}_{imag} = DWT\{imag\{\widetilde{IQ}\}\}$  be the 2D DWT of the real and imaginary image of  $\widetilde{IQ}$ , *resp.* The soft thresholding of  $\mathbf{W}_{real}$  and  $\mathbf{W}_{imag}$  with thresholds

$$\lambda_{soft,real} = \sigma_{real} \sqrt{2 \ln(|\widetilde{IQ}|)} \quad (8)$$

and

$$\lambda_{soft,imag} = \sigma_{imag} \sqrt{2 \ln(|\widetilde{IQ}|)}, \quad (9)$$

*resp.*, are denoted as  $\widetilde{\mathbf{W}}_{real}$  and  $\widetilde{\mathbf{W}}_{imag}$ , *resp.* The term  $\sigma_{real}$  is the standard deviation of elements in  $\widetilde{IQ}_{real}$  where

$$\widetilde{IQ}_{real} = \{real\{IQ(n, m)\} : \|IQ(n, m)\| \leq \lambda\} \quad (10)$$

with the same  $\lambda$  used in equation (6). Likewise  $\sigma_{imag}$  is the standard deviation of  $\widetilde{IQ}_{imag}$  where

$$\widetilde{IQ}_{imag} = \{imag\{IQ(n, m)\} : \|IQ(n, m)\| \leq \lambda\} \quad (11)$$

with the same  $\lambda$  used in equation (6). The term  $|\widetilde{IQ}|$  in equations (8) and (9) is simply the number of samples where the  $L^2$ -norm of the IQ data is greater than the  $\lambda$  of equation (6).

An estimate of the artifacts in equation (7) is determine as

$$\widehat{\mathbf{A}} = IDWT\{\widetilde{\mathbf{W}}_{real}\} + jIDWT\{\widetilde{\mathbf{W}}_{imag}\}. \quad (12)$$

A artifact free image  $\widehat{IQ}$  is attained by subtracting the estimated artifact values of equation (12) from the original IQ data, that is

$$\widehat{IQ} = IQ - \widehat{\mathbf{A}}. \quad (13)$$

If the component  $\widetilde{T}(n, m)$  in the additive model given in equation (7) can be shown to be Gaussian distributed, then using the soft threshold of equation (4), which we estimate in equations (8) and (9), would yield a near optimal estimate of the artifact values  $\widetilde{A}(n, m)$ . If the component  $\widetilde{T}(n, m)$  were statistically independent with respect to the sample indices  $(n, m) \in \mathbb{Z} \times \mathbb{Z}$ , then optimally in the sense describe by Donoho *et al.* in [7], [8], and [9] could justifiably be claimed<sup>3</sup>.

To establish that  $\widetilde{T}(n, m)$  is Gaussian distributed, we consider the basic characterization of these reflectivity values. In [11] and [12], Goodman characterize the reflectivity values produced by ultrasound, coherent optical laser, and synthetic aperture radar as a sum of complex random phasors

$$\widetilde{T}(n, m) = \sum_{i=0}^{\infty} a_i(n, m) e^{j\varphi_i(n, m)} \quad (14)$$

where  $a_i(n, m)$  and  $\varphi_i(n, m)$  are independent with respect to the variable  $i \in \mathbb{Z}$  and with each other<sup>4</sup>. This specular phenomena occurs naturally and normally with these and other imaging systems. The speckle characterization is due to the “roughness” of the object being imaged with respect to the wavelength of the transmitted sound, light, or electro-magnetic wave. Since  $\widetilde{T}(n, m)$  is the infinite sum of independent variables, the Central Limit Theorem implies that  $\widetilde{T}(n, m)$  is Gaussian distributed.

<sup>3</sup>Since the reflectivity values due to the underlying muscle/tissue are not statistically independent, the arguments for MMSE or minimax optimality made by Dohono *et al.* cannot be invoked.

<sup>4</sup>For fixed  $n, m, i \in \mathbb{Z}$ , the conditional probability of  $a_i(n, m)$  given  $\varphi_i(n, m)$  is equal to the of the probability of  $a_i(n, m)$  and likewise for the conditional probability of  $\varphi_i(n, m)$  given  $a_i(n, m)$  is equal to the probability of  $\varphi_i(n, m)$ .

## IV. RESULTS

### A. Image Artifact Removal

In Fig. 2 we show the B mode images of our proposed reverberation and multi-path artifact removal algorithm. The images shown in Fig. 2 are rendered in the same dynamic range so that an accurate representation of our results can be displayed. Although our processing is performed on the  $IQ$  data, our end result is to improve the quality of the B mode image and we use this mode to display our results. The B mode image in Fig. 2(a) is a short axis view of a mouse heart where the bold capital “A” signifies the presence of an artifact and the ellipse represents the approximate location of the muscle/tissue of interest. In Fig. 2(b) is the B mode image of  $\tilde{IQ}(n, m)$  as defined in equation (6) using  $\lambda = 400$ . The image in Fig. 2(b) contains both prominent artifacts and muscle(s)/tissue(s), which are obscured. The B mode image of the near optimally estimated artifact only reflectivity values  $\hat{A}$  of equation (12) is shown in Fig. 2(c). When compared with the image in Fig. 2(b), the objects and features in the B mode image of Fig. 2(c) are subtly and smoothly diminished. Importantly, it is evident from Fig. 2(c) that no new discontinuity, ripples, blips, or oscillations are introduced by our proposed processing. The B mode image of the approximated artifact free image produced by our algorithm  $\hat{IQ}(n, m)$  is shown in Fig. 2(d). We have yet to make any objective and quantifiable measurements on the robustness of our proposed artifact removal algorithm. From a subjective evaluation of Fig. 2(d), we highlight the following improvements and observations:

- 1) The reverberation and multi-path artifacts, which are evident in Fig. 2(a), are removed.
- 2) The artifact regions have been replaced by textures that are homogeneous with textures from neighboring regions that were not adversely affected by these artifacts.
- 3) Artifact free regions are not diminished by our proposed algorithm.
- 4) No processing artifacts are visibly evident.
- 5) Objects of interest are not morphed, warped, skewed, or disfigured in anyway.
- 6) The image in Fig. 2(d) is not displayed in the full contrast range of the human visual system. A contrast enhancement would render a more visually pleasing image.

### B. 3D Surface Rendering and Volume Estimation

We implement a 3D extension of the 2D gradient vector flow (GVF) active contour (also known as a snake) (cite Xu and Prince) to perform a 3D rendering from 2D slices. The volume of the 3D rendering is calculated as the volume of convex hull of the final 3D GVF snake. In Fig. we shows the 3D contour using unprocessed slices and the volume of this contour is estimated at (some number). In Fig. we show the 3D rendering provided by the 3D GVF snake and using artifact removed slices. The volume enclosed by the 3D contour in Fig. is (some more accurate number). This result is more

accurate to the true volume. Although our evaluation is far from complete, this one example shows the artifact removal is necessary for accurate 3D imaging and our proposed artifact removal method is promising.

## V. CONCLUSION

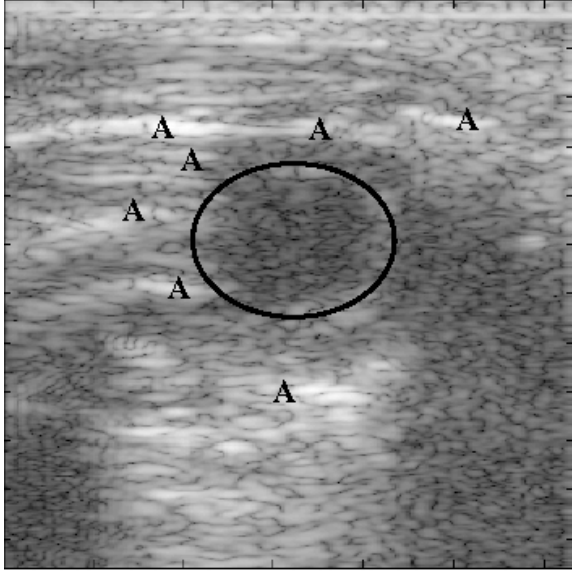
Ultrasound artifacts due to reverberations or multi-path reflections are expected when acquiring images of organs, muscles, tissues, *etc.* require the ultrasonic sound wave to traverse through or around highly reflective objects such as bones or various interfaces. We present a wavelet transform method to replace these artifacts with a near optimal estimate of the underlying objects, which are obscured by these artifacts. For several compelling reasons, our processing is performed fully to the complex  $IQ$  data. Using the resulting B mode data produced by the processed  $IQ$  data, we show that the regions adversely affected by artifacts are replaced with textures that are homogeneous with textures from surrounding regions not adversely affected by these artifacts. Additionally, it can be observed that our proposed artifact removal algorithm is not detrimental to artifact free regions and no processing artifacts are introduced.

## ACKNOWLEDGMENT

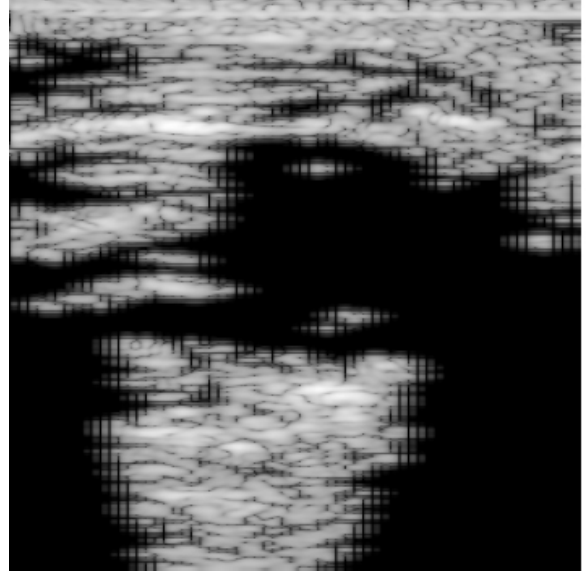
This work was supported by NIH NIBIB grant EB001826 and US Army CDMRP grant (W81XWH-04-1-0240).

## REFERENCES

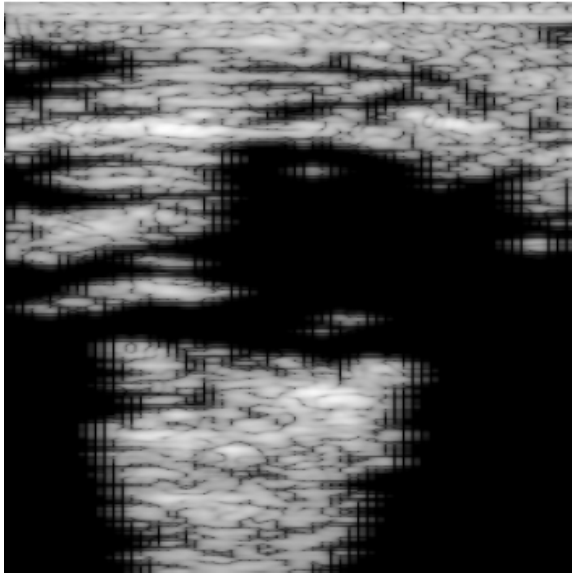
- [1] J. T. Bushberg, J. A. Seibert, J. E. M. Leidholdt, and J. M. Boone, *The essential physics of medical imaging*. Baltimore: Williams and Wilkins, 1994.
- [2] L. R. C. Agnew, D. M. Aviado, J. I. Brody, W. Burrows, R. F. Butler, C. M. Combs, C. M. Gambill, O. Glasser, M. K. Hine, W. B. Shelley, and L. W. Daly, Eds., *Dorland's Illustrated Medical Dictionary*, 24th ed. Philadelphia: W. B. Saunders company, 1965.
- [3] S. Mallat, “A theory for multiresolution signal decomposition: the wavelet representation,” *IEEE Trans. Pattern Anal. Machine Intell.*, vol. 11, no. 7, pp. 674–693, July 1989.
- [4] J. P. Havlicek and A. C. Bovik, “Image modulation models,” in *Handbook of Image and Video Processing*, A. Bovik, Ed. San Diego: Academic Press, 2000, pp. 313–324.
- [5] P. C. Tay, “An optimally well localized multi-channel parallel perfect reconstruction filter bank,” Ph.D. dissertation, University of Oklahoma, 2003.
- [6] Y. Meyer, *Wavelets and Operators*. New York, NY: Cambridge University Press, 1992.
- [7] D. Donoho and I. Johnstone, “Threshold selection for wavelet shrinkage of noisy data,” in *Proc. 16<sup>th</sup> Annual IEEE Int'l. Conf. Engineering Advances: New Opportunities for Biomedical Engineers*, Nov. 3-6 1994, pp. A.24–A.25 vol. 1.
- [8] D. Donoho, “De-noising by soft-thresholding,” *IEEE Trans. Inform. Theory*, vol. 41, no. 3, pp. 613–627, May 1995.
- [9] H. Krim, D. Tucker, S. Mallat, and D. Donoho, “On denoising and best signal representation,” *IEEE Trans. Inform. Theory*, vol. 45, no. 7, pp. 2225–2238, Nov. 1999.
- [10] S. Bjaerum and H. Torp, “Optimal adaptive clutter filtering in color flow imaging,” in *Proc. IEEE Int'l. Ultrasonics Symp.*, Ontario, Canada, Oct. 5-8 1997, pp. 1223–1226.
- [11] J. W. Goodman, “Statistical properties of laser speckle patterns,” in *Laser Speckle and Related Phenomena*, J. C. Dainty, Ed. Berlin: Springer-Verlag, 1984, pp. 9–75.
- [12] —, “Speckle phenomena in optics: Theory and applications version 5.0,” <http://www-ee.stanford.edu/~goodman/>, Aug. 2005.



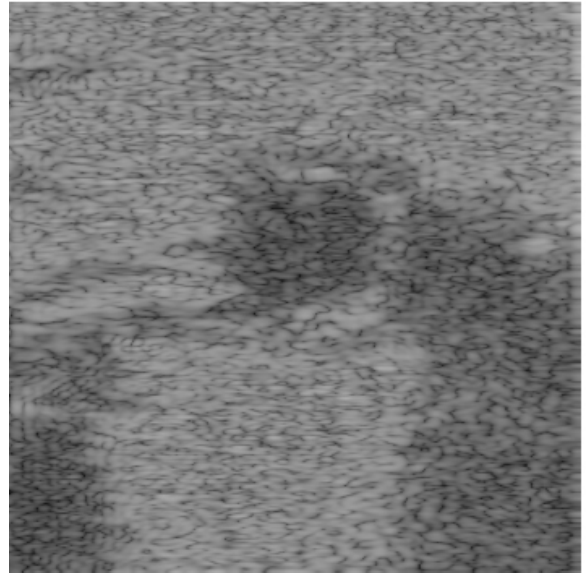
(a) The original image with artifacts (A) and approximate location of myocardium (ellipse).



(b) Unprocessed artifact image  $\widetilde{\mathbf{I}\mathbf{Q}}$  using  $\lambda = 400$



(c) Estimated artifact only image  $\widehat{\mathbf{A}}$ .



(d) Artifact free image  $\widehat{\mathbf{I}\mathbf{Q}}(n, m)$

Fig. 2. B mode version of original, unprocessed artifact, processed artifact, and artifact free images.

# A STOCHASTIC APPROACH TO ULTRASOUND DESPECKLING

Peter C. Tay and Scott T. Acton

Depts. of ECE and BME  
University of Virginia  
Charlottesville, VA USA 22901  
Email: {ptay,acton}@virginia.edu

John A. Hossack

Dept. of BME  
University of Virginia  
Charlottesville, VA USA 22904  
Email: hossack@virginia.edu

## ABSTRACT

A novel stochastically driven filtering method to despeckle B mode ultrasound images is presented. This method is motivated by viewing the pixel values as a stochastic process and removing outliers, where outliers are defined by local extrema. These outliers are removed by local averaging. This produces another image with new outliers (local extrema) and the process is iteratively repeated. With each iteration homogeneous regions become smoother while edges that defined these regions remain preserved. To evaluate the performance of our proposed method in satisfying these two opposing goals we develop a modified Fisher discriminant contrast metric. Larger values of this metric indicate better performance in reducing each intraregion or intraclass variance and increasing the difference of interregion or interclass means.

## 1. INTRODUCTION

In applications where speckle precludes successful image analysis and removal is desired, speckle is considered noise and its removal as an image restoration problem. Speckle is a common phenomena found in many imaging modalities such as optical laser, synthetic aperture radar, and ultrasound. Many despeckling methods have been proposed with improving these imaging modalities in mind. The despeckling success of the various proposed algorithms are usually subjectively assessed. A fair quantitative evaluation in many cases is avoided.

Our concern is despeckling B mode ultrasound images to aid medical diagnosis. Wagner *et al.* in [1, 2] gives a description of the statistical characteristics of B mode ultrasound speckle. The assumptions of the cause and basic characterizations of ultrasound speckle coincide with Goodman's assumptions and resulting statistical characterizations of speckle caused by a coherent laser in [3, 4]. Although these characterizations of speckle are insightful, an image model like the additive and multiplicative ones in equations (1) and (2), *resp.*, is not offered. Two typical image models are

$$J(n, m) = I(n, m) + \eta(n, m) \quad (1)$$

for the additive noise case and

$$J(n, m) = I(n, m)\eta(n, m) \quad (2)$$

for the multiplicative noise case where  $\eta(n, m)$  is the noise component. Most image restoration methods are specific to the problem being addressed. The restoration problem or motivation for a

reasonable solution are generally constrained by the modeling of the noisy image.

We give a brief overview of various despeckling algorithms proposed for different imaging modalities and applications. A novel stochastically driven method to remove or reduce ultrasound speckle is presented. Lastly, we provide a quantitative assessment of the results of our proposed method and those of other despeckling methods.

## 2. VARIOUS DESPECKLING METHODS

Nagao and Matsuyama in [5] proposed a recursive edge preserving smoothing algorithm. One iteration of this algorithm replaces each pixel value with the mean of some segment  $w_k$  originating from  $J(n, m)$  and the variance of  $w_k$  is the minimum variance attained from a set of variances in all eight directions. Precisely,

$$\hat{J}(n, m) = E(w_k), \quad (3)$$

where  $E(\cdot)$  is the expected value operator,

$$\text{var}(w_k) = \min \{ \text{var}(w_i) \mid \text{for } i = 0, 1, 2, \dots, 7 \}$$

and  $w_0, w_1, w_2, \dots, w_7$  are equal length segments, which originate from  $J(n, m)$  and span all eight directions. This recursion is allowed to continue until convergence in most of the pixel values is established.

Lee in [6] proposed methods to contrast enhance an image and to restore an image corrupted by noise as define in equations (1) or (2). The method in [6] proposes to adaptively locally smooth in homogeneous regions while regions containing edges or salient textures are preserved. This algorithm adaptively chooses a weighting factor  $k$  between zero and one so that the new pixel value  $\hat{J}(n, m)$  is set at

$$\hat{J}(n, m) = \mu + k(J(n, m) - \mu) \quad (4)$$

where  $\mu$  is the mean in some window. The weighting factor  $k$  is adaptively determined as

$$k = \frac{\sigma^2 - \sigma_\eta^2}{\sigma^2} \quad (5)$$

where  $\sigma^2$  is the local variance in the some window. The noise variance is denoted as  $\sigma_\eta^2$  and must be known *a priori*. When  $\sigma^2 \gg \sigma_\eta^2 \neq 0$ , the gain parameter is approximately one, in which case the filter in equation (4) is the identity filter. If the local variance  $\sigma^2$  is greater than but nearly equal to the global noise variance

---

This work was supported by NIH NIBIB grant EB001826 and US Army CDMRP grant (W81XWH-04-1-0240)

$\sigma_\eta^2$ , then the filter specified by equation (4) is a local averaging low pass filter.

When the image is degraded by multiplicative noise as in equation (2), then Lee in [6] recasts the image as an additive noise model of the form

$$\tilde{J}(n, m) = AI(n, m) + B\eta(n, m) + C \quad (6)$$

where  $A, B, C \in \mathbb{R}$  are chosen so that the mean squared error of the multiplicative model from equation (2) and the additive model in equation (6) is minimized. Recasting as an image with additive noise, the adaptative filter defined in equation (4) can be used and the gain parameter  $k$  is redefined as

$$k = \frac{\mu_\eta Q}{\mu_I^2 \sigma_\eta^2 + \mu_\eta^2 Q} \quad (7)$$

where  $\mu_I$  is the approximated local mean of the ideal image  $I(n, m)$  determined as

$$\mu_I = \frac{\mu}{\mu_\eta} \quad (8)$$

within some fixed window and  $\mu$  is the local mean of  $J(n, m)$ . The variable  $Q$  is determined as

$$Q = \frac{\sigma^2 + \mu^2}{\sigma_\eta^2 + \mu_\eta^2} - \mu_I^2 \quad (9)$$

where  $\sigma^2$  is the local variance of  $J(n, m)$  within some window.

The Frost filter given in [7] consists of determining a filter  $f(n', m')$ , so that in a local homogeneous region of  $J(n, m)$  and in the presence of white noise, the expectation criterion

$$E[(I(n, m) - \tilde{I}(n, m))^2] \quad (10)$$

is minimized. The term  $\tilde{I}(n, m)$  is a windowed weighted sum about some constrained ideal image  $I(n, m)$

$$\tilde{I}(n, m) = \sum_{n', m' \in W} f(n', m') I(n + n', m + m') \quad (11)$$

where  $W$  is some odd dimensional window. They derived the filter that minimizes equation (10) as

$$f(n', m') = K\alpha e^{-\alpha|\tau(n', m')|} \quad (12)$$

where

$$\alpha = \sqrt{2a \left( \frac{\mu_\eta}{\sigma_\eta} \right)^2 \left( 1 + \left( \frac{\mu}{\sigma} \right)^2 \right)^{-1} + a}, \quad (13)$$

$K$  is some normalizing constant,  $a$  is a region dependant constant,  $\mu_\eta$  is the mean of the noise,  $\sigma_\eta$  is the standard deviation of the noise,  $\mu$  and  $\sigma$  are the local mean and local standard deviation of  $J(n, m)$ , *resp.* The function  $\tau : \mathbb{Z} \times \mathbb{Z} \rightarrow \mathbb{R}$  is some symmetric function like  $\tau(n, m) = \sqrt{n^2 + m^2}$ .

The linear minimum mean squared error estimate of the ideal noise free image given by Kuan *et al.* in [8] is defined as

$$\hat{I}(n, m) = \mu + \frac{\omega^2 - \sigma_\eta^2}{\omega^2} (J(n, m) - \mu) \quad (14)$$

where  $\mu$  is the local variance in some window about  $J(n, m)$  and  $\omega^2$  is the local variance in some weighted window about  $J(n, m)$ . The local weighted variance  $\omega^2$  is defined as

$$\omega^2 = \frac{1}{N'M'} \sum_{n', m' \in W} w(n', m') (J(n + n', m + m') - \mu)^2 \quad (15)$$

where  $\sum_{n', m'} w(n', m') = 1$  and  $W$  is some odd dimensional square window.

The adaptive weighted median filter (AWMF) of Loupas *et al.* in [9] models the ultrasound image as

$$J(n, m) = I(n, m) + \sqrt{I(n, m)} \eta(n, m). \quad (16)$$

From the image model given in equation (16) and when the ideal image is equal to a constant in some local neighborhood, then

$$\sigma^2 = c\sigma_\eta^2 \quad (17)$$

where  $\sigma^2$  and  $\sigma_\eta^2$  are the local variance of the observed image and the variance of the noise, *resp.* The AWMF is defined as

$$\hat{J}(n, m) = \text{median} \left\{ \underbrace{J(n', m'), \dots, J(n', m')}_{w(n', m')} \right\} \quad (18)$$

for  $n', m'$  in some window about  $(n, m)$  and

$$w(n', m') = \text{round}_+ \left\{ w(0, 0) - \frac{c\sigma^2 \sqrt{n'^2 + m'^2}}{\mu} \right\} \quad (19)$$

where  $\text{round}_+ \{\cdot\}$  means round to the nearest non-negative integer,  $c$  is some constant,  $\mu$  is the local mean, and  $\sigma^2$  is the local variance. The constant  $c$  and the window term  $w(0, 0)$  determines the AWMF's ability to preserve edges.

Yu and Acton in [10] proposed the speckle reducing anisotropic diffusion (SRAD) method. The SRAD algorithm iteratively filters a nonzero valued image  $I(x, y; 0) = I(x, y)$  according to

$$\frac{\partial I(x, y; t)}{\partial t} = \text{div}[c(q) \nabla I(x, y; t)] \quad (20)$$

and

$$\left. \frac{\partial I(x, y; t)}{\partial \vec{n}} \right|_{B(\Omega)} = 0 \quad (21)$$

where  $\vec{n}$  is the outward normal vector to the border of  $\Omega$ . The diffusion coefficient  $c(\cdot)$  is defined either as the quotient

$$c(q(x, y; t)) = \frac{q_0^4(t) + q_0^2(t)}{q_0^4(t) + q^2(x, y; t)} \quad (22)$$

or as the exponential function

$$c(q(x, y; t)) = \exp \left( \frac{q_0^2(t) - q^2(x, y; t)}{q_0^4(t) + q_0^2(t)} \right). \quad (23)$$

In both equations (22) and (23), if  $q(x, y; t) \approx q_0(t)$ , then  $c(q(x, y; t)) \approx 1$  and equation (20) is a local smoothing operator. If  $q(x, y; t) \gg q_0(t)$ , then the diffusion coefficient is very small and smoothing in a local region around  $(x, y)$  is suppressed. When at time  $t$ , if  $(x, y)$  resides in a homogeneous region, then smoothing can be promoted by allowing  $q(x, y; t) \approx q_0(t)$ . When  $(x, y)$  lie on an edge, then defining  $q(x, y; t) \gg q_0(t)$  would prohibit edge deterioration. The function  $q(\cdot)$  is defined as

$$q(x, y; t) = \sqrt{\frac{\frac{1}{2} \left( \frac{|\nabla I|}{I} \right)^2 - \frac{1}{16} \left( \frac{\nabla^2 I}{I} \right)^2}{\left( 1 + \left( \frac{1}{4} \right) \left( \frac{\nabla^2 I}{I} \right)^2 \right)}}. \quad (24)$$

SRAD requires initialization of  $q_0(t)$ , which is determined by calculating the mean and standard deviation within a homogeneous region where speckle is prevalent.

### 3. THE SQUEEZE BOX FILTER

The methods in section 2 evaluate every sample in a image and adaptively determines whether to smooth (locally average) or not. The iterative filtering method we presented in this section only considers samples which are outliers of some probability density function (PDF) and applies local smoothing to these outliers. The local extrema are considered outliers and are not used in the determination of the local mean. The choice of the neighborhood  $\mathcal{N}$  is extremely important, since the mean of some PDF is determined by samples in  $\mathcal{N}$ . Each iteration produces a sequence with locally reduced variance. The local extrema of the new sequence are consider as outliers and the process is iterated. The steps of our proposed iterative method are as follow:

1. Each iteration  $i$  begins by determining the set of locations of local maxima and local minima. The locations of these extrema are defined by the set

$$\mathcal{N}_E = \{(n, m) \mid g_{i-1}(n, m) \text{ meets condition 1 or 2} \}$$

$$\text{Condition 1: } g_{i-1}(n, m) > g_{i-1}(n+k, m+l)$$

$$\text{Condition 2: } g_{i-1}(n, m) < g_{i-1}(n+k, m+l)$$

where  $k, l = -1$  or  $1$ .

2. Without using the local extrema values, our algorithm replaces the extremum with the local mean taken from neighboring samples. For all  $(n, m) \in \mathcal{N}_E$

$$g_i(n, m) = \frac{1}{|\mathcal{N}|} \sum_{(k,l) \in \mathcal{N}} g_{i-1}(k, l) \quad (25)$$

where  $\mathcal{N}$  is some local neighborhood of  $(n, m)$ ,  $|\mathcal{N}|$  is the cardinality of set  $\mathcal{N}$ , and  $(n, m) \notin \mathcal{N}$ .

3. If convergence is not attained, that is

$$\sum_{\forall n, m} |g_{i-1}(n, m) - g_i(n, m)| > \epsilon \quad (26)$$

for some predefined  $\epsilon > 0$ , then another iteration is performed. If convergence is attained, then no further improvements can be attained with this filtering method.

By removing outliers at each iteration, this method reduces the local variance at each pixel. In effect, this method produces a convergent sequence of images by squeezing the stochastically distributed pixel values to a limiting value. Thus, we call this stochastically driven method the squeeze box filter (SBF).

### 4. EXPERIMENT AND RESULTS

To evaluate the performance of the proposed SBF against the other methods in section 2, a phantom, consisting of a background class with pixel values set at one and two other classes with pixel values set at either one or ten, is used. Each nonbackground class consist of five bright disks or five dark disks of various diameters vertically aligned.

The phantom and the Field II simulation [11], which is the image being processed in this evaluation, are shown in Figs. 1(a) and 1(b), *resp.* The simulation is constructed with the transducer at the top of the image. The focus point of the simulation is set at 70mm axial distance from the transducer and at lateral position 0mm. In this simulation, the spatial varying point spread functions

are shown along the column at lateral position -15mm and at axial distances 40mm, 50mm, 60mm, 70mm, and 80mm. Fig. 1(c) shows the SRAD result applied to the simulated image in Fig. 1(b). Fig. 1(d) is the resulting image of SBF applied to the same image. It can be observed that the large intensity (white) disks on the right side of Fig. 1(d) is brighter and the background class is smoother with SBF restoration.

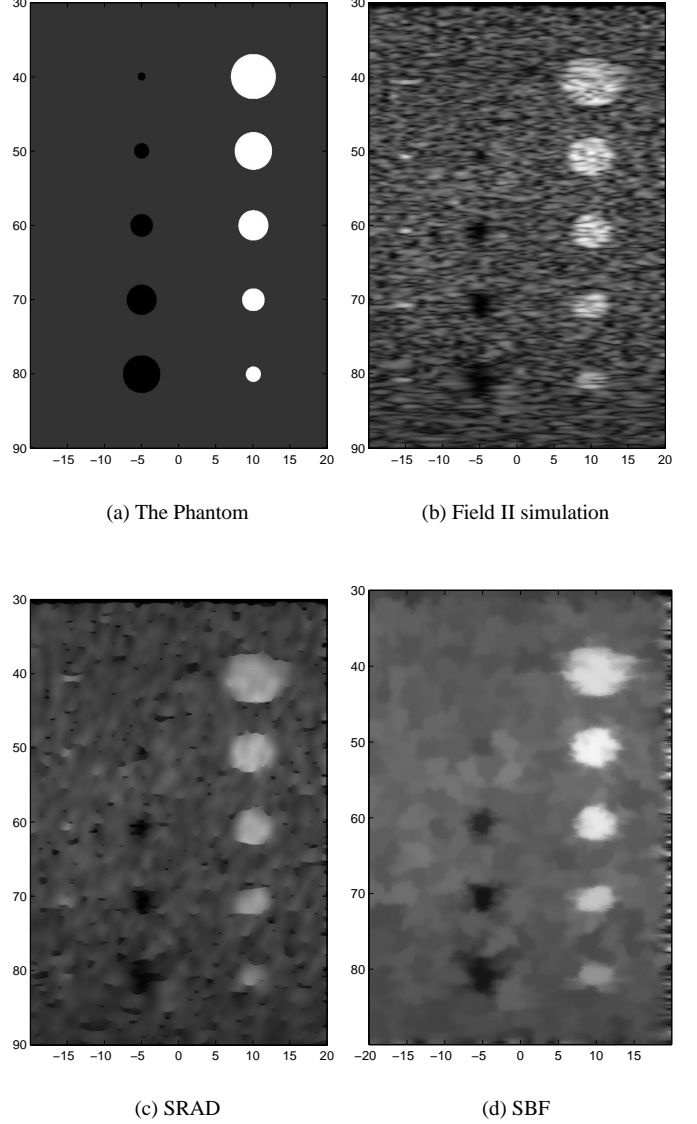


**Fig. 1.** (a) Three class phantom, (b) Field II simulation, (c) output due to SRAD, and (d) output due to SBF.

To quantitatively evaluate which despeckling method provides the best improvements to an ultrasound image, we use a modified Fisher discriminant contrast metric. This measure determines how well an algorithm reduces variances in homogeneous classes while keeping the distinct classes well separated and preserving edges.

This metric is defined as

$$Q(alg) \stackrel{def}{=} \frac{\sum_{k \neq l} (\mu_{C_k} - \mu_{C_l})^2}{\sum_{k=1}^3 \sigma_{C_k}^2}, \quad (27)$$

$$\mu_{C_k} \stackrel{def}{=} \frac{1}{|C_k|} \sum_{(n,m) \in C_k} J_{alg}(n, m), \quad (28)$$

$$\sigma_{C_k}^2 \stackrel{def}{=} \frac{1}{|C_k|} \sum_{(n,m) \in C_k} (J_{alg}(n, m) - \mu_{C_k})^2, \quad (29)$$

where  $J_{alg}$  is the resulting image due to algorithm  $alg$ , and  $|C_k|$  denotes the number of pixels in class  $C_k$ . To avoid sensitivity to resolution, we normalize the measure in equation (27) as

$$\tilde{Q}(alg) \stackrel{def}{=} \frac{Q(alg)}{Q(id)} \quad (30)$$

where  $J_{id} = J$ . This performance metric  $\tilde{Q}(alg)$  is called ultrasound despeckling assessment index (USDSAI). If a despeckling algorithm produces classes that are well separated, then the numerator in equation (27) will be large. If the segmentation or restoration algorithm produces small intra-class variances, then the denominator of equation (27) will be small. An algorithm that attains a large numerator and a small denominator will yield a large USDSAI quantity  $\tilde{Q}(alg)$ . Large USDSAI would indicate that  $alg$  produces desirable restoration or enhancement results.

To present an objective comparison, we perform an exhaustive search, varying the parameters of each algorithm in section 2 and SBF so that the USDSAI value  $\tilde{Q}(alg)$  is maximized. The USDSAI values  $\tilde{Q}(alg)$  of each filter are given in Table 1. The USDSAI in Table 1 are the results attained by an exhaustive efforts to maximize this metric. The result of SBF was attained by using the values within a  $9 \times 9$  square window minus the extremum value to determine the local mean at each extrema. The maximum USDSAI of the SBF is 2.1144 and took 542 iterations to attain. The USDSAI of SRAD and SBF exceeds the performance of the other despeckling methods with SBF performing better than SRAD, albeit at a much greater computational cost and degradation to relevant point scatters that is SBF totally removed the point scatters along column 15 while SRAD retained these features.

		$\tilde{Q}(alg)$
F	Nagao	1.3651
I	Lee	1.2097
L	Frost	1.0457
T	Kuan	1.0016
E	AWMF	1.1025
R	SRAD	1.8187
S	SBF	<b>2.1144</b>

**Table 1.** USDSAI for the various algorithms tested.

## 5. CONCLUSION

An overview of some of the prominent speckle removing algorithms for various imaging modalities is presented. These despeckling methods were used to assess the performance of a novel stochastically driven SBF method. A visual inspection shows that SRAD is better at preserving relevant point scatters than SBF. A modified Fisher discriminant metric was used to quantify the contrast improvement performance of each despeckling algorithm. The quantitative evaluation using the USDSAI metric shows that the SBF method performed the best contrast improvement to the Field II simulated image while reduction to intraclass variance is on par with SRAD.

## 6. REFERENCES

- [1] R. F. Wagner, S. W. Smith, J. M. Sandrik, and H. Lopez, "Statistics of speckle in ultrasound B-scans," *IEEE Trans. Sonics Ultrason.*, vol. 30, no. 3, pp. 156–163, May 1983.
- [2] R. F. Wagner, M. F. Insana, and S. W. Smith, "Fundamental correlation lengths of coherent speckle in medical ultrasonic images," *IEEE Trans. Ultrason., Ferroelect., Freq. Contr.*, vol. 35, no. 1, pp. 34–44, January 1988.
- [3] J. W. Goodman, "Statistical properties of laser speckle patterns," in *Laser Speckle and Related Phenomena*, J. C. Dainty, Ed., pp. 9–75. Springer-Verlag, Berlin, 1984.
- [4] J. W. Goodman, "Speckle phenomena in optics: theory and applications version 5.0," <http://www-ee.stanford.edu/~goodman/>, August 2005.
- [5] M. Nagao and T. Matsuyama, "Edge preserving smoothing," *Computer Graphics and Image Processing*, vol. 9, no. 4, pp. 394–407, April 1979.
- [6] J. S. Lee, "Digital image enhancement and noise filtering by use of local statistics," *IEEE Trans. Pattern Anal. Machine Intell.*, vol. PAMI-2, no. 2, pp. 165–168, March 1980.
- [7] V. S. Frost, J. A. Stiles, K. S. Shanmugan, and J. C. Holtzman, "A model for radar images and its application to adaptive digital filtering of multiplicative noise," *IEEE Trans. Pattern Anal. Machine Intell.*, vol. PAMI-4, no. 2, pp. 157–166, March 1982.
- [8] D. T. Kuan, A. A. Sawchuk, T. C. Strand, and P. Chavel, "Adaptive restoration of images with speckle," *IEEE Trans. Acoust., Speech, Signal Processing*, vol. ASSP-35, no. 3, pp. 373–383, March 1987.
- [9] T. Loupas, W. N. McDicken, and P. L. Allan, "An adaptive weighted median filter for speckle suppression in medical ultrasonic images," *IEEE Trans. Circuits Syst.*, vol. 36, no. 1, pp. 129–135, January 1989.
- [10] Y. Yu and S. T. Acton, "Speckle reducing anisotropic diffusion," *IEEE Trans. Image Processing*, vol. 11, no. 11, pp. 1260–1270, November 2002.
- [11] J. A. Jensen and N. B. Svendsen, "Calculation of pressure fields from arbitrarily shaped apodized and excited ultrasound transducers," *IEEE Trans. Ultrason., Ferroelect., Freq. Contr.*, vol. 39, no. 2, pp. 262–267, February 1992.



# Ultrasound Despeckling Using An Adaptive Window Stochastic Approach

Peter C. Tay  
Depts. of ECE and BME  
University of Virginia  
Charlottesville, VA USA 22901  
Email: ptay@virginia.edu

Scott T. Acton  
Depts. of ECE and BME  
University of Virginia  
Charlottesville, VA USA 22901  
Email: acton@virginia.edu

John A. Hossack  
Dept. of BME  
University of Virginia  
Charlottesville, VA USA 22904  
Email: hossack@virginia.edu

**Abstract**—A novel stochastically driven filtering method to despeckle B mode ultrasound images is presented. This method is motivated by viewing the pixel values as a stochastic process and removing outliers, where outliers are defined by local extrema. These outliers are removed by local averaging. This produces another image with new outliers (local extrema) and the process is iterated. With each iteration homogeneous regions become smoother while edges that defined these regions are preserved. By allowing a dynamically varying window to determine the local mean, we achieve equivalent results with fewer iterations.

## I. INTRODUCTION

Speckle is a common phenomena found in many imaging modalities such as optical laser, synthetic aperture radar, and ultrasound. Goodman's intuitive explanation of the appearance of speckle is due to the signal being composed of a sum of independent complex components caused by the random roughness of the object being imaged [1], [2]. Speckle can be modeled as a complex random walk where individual complex components are independent of each other and the phase and amplitude of each component are also independent. Since speckle is a common and prevalent phenomena in ultrasound imaging, Goodman's intuition and analysis is relevant.

In Fig. 1, we show a block diagram of the ultrasound data flow from the real-valued digitized **RF** signal detected at the transducer to the intermediate complex-valued **IQ** data to the real-valued **B mode** data. The processing that occurs between the **RF** and **IQ** data is proprietary to each ultrasound manufacture and is generally privileged information. The probability distribution of the norm of the **IQ** to produce **B mode** data is considered in Goodman's analysis found in [2]. Exactly applying Goodman's analysis to the **IQ** data, it can be derived that the samples of homogeneous regions of the **B mode** data are Rayleigh or more generally Rician distributed. As with any probability distribution function (PDF), outliers will occur and values close to the mean occur more frequently. Determining which samples are outliers and consistently replacing these outlier with a meaningful value is difficult.

Numerous despeckling methods indiscriminately scrutinize every pixel values and rely on local statistics like the local mean, local variance, and/or the gradient to determine how aggressively a pixel should be smoothed. These local statistics are usually determined by a fixed window size usually of odd

dimensions  $3 \times 3$ ,  $5 \times 5$ , and so on. One of the first of these filters is the Nagao and Matsuyama filter proposed in [3], which recursively replaces each pixel value with the mean of the minimum variance segment from all eight direction originating from the pixel under scrutiny.

A more profound and adaptive despeckling method was proposed by the Lee filter in [4]. This algorithm adaptively chooses a weighting factor  $k$  between zero and one so that the new pixel value  $\hat{J}(n, m)$  is set at

$$\hat{J}(n, m) = \mu + k(J(n, m) - \mu) \quad (1)$$

where  $\mu$  is the mean in some window. The weighting factor  $k$  is adaptively determined as

$$k = \frac{\sigma^2 - \sigma_\eta^2}{\sigma^2} \quad (2)$$

where  $\sigma^2$  is the local variance in the some window. The noise variance is denoted as  $\sigma_\eta^2$  and must be known *a priori*. When  $\sigma^2 \gg \sigma_\eta^2 \neq 0$ , the gain parameter is approximately one, in which case the filter in equation (1) is the identity filter. If the local variance  $\sigma^2$  is greater than but nearly equal to the global noise variance  $\sigma_\eta^2$ , then the filter specified by equation (1) is a local averaging low pass filter.

The Frost filter given in [5] consists of determining a filter  $f(n', m')$ , so that in a local homogeneous region and in the presence of white noise, the expectation criterion is minimized. The term  $\tilde{I}(n, m)$  is a windowed weighted sum about some constrained ideal image  $I(n, m)$

$$\tilde{I}(n, m) = \sum_{n', m' \in W} f(n', m') I(n + n', m + m') \quad (3)$$

where  $W$  is some odd dimensional window.

The linear minimum mean squared error (LLMSE) estimate of the ideal noise free image given by Kuan *et al.* in [6] is defined as

$$\tilde{I}(n, m) = \mu + \frac{\omega^2 - \sigma_\eta^2}{\omega^2} (J(n, m) - \mu) \quad (4)$$

where  $\mu$  is the local variance in some window about  $J(n, m)$  and  $\omega^2$  is the local variance in some weighted window about  $J(n, m)$ . The local weighted variance  $\omega^2$  is defined as

$$\omega^2 = \frac{1}{N'M'} \sum_{n', m' \in W} w(n', m') (J(n + n', m + m') - \mu)^2 \quad (5)$$

where  $\sum_{n',m'} w(n',m') = 1$  and  $W$  is some odd dimensional square window.

The adaptive weighted median filter (AWMF) in [7] models the ultrasound image as

$$J(n, m) = I(n, m) + \sqrt{I(n, m)} \eta(n, m). \quad (6)$$

From the image model given in equation (6) and when the ideal image is equal to a constant in some local neighborhood, then

$$\sigma^2 = c\sigma_\eta^2 \quad (7)$$

where  $\sigma^2$  and  $\sigma_\eta^2$  are the local variance of the observed image and the variance of the noise, *resp.* The AWMF is defined as

$$\hat{J}(n, m) = \text{median} \left\{ \underbrace{J(n', m'), \dots, J(n', m')}_{w(n', m')} \right\} \quad (8)$$

for  $n', m'$  in some window about  $(n, m)$  and

$$w(n', m') = \text{round}_+ \left\{ w(0, 0) - \frac{c\sigma^2 \sqrt{n'^2 + m'^2}}{\mu} \right\} \quad (9)$$

where  $\text{round}_+ \{\cdot\}$  means round to the nearest non-negative integer,  $c$  is some constant,  $\mu$  is the local mean, and  $\sigma^2$  is the local variance.

The filtering method of Yu and Acton in [8], the speckle reducing anisotropic diffusion (SRAD) method incorporates gradient information as well as local statistics to determine a smoothing kernel. The SRAD algorithm iteratively filters a nonzero valued image  $J(x, y; 0) = J(x, y)$  according to

$$\frac{\partial J(x, y; t)}{\partial t} = \text{div}[c(q) \nabla J(x, y; t)] \quad (10)$$

and

$$\left. \frac{\partial J(x, y; t)}{\partial \vec{n}} \right|_{B(\Omega)} = 0 \quad (11)$$

where  $\vec{n}$  is the outward normal vector to the border  $B(\Omega)$ . The diffusion coefficient  $c(\cdot)$  is defined either as the quotient

$$c(q(x, y; t)) = \frac{q_0^4(t) + q_0^2(t)}{q_0^4(t) + q^2(x, y; t)} \quad (12)$$

or as the exponential function

$$c(q(x, y; t)) = \exp \left( \frac{q_0^2(t) - q^2(x, y; t)}{q_0^4(t) + q_0^2(t)} \right). \quad (13)$$

In both equations (12) and (13), if  $q(x, y; t) \approx q_0(t)$ , then  $c(q(x, y; t)) \approx 1$  and equation (10) is a local smoothing operator. If  $q(x, y; t) \gg q_0(t)$ , then the diffusion coefficient is very small and smoothing in a local region around  $(x, y)$  is suppressed. When at time  $t$ , if  $(x, y)$  resides in a homogeneous region, then smoothing can be promoted by allowing  $q(x, y; t) \approx q_0(t)$ . When  $(x, y)$  lie on an edge, then defining  $q(x, y; t) \gg q_0(t)$  would prohibit edge deterioration. The function  $q(\cdot)$  is defined as

$$q(x, y; t) = \sqrt{\frac{\frac{1}{2} \left( \frac{|\nabla J|}{J} \right)^2 - \frac{1}{16} \left( \frac{\nabla^2 J}{J} \right)^2}{\left( 1 + \left( \frac{1}{4} \right) \left( \frac{\nabla^2 J}{J} \right) \right)^2}}. \quad (14)$$

SRAD requires initialization of  $q_0(t)$ , which is determined by calculating the mean and standard deviation within a homogeneous region where speckle is prevalent.

Determining the appropriate window to determine local statistics is important to these and other algorithms. We offer a novel despeckling method that iteratively removes outliers by determining the local mean and standard deviation from an adaptively varying window. The adaptively determined mean is used to replace the outlying values of an B mode ultrasound image causing homogeneous regions to be aggressively smoothed while preservation of edges is profoundly respected.

## II. THE SQUEEZE BOX FILTER

We propose an iterative filtering method that considers local extrema of the **B mode** image  $J(n, m)$  as outliers and only applies local smoothing to these outliers. The local extrema are considered outliers and are not used in the determination of the local mean. The choice of the neighborhood or window  $\mathcal{N}$  is extremely important, since the mean of some PDF is determined by samples in  $\mathcal{N}$ . An explanation of a robust method to determine this window will be given in section III. Each iteration of our proposed method produces a sequence with locally reduced variance. The local extrema of the new sequence are consider as outliers and the process is iterated. The steps of our proposed iterative method are as follow:

- 1) Each iteration  $i$  begins by determining the set of locations of local maxima and local minima. The locations of these extrema are defined by the set

$$\mathcal{N}_E = \{(n, m) \mid J_{i-1}(n, m) \text{ meets condition 1 or 2} \}$$

$$\text{Condition 1: } J_{i-1}(n, m) > J_{i-1}(n+k, m+l)$$

$$\text{Condition 2: } J_{i-1}(n, m) < J_{i-1}(n+k, m+l)$$

where  $k, l = -1$  or  $1$ .

- 2) Without using the local extrema values, our algorithm replaces the extremum with the local mean taken from neighboring samples. For all  $(n, m) \in \mathcal{N}_E$

$$J_i(n, m) = \frac{1}{|\mathcal{N}|} \sum_{(k, l) \in \mathcal{N}} J_{i-1}(k, l) \quad (15)$$

where  $\mathcal{N}$  is some local neighborhood of  $(n, m)$ ,  $|\mathcal{N}|$  is the cardinality of set  $\mathcal{N}$ , and  $(n, m) \notin \mathcal{N}$ .

- 3) If convergence is not attained, that is

$$\sum_{\forall n, m} |J_{i-1}(n, m) - J_i(n, m)| > \epsilon \quad (16)$$

for some predefined  $\epsilon > 0$ , then another iteration is performed. If convergence is attained, then no further improvements can be attained with this filtering method.

By removing outliers at each iteration, this method reduces the local variance at each pixel. In effect, this method produces a convergent sequence of images by squeezing the stochastically distributed pixel values to a limiting value. We call this stochastically driven method the squeeze box filter (SBF).

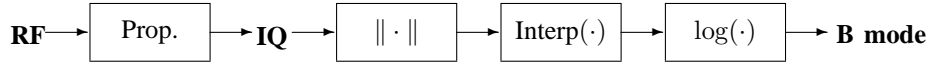


Fig. 1. RF data to IQ data to B mode image.

### III. WINDOW SELECTION

Given  $J_{i-1}(n, m) \in \mathcal{N}_E$  is an extremum value at some iteration  $i$ , some considerations for a neighborhood or window  $\mathcal{N}$  about  $J_{i-1}(n, m)$  to determine the local mean are

- 1) the samples of  $\mathcal{N}$  should be from the same homogeneous region as  $J_{i-1}(n, m)$ ; and
- 2) to get an accurate estimate of the actual mean within a homogeneous region, the cardinality  $|\mathcal{N}|$  should be as large as possible.

To effectively and dynamically determine the window  $\mathcal{N}$ , a multiplicative image model of equation (17) is used

$$J(n, m) = I(n, m)\eta(n, m) \quad (17)$$

where  $I(n, m)$  is the speckle free image and  $\eta(n, m)$  is a white stationary random process. This model is supported by the empirical evidence and deductive arguments given in [9], [10]. In a constant homogeneous region  $\mathcal{N}_c$ ,  $I(n, m) = c \neq 0$  for all  $(n, m) \in \mathcal{N}_c$ , the mean to standard deviation ratio  $R_{\mathcal{N}_c}(n, m)$  is independent of  $c$ , that is,

$$R_{\mathcal{N}_c}(n, m) = \frac{\mu_{\mathcal{N}_c}}{\sigma_{\mathcal{N}_c}} \quad (18)$$

where  $\mu_{\mathcal{N}_c}$  and  $\sigma_{\mathcal{N}_c}$  are the mean and standard deviation within  $\mathcal{N}_c$ , *resp.* Let  $R$  be the ratio defined by equation (18) determined from a known non-zero constant region. At each outlier, we dynamically choose a rectangular window of dimension  $N' \times M'$  so that  $|R - R_{N \times M}|$  is minimized where  $R_{N \times M}$  is the ratio of the mean to standard deviation within a rectangular  $N \times M$  window centered at the outlier  $J_{i-1}(n, m)$ . The SBF despeckling method using this dynamically varying window (SBF-DVW) replaces each outlier values with the mean determined from this dynamically varying window less the outlier value.

### IV. EXPERIMENTS AND RESULTS

To evaluate the performance of our algorithm we created a phantom and the Field II simulation [11] of the phantom, which is the image being processed in this evaluation. The phantom and the Field II simulation are shown in Figs. 2(a) and 2(b), *resp.* The phantom consist of the background class with pixel values set at one. The phantom also consist of two other classes with pixel values set at either one or ten. Each nonbackground class consist of five bright disks or five dark disks of various diameters vertically aligned. The Field II simulation of an actual B mode ultrasound image is constructed with the transducer at the top of the image. The focus point of the simulation is set at 70mm axial distance from the transducer and at lateral position 0mm. In this simulation, the spatial varying point spread functions are shown along the column at lateral position -15mm and at axial distances 40mm, 50mm, 60mm, 70mm, and 80mm. Fig. 2(c)

shows the SRAD result applied to the simulated image in Fig. 2(b). Fig. 2(d) is the resulting image of SBF-DVW applied to the same image. The SBF-DVW we implemented allowed for a rectangular window with odd row and column dimensions to vary  $N, M = 3, 5, \dots, 41$ . It can be observed that the large intensity (white) disks aligned on the center column of Fig. 2(d) is brighter and the background class is smoother with SBF-DVW method. The visual results of SBF using a fixed  $9 \times 9$  is almost indistinguishable from the result of SBF-DVW. Thus only the result of SBF-DVW is shown in Fig. 2.

To quantitatively evaluate performance we use a modified Fisher discriminant contrast metric. This measure determines how well an algorithm reduces variances in homogeneous classes while keeping the distinct classes well separated and preserving edges. This metric is defined as

$$Q(alg) \stackrel{def}{=} \frac{\sum_{k \neq l} (\mu_{C_k} - \mu_{C_l})^2}{\sum_{k=1}^3 \sigma_{C_k}^2}, \quad (19)$$

$$\mu_{C_k} \stackrel{def}{=} \frac{1}{|C_k|} \sum_{(n, m) \in C_k} J_{alg}(n, m), \quad (20)$$

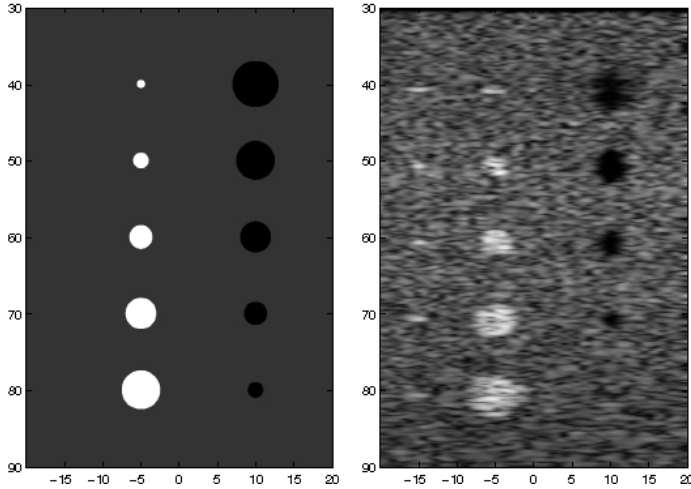
$$\sigma_{C_k}^2 \stackrel{def}{=} \frac{1}{|C_k|} \sum_{(n, m) \in C_k} (J_{alg}(n, m) - \mu_{C_k})^2, \quad (21)$$

where  $\mathbf{J}_{alg}$  is the resulting image due to algorithm  $alg$ , and  $|C_k|$  denotes the number of pixels in class  $C_k$ . To avoid sensitivity to resolution, we normalize the measure in equation (19) as

$$\tilde{Q}(alg) \stackrel{def}{=} \frac{Q(alg)}{Q(id)} \quad (22)$$

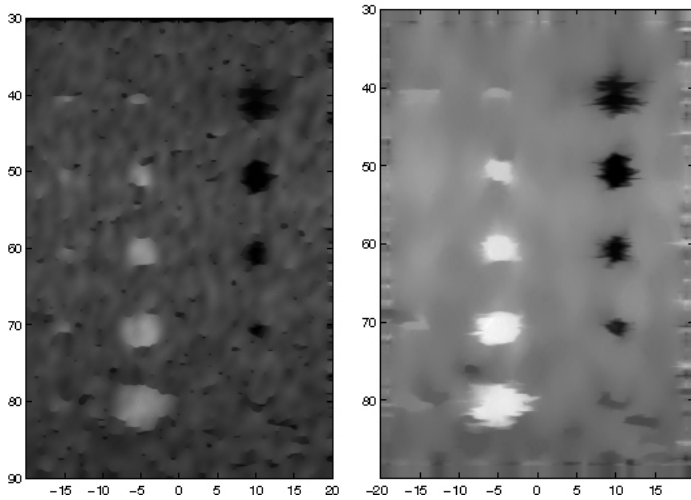
where  $\mathbf{J}_{id} = \mathbf{J}$ . This performance metric  $\tilde{Q}(alg)$  is called ultrasound despeckling assessment index (USDSAI). If a despeckling algorithm produces classes that are well separated, then the numerator in equation (19) will be large. If the segmentation or restoration algorithm produces small intra-class variances, then the denominator of equation (19) will be small. An algorithm that attains a large numerator and a small denominator will yield a large USDSAI quantity  $\tilde{Q}(alg)$ . Large USDSAI would indicate that  $alg$  produces desirable restoration or enhancement results.

An objective quantitative comparison is performed by varying the parameters over a wide range of reasonable values for each algorithm listed in Table I, the number of iteration used in SBF with a fixed  $9 \times 9$  window, and SBF-DVW so that the USDSAI value  $\tilde{Q}(alg)$  is maximized. The USDSAI values  $\tilde{Q}(alg)$  of each filter are given in Table I. The USDSAI in Table I are the results attained by an exhaustive effort to maximize this metric. The results of the fixed window SBF



(a) The Phantom

(b) Field II simulation



(c) SRAD

(d) SBF-DVW

Fig. 2. (a) Three class phantom, (b) Field II simulation, (c) output due to SRAD, and (d) output due to SBF-DVW.

and SBF-DVW exceed the results of the other methods. The result of SBF was attained by using the values within a  $9 \times 9$  square window minus the extremum value to determine the local mean at each extrema. The maximum attained USDSAI of the SBF is 2.1491 and took 810 iterations to attain. The maximum USDSAI of SBF-DVW is slightly better at 2.1716, but occurred with only 143 iterations. This result is promising in which we maybe able to decrease the run time of our proposed SBF algorithm while maintaining excellent contrast improvements.

## V. CONCLUSION

Based on the intuition that speckle is a random stochastic process, we develop a novel despeckling method SBF, which

		$\tilde{Q}(alg)$
F	Nagao	1.0315
I	Lee	1.2007
L	Frost	1.0446
T	Kuan	1.0012
E	AWMF	1.0959
R	SRAD	1.8603
S	SBF	<b>2.1491</b>
	SBF-DVW	<b>2.1716</b>

TABLE I  
USDSAI FOR THE VARIOUS ALGORITHMS TESTED.

is aimed at replacing outliers with the local mean. The SBF and SBF-DVW methods attained better qualitative and quantitative results than the other well known published despeckling methods. By allowing a dynamically varying window in which to determine the local mean, SBF-DVW attain slightly better results than SBF with a fixed window with fewer iterations. This result is promising in that we can achieve a faster algorithm without compromising performance.

## ACKNOWLEDGMENT

This work was supported by NIH NIBIB grant EB001826 and US Army CDMRP grant (W81XWH-04-1-0240).

## REFERENCES

- [1] J. W. Goodman, "Statistical properties of laser speckle patterns," in *Laser Speckle and Related Phenomena*, J. C. Dainty, Ed. Berlin: Springer-Verlag, 1984, pp. 9–75.
- [2] —, "Speckle phenomena in optics: Theory and applications version 5.0," <http://www-ee.stanford.edu/~goodman/>, Aug. 2005.
- [3] M. Nagao and T. Matsuyama, "Edge preserving smoothing," *Computer Graphics and Image Processing*, vol. 9, no. 4, pp. 394–407, April 1979.
- [4] J. S. Lee, "Digital image enhancement and noise filtering by use of local statistics," *IEEE Trans. Pattern Anal. Machine Intell.*, vol. PAMI-2, no. 2, pp. 165–168, March 1980.
- [5] V. S. Frost, J. A. Stiles, K. S. Shanmugan, and J. C. Holtzman, "A model for radar images and its application to adaptive digital filtering of multiplicative noise," *IEEE Trans. Pattern Anal. Machine Intell.*, vol. PAMI-4, no. 2, pp. 157–166, March 1982.
- [6] D. T. Kuan, A. A. Sawchuk, T. C. Strand, and P. Chavel, "Adaptive restoration of images with speckle," *IEEE Trans. Acoust., Speech, Signal Processing*, vol. ASSP-35, no. 3, pp. 373–383, March 1987.
- [7] T. Loupas, W. N. McDicken, and P. L. Allan, "An adaptive weighted median filter for speckle suppression in medical ultrasonic images," *IEEE Trans. Circuits Syst.*, vol. 36, no. 1, pp. 129–135, January 1989.
- [8] Y. Yu and S. T. Acton, "Speckle reducing anisotropic diffusion," *IEEE Trans. Image Processing*, vol. 11, no. 11, pp. 1260–1270, November 2002.
- [9] R. F. Wagner, S. W. Smith, J. M. Sandrik, and H. Lopez, "Statistics of speckle in ultrasound B-scans," *IEEE Trans. Sonics Ultrason.*, vol. 30, no. 3, pp. 156–163, May 1983.
- [10] R. F. Wagner, M. F. Insana, and S. W. Smith, "Fundamental correlation lengths of coherent speckle in medical ultrasonic images," *IEEE Trans. Ultrason., Ferroelect., Freq. Contr.*, vol. 35, no. 1, pp. 34–44, Jan. 1988.
- [11] J. A. Jensen and N. B. Svendsen, "Calculation of pressure fields from arbitrarily shaped apodized and excited ultrasound transducers," *IEEE Trans. Ultrason., Ferroelect., Freq. Contr.*, vol. 39, no. 2, pp. 262–267, Feb. 1992.